# Demonstration of a Scalable 2D Optical Phased Array

**Emmanuel A. Malikides**

**A thesis submitted for the degree of**
**Bachelor of Philosophy (Science) with Honours in Physics of**
**The Australian National University**

**October, 2012**

# Declaration

This thesis is an account of research undertaken between February 2012 and October 2012 at The Department of Physics, Faculty of Science, The Australian National University, Canberra, Australia.

Except where acknowledged in the customary manner, the material presented in this thesis is, to the best of my knowledge, original and has not been submitted in whole or part for a degree in any university.

Emmanuel Alexander Malikides
October, 2012

q

# Acknowledgements

This year has been incredibly epic. I have learned a great deal about myself and research. Naturally this has been through extremely large collaboration of people.

I would first like to thank my supervisor, Daniel Shaddock. You have been an outstanding supervisor and guided me well throughout this project. You have also given me the opportunity to play with some very cool toys. Thankyou, it was great fun. I am especially thankful for the incredible opportunity to travel to JPL to continue this work. I'm certain this will be an amazing experience.

I would also like to thank my co-supervisor and lab buddy Robert Ward. Thanks for your patience and helpful answers to my questions. You did a great job putting up with my blithering and telling me not to worry about unimportant details. I am slowly begining to see your point of view.

I would next like to thank Danielle Wuchenich, and Andrew Sutton -thanks for being so awesome! You guys are an inspiring figures in the lab, and I've learned a lot from you. Thanks are also due to Timothy Lam, you were extremely helpful in the lab, and I am indebted to you for your unwavering ability to conquer Labview in worst of times.

Thanks to David Bowman and Lyle Roberts for inciteful discussions about the array, and helping me whenever I should ask. David you have introduced me to many a colourful colloquealism.

Thank you to Roland, Silvie, Jarrod and John. We made a good office, and although I was never there, I very much enjoyed the times that I was.

And a big thankyou to the rest Gravitational wave group. I've had a great time with you guys. A special thanks to Thanh Nguyen, Sheon Chua and Roland for helping edit my thesis.

I would also like to sincerely thank John Close. Your support and counsel over the course of my degree and throughout this year have been of unprecentented benefit. Thankyou to the atom optics group for making the physics building such a friendly and inviting place throughout my degree.

Finally I would like to thank my parents Stephanos and Margaret for supporting me when the going got tough, and my brothers Sean and Theo for keeping me sane.

# Abstract

An optical phased array is a device that permits beam steering, focusing and coherent combining of multiple laser beams by controlling their relative phase. Optical phased arrays have application as laser steering systems and can be used for space debris perturbation and deorbiting. Radio frequency phased arrays have existed for over 50 years, however development of their optical analogue is more difficult because at shorter wavelengths many noise sources become significant. Current developments toward active optical phased arrays are also hindered by complex designs that typically involve obscuring the array's output.

This thesis progresses toward solving these issues through the evaluation of a scalable, simple architecture with minimal obstruction of the array's output.

It builds on the work of previous Honours student Malcolm King, who demonstrated a preliminary one dimensional version of an active optical phased array. The design encountered two significant problems that rendered it incapable of scaling to large numbers of elements.

The first was that the modulation scheme used was unsuitable as it required the light from each array element to pass through significantly different optical path lengths. With large numbers of elements such an array would become cumbersome, and the array would only function for a single wavelength, limiting its application.

The second was that the architecture caused an initilisation error in the phase measurement that resulted in the array output being unpredictable.

In this thesis we scale the design to two dimensions and solve these two problems. Theoretical calculations are first presented, assessing the viability of the design. The design is deemed viable and tolerances for necessary parameters for the design are suggested. Following this, results from testing aspects of the design in an optical experiment are presented. These results include the successful demonstration of a novel modulation scheme resolving the issues in King's approach, and technique for resolving the phase measurement problem. We present a controller capable of locking the relative phase between elements of the array to within $12\,\mu$Cycles and use this to show beam steering in two dimensions.

# Contents

# Introduction

## 1.1 Motivation

The ability to control the relative phase of elements of an array of microwave, or radio wave emitters has seen many useful applications. These *phased arrays* utilise interference effects to produce steerable, directional antennas with no moving parts. Phased arrays have seen deployment in radar systems, radio broadcasting [1], radio telescopes [?], and in 3D imaging [?]. The development of an optical analogue of such a device could see a similarly broad domain of use. Indeed, should such an array be developed, it would see application in laser radar systems [2], optical communication networks [3, 4], and high power beam combining [5]. Of these possible applications, this thesis is motivated by beam steering for the Gravity Recovery and Climate Experiment (GRACE), and high power beam combining for space debris deorbiting.

The GRACE mission measures the gravitational field of the Earth through use of a microwave interferometer between two satellites orbiting synchronously. In 2017 the satellites will be replaced with those of the GRACE follow-on project, which, together with the microwave ranging system, will trial the first inter-spacecraft laser interferometer. The wavelength of light is of the order of micrometres, far smaller than the centimetre wavelengths of microwaves, implying the laser interferometer may increase the precision of measurements by a factor of 20. However, fluctuations in the position of the satellites requires active beam steering to keep the interferometer aligned [6]. While this could be accomplished with a mechanical mirror, such mirrors are more prone to failure, and not as fast as an optical phased array beam steering device.

The second motivation addresses the problem of man made space debris. Space debris is becoming an increasing problem for new satellites and astronauts. As the debris is generally traveling at relative velocities of roughly 12 km/s even a small fleck of paint presents a hazard [7]. If the problem is not addressed, collisions between debris will cause exponential growth in their number as can be seen in figure 1.1 [8]. If this occurs, the density of space debris will be so high it will render some orbits unusable.

One proposed solution to this problem utilises a laser beam of the order of 100 kW focussed onto a piece of debris. Through a combination of surface ablation of the debris, and photon pressure, the piece of debris may be slowed enough to be deorbited entirely in only a few passes [7]. As thermal effects limit the increase of individual laser power, combining multiple lasers presents the most plausible method of attaining the power required[5]. This is challenging because the lasers must be combined such that they interfere constructively on the target. The effects of atmospheric turbulence further complicates matters by altering the wavefront. Correctly implemented, an optical phased array will resolve these issues.
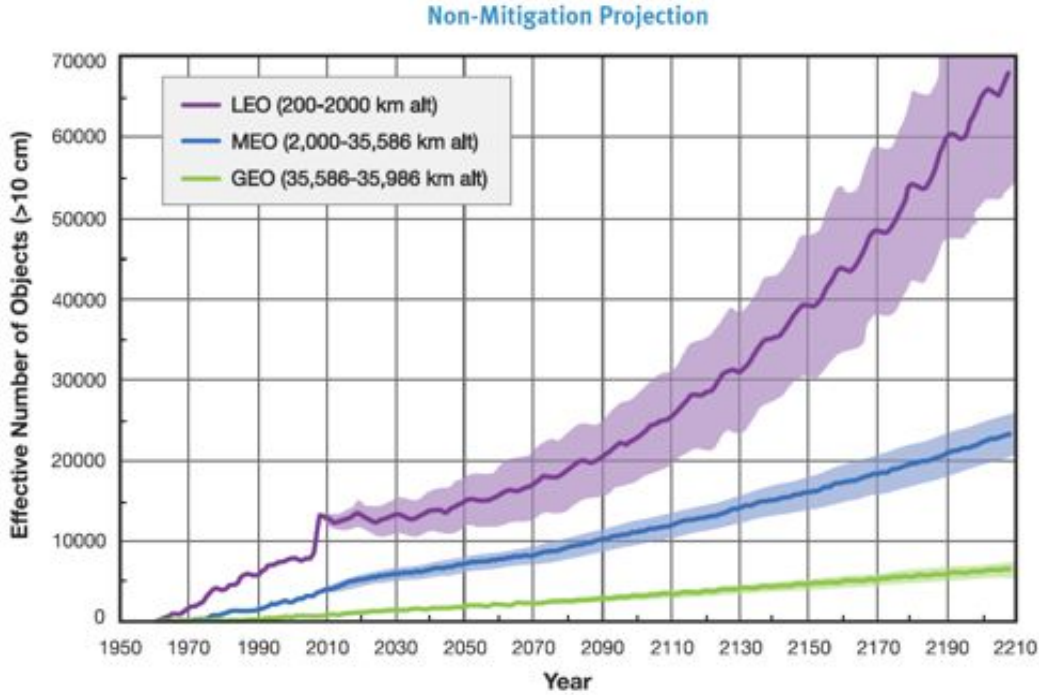
**Figure 1.1:** Predicted numbers of objects in various orbits over time (Low Earth Orbit, Medium Earth orbit and the GEOsynchronous orbit). Image courtesy of Craig Smith, EOS.

## 1.2   Optical phased arrays

An optical phased array is a two dimensional array of light sources with control over the relative phase between each element. The wavefront exiting the device may be modified, permitting arbitrary beam forming. This is illustrated in figure 1.2. Part (a) of this figure demonstrates the null case, with all emitters in phase. Part (b) demonstrates the capacity of such an array for beam steering. It shows an array where each element radiates with a phase different from its neighbours such that there is a linear phase gradient over the array as in figure 1.2 (b). This results in the net wavefront being a planar wave at some angle. The angle can be changed by altering the phase gradient across the array, thus permitting beam steering. Similarly, more exotic phase profiles may be imposed, such as that of a lens (figure 1.2 (c)), allowing the laser beam to be focussed. The wavefront may also be changed in this manner to correct, in advance, for atmospheric turbulence. When multiple sources are combined this way the technique is called *coherent beam combining*.

The main challenge with moving from microwave to optical phased arrays comes from the fact that optical wavelengths are of the order of $1\,\mu$m, which is sufficiently small to be affected by thermal fluctuations. Through thermal expansion of components in the array these fluctuations change the path length of light incident on the array, adding unwanted noise to the phase. The phase must be controlled to a fraction of a wavelength [5], thus it is necessary to account for this noise.

**Figure 1.2:**   The essential function of an optical phased array is captured in the above image. Part (a) Demonstrates the null case, with no phase shift between elements. Part (b) shows how a beam might be steered with a linear phase gradient across the array, and part (c) illustrates how the beam may be focussed by imposing the same phase profile as a lens.
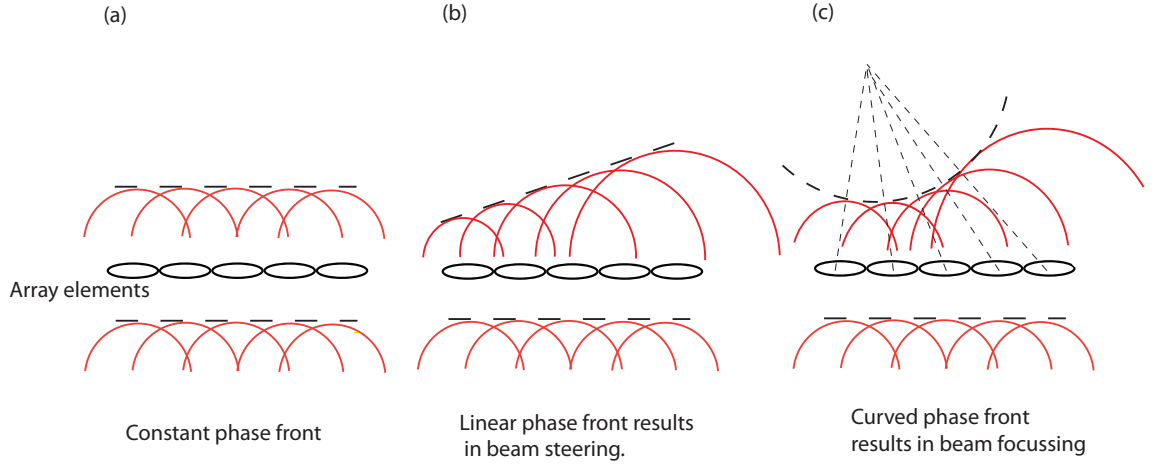
With respect to the use of phased arrays for beam steering in space, a number of approaches have yielded some success. Demonstrations of beam steering with no phase control exist, employing a range of techniques. Of these those that use liquid crystal phase modulators placed in an expanded laser beam with approximately flat wavefronts have been the most successful [9, 10]. However, such arrays have limited bandwidth and it has been suggested they are not suitable for space application [4]. Nor can they be used for high power beam combining. This warrants the development of an alternate approach such as active phased arrays, in which the phase of each array element is detected and controlled with feedback.

The situation is similar in research motivated toward beam combining for high power. There exist a host of passive beam combining methods[11, 12, 13], with no phase control, however these are yet to demonstrate scalability [5], and cannot perform real time adaptive optics to account for atmospheric effects, a requirement for space debris deorbiting.

Of these active methods, there are two main approaches that differ in the method for sensing the phase. The first, termed the multi-dither approach, uses only one sensor for many array elements, and the phase of each element is dithered to optimise the beam quality [5]. This method relies on power from a target in the far field, and is thus slower and less robust than the internally sensing array developed here.

The second approach senses and controls the phase independently for each element [14]. This is the method used in this work. This method has yielded some success with coherent combination of 48 fibres to a phase error of $\frac{\lambda}{30}$ [15]. Further this method is very robust, and has the potential to scale to large numbers of elements. The drawback is that each element must have its own controlling electronics, and the phase detection system is inherently complex, typically requiring optics obstructing the output of the array [14, 5]. This obstruction is a major problem for high power beam combining.

Thus we see that developments in active phased arrays are lacking in a scalable method of sensing the phase with minimal obstruction of the output. To the best of the author's

knowledge, the only work to date that demonstrates an array with minimal obstruction of the output is the work by Vorontsov [16]. However, the solution proposed in this work involves a detector for each emitter, a far less scalable design than that proposed here.

## 1.3   Demonstration of a scalable active optical phased array

This thesis builds on previous work toward an optical phased array by Honours student Malcolm King [**?**]. This work began to address the problem of scalability by employing a phase modulation technique called *digital interferometry* developed by Daniel Shaddock[17]. The modulation technique enables laser beams incident on a single detector to be separated from their time of flight. The geometry demonstrated by King is shown in figure 1.3. In this architecture, the beam from a single laser is first modulated, then split and passed through different fibre lengths. Reflections from a glass reference surface travel back through the same fibre lengths and reach the detector, where they are separated based on their time of flight. The relative phase of these signals is measured, and controlled with the fibre stretchers.

This prototype demonstrated successful phase control and beam steering in one dimension, proving that, in principle, digital interferometry could be used to sense the phase of multiple beams on a single detector with minimal obstruction of the output of the array. This mitigates the need for a large amount of detection electronics, however, the design maintained two significant problems.
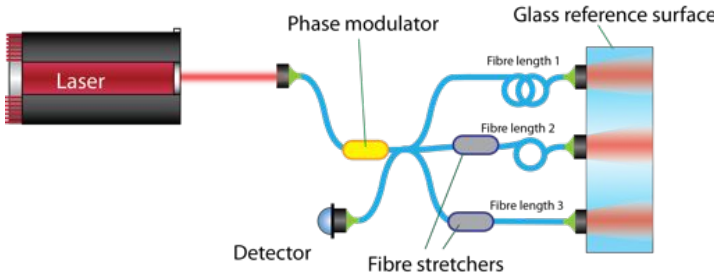


**Figure 1.3:** A simplified form of the architecture that was previously demonstrated for the optical phased array.

The first was that the separation was reliant on different fibre lengths for each element. In the limit of a large number of elements the design would become unnecessarily complex.

The second was more subtle. The path of the back-reflected signals passes through these fibres twice before it reaches the detector. This means that if the length of the fibres resulted in a phase difference of $\pi$ at the reference surface, this difference would be $2\pi$ at the detector. But this cannot be discerned from a relative phase of zero, because of the periodicity of the light. This can cause the phasemeters to initialise in a manner that renders the output of the array unpredictable. For the purpose of discussion, this problem will be called the $\pi$ ambiguity.

In this thesis we solve these two problems with the architecture shown in figure 1.4. The first problem is solved through a novel innovation of the digital interferometry technique that we call *CDMA-based digital interferometry*. It amounts to modulating each beam with a unique label so that the beams may be separated based on their label, instead of their delay. Chapter 5 is concerned with the design, implementation and resulting success of this new technique.

The $\pi$ ambiguity is solved through the addition of another detector. This detector senses light from all beams through the *dark fibre*, an additional fibre placed near the *bright* fibres for the purpose of collecting light. The light from the bright fibres travels to the reference surface, and reflects into the dark fibre. Since all the return beams pass through the dark fibre, the phase noise from this will be common to all beams, and thus will not show up in the relative phase. Thus the signal from the dark fibre will be a measure of the actual relative phase at the reference surface, not twice the relative phase as ing King's experiment.

The feasibility of this solution in a GRACE-like context is evaluated theoretically, and an initial design for a phased array for use in GRACE-like applications is suggested in chapter 3. In this new design we scale the array to two dimensions, as shown in the cross section of figure 1.4. In this array there will be multiple dark fibres, each collecting light from a group of bright fibres. Signals from these dark fibres will be detected on a single detector, and separated using digital interferometry. This will require additional phase modulators on each dark fibre to "label" these beams.

Following the success of the theoretical evaluation of the dark fibre, a new controller, incorporating the CDMA-based digital interferometry is discussed in chapter 4. Also discussed in this chapter are the methods used to correct the $\pi$ ambiguity using the dark fibre. The controller is then tested in an optical experiment, the setup of which is described in chapter 6.

In addition to solving the two problems with the previous architecture, we test the aptitude of the array for two dimensional beam steering. The configuration simulates some aspects of a small part of an anticipated larger array as shown in figure 1.4. These results are discussed in chapter 6.

Because of the simplicity of the design, this demonstration has the potential to alleviate the scalability problems inherent with active optical phased arrays, opening the path to a host of exciting new technologies.
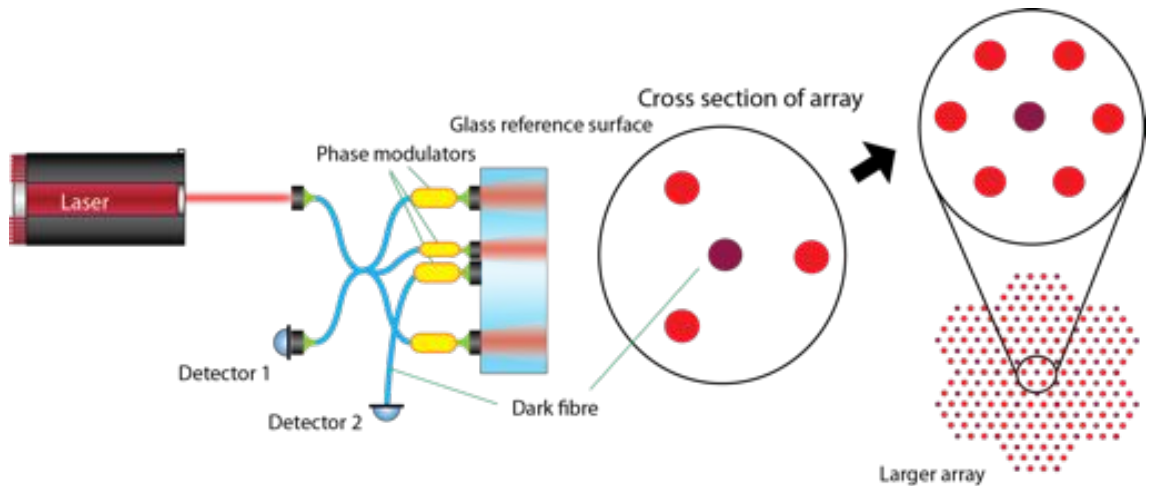


**Figure 1.4**: A simplified form of the architecture that is demonstrated in this thesis.

# Background Theory

In which we introduce the necessary concepts and tools for the description of the majority of phenomena encountered in this thesis.

## 2.1 Interference of light

Maxwell's equations naturally lead to a linear wave based theory of electromagnetic waves. Mathematically it is useful to construct this representation using the complex wavefunction, which comes from solutions to the Helmholtz equation[18]:

$$\nabla^2 U + k^2 U = 0 \tag{2.1}$$

Where $k = \frac{\omega}{c}$ is the wavenumber and $c$ is the speed of light. One such solution is the monochromatic wave. Its complex wavefunction is given by:

$$U(\mathbf{r}, t) = A \exp(-j\mathbf{k} \cdot \mathbf{r}) \exp(j\omega t) = U(\mathbf{r}) \exp(j\omega t) \tag{2.2}$$

Where $\mathbf{r}$ is the position vector, U($\mathbf{r}$)=Aexp(-j$\mathbf{k} \cdot \mathbf{r}$) is the complex amplitude of the wave, $\mathbf{k} = (k_x, k_y, k_z)$ is the wavevector, defined such that $|\mathbf{k}| = k$, $\omega = 2\pi\nu$ is the angular frequency and $\nu$ the frequency of the wave. The argument of complex amplitude gives the phase of light, and its magnitude gives the amplitude.

Because the Helmholtz equation is a constant-coefficient linear differential equation, light satisfies the principle of superposition. That is if $U_1$ and $U_2$ are complex representations of a beam of light, then so is $U_1 + U_2$. It also means that solutions are unique[19], so if we find a solution for a particular set of boundary conditions, it is the only solution. This means that $U_1 + U_2$ *is* the solution if two waves are present.

Another feature of this model is that the intensity of light is given by the absolute square of the complex amplitude:

$$I(\mathbf{r}) = |U(\mathbf{r})|^2 \tag{2.3}$$

Because intensity is something we can easily measure, it is interesting to find the intensity of two beams of monochromatic light present in the same region of space. If we have two waves with complex amplitudes $U_1$ and $U_2$ and intensities $I_1$ and $I_2$, then the intensity of

the resulting wavefunction is:

$$
\begin{aligned}
I &= |U_1 + U_2|^2 \\
&= (U_1 + U_2)(U_1^* + U_2^*) \\
&= |U_1|^2 + |U_2|^2 + U_1 U_2^* + (U_1 U_2^*)^* \\
&= I_1 + I_2 + 2Re(U_1 U_2^*)
\end{aligned}
$$

If these two waves were monochromatic plane waves, their complex amplitudes would be: $U_1 = \sqrt{I_1}\exp(j\phi_1)$ and $U_2 = \sqrt{I_2}\exp(j\phi_2)$, where $\phi_1 = \mathbf{k_1}\cdot\mathbf{r}$ and $\phi_2 = \mathbf{k_2}\cdot\mathbf{r}$ are the phases of each wave. This gives our net intensity as:

$$
I = I_1 + I_2 + 2\sqrt{I_1 I_2}\cos(\phi_1 - \phi_2) \tag{2.4}
$$

Thus the resultant intensity is dependent on the phase of the two waves. If the two waves were of equal intensity $I_1$, then this dependence can result in the intensity fluctuating between zero and $2I_1$ depending on the phase difference. This is the principle of interference. If the phase difference is an even multiple of $\pi$, then the intensity will be maximised, and we say that the two beams constructively interfere. If the phase difference is and odd multiple, the intensity is minimised, and the two beams are said to destructively interfere.

## 2.2 Optical phased arrays

As seen above, in the case of the overlap of two monochromatic, coherent, waves the intensity distribution can depend strongly on the phase. Thus the phase provides a convenient tool with which to control the intensity. Controlling the phase of light to control the intensity distribution is what a phased array does.

An analysis of the double slit experiment shows how a 1 dimensional array with 2 elements might work. A diagram of this situation is shown in figure 2.1. Two beams pass through phase modulators that control the phase of each, and exit each slit. Suppose both rays reach some point in the far field after traveling distance $L$. Then both will be approximately parallel at some angle $\vartheta$ to the horizontal. We can see from the figure that the difference in the distance travelled between these rays is $d\sin(\vartheta)$, where $d$ is the separation between the elements.
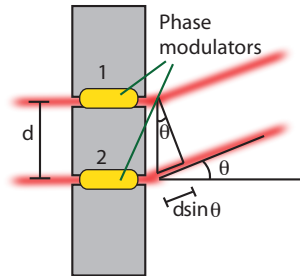


**Figure 2.1:** Diagram of a one dimensional optical phased array. In the limit of large numbers of elements one can treat such an array as a Bragg grating.

The phase due to the propagation for these monochromatic plane waves is given by:

$$\phi = \mathbf{k} \cdot \mathbf{r} = \frac{2\pi L}{\lambda} \tag{2.5}$$

The phase of each element at our point in the far field will be given by the sum of the phase due to the propagation and the phase $f_1$ and $f_2$ we impose on each element from the phase modulators, that is:

$$\phi_1 = f_1 + \frac{2\pi L}{\lambda} \tag{2.6}$$

$$\phi_2 = f_2 + \frac{2\pi L}{\lambda} + \frac{2\pi}{\lambda} d \sin(\vartheta) \tag{2.7}$$

Assuming that both rays may be approximated by monochromatic plane waves, we know the interference will be affected by the difference in these phases, let $\Delta f = f_1 - f_2$:

$$\phi_1 - \phi_2 = \Delta f - \frac{2\pi}{\lambda} d \sin(\vartheta) \tag{2.8}$$

Now recall the waves will constructively interfere when $\phi_1 - \phi_2 = 2n\pi$ for some integer $n$, and destructively interfere when $\phi_1 - \phi_2 = (2n+1)\pi$. Because the phase of light depends on the angle $\vartheta$, we arrive at the conclusion that the intensity is also a function of this angle. This causes the traditional fringe pattern seen in the double slit experiment. But now we have control over this relative phase through our phase modulators. Thus we may control the angle at which a peak occurs by adjusting $\Delta f$. The relative phase required to steer a peak to a desired angle $\vartheta$ is:

$$\Delta f - \frac{2\pi}{\lambda} d \sin(\vartheta) = 2n\pi \rightarrow \Delta f = 2n\pi + \frac{2\pi}{\lambda} d \sin(\vartheta) \tag{2.9}$$

In a larger one dimensional array one simply ensures that the relative phase between any two elements is that given by the above, and the situation is the same for a two dimensional array. This amounts to placing a phase gradient over the array.

## 2.3   Gaussian modes

A better approximation of the light coming from a laser is that of the Gaussian mode. The complex envelope of a Gaussian beam propagating along the z axis is given by [18]:

$$U = U_0 \frac{r_0}{r(z)} \exp\left[-\frac{(x^2 + y^2)}{r(z)^2} - j\left(kz + k\frac{(x^2 + y^2)}{2R(z)} - \zeta_t(z)\right)\right] \tag{2.10}$$

where $k = \frac{2\pi}{\lambda}$, $U_0 = \sqrt{\frac{2P_0}{\pi r_0^2}}$ is the amplitude of a mode of power $P_0$. $r_0$ is the waist radius as indicated in figure, and $r(z)$ given by:

$$r(z) = r_0\sqrt{1 + (\frac{z}{z_R})^2} \tag{2.11}$$

This is the radius at distance $z$ from the waist. The radius is defined such that $(1-e^{-2})P_0 \approx 0.86P_0$ is contained within a circle of radius $r(z)$. $z_R$ is given by:

$$z_R = \frac{\pi r_0^2}{\lambda} \tag{2.12}$$

and is called the *Rayleigh range.* This is the distance at which $r(z) = \sqrt{2}r_0$.

$$\zeta_t(z) = \arctan(\frac{z}{z_0}) \tag{2.13}$$

Is called the *Gouy phase.* Finally:

$$R(z) = \begin{cases} \infty & z = 0 \\ z\left[1 + \left(\frac{z_0}{z}\right)^2\right] & z \neq 0 \end{cases} \tag{2.14}$$

This is the radius of curvature of the wavefronts (lines of constant phase) of the mode. For large distances away from the waist, that is $z \gg z_0$, the beam diverges with angle:

$$\vartheta = \frac{2\lambda}{\pi r_0} \tag{2.15}$$

Thus we see that beams with small waist radii diverge more rapidly than large beams. This will become relevant when considering the transmission of beams over large distances, as in GRACE. When working with lasers it is also of use to note that only two parameters are required to completely characterise a Gaussian mode. Usually these are the waist position and waist radius.
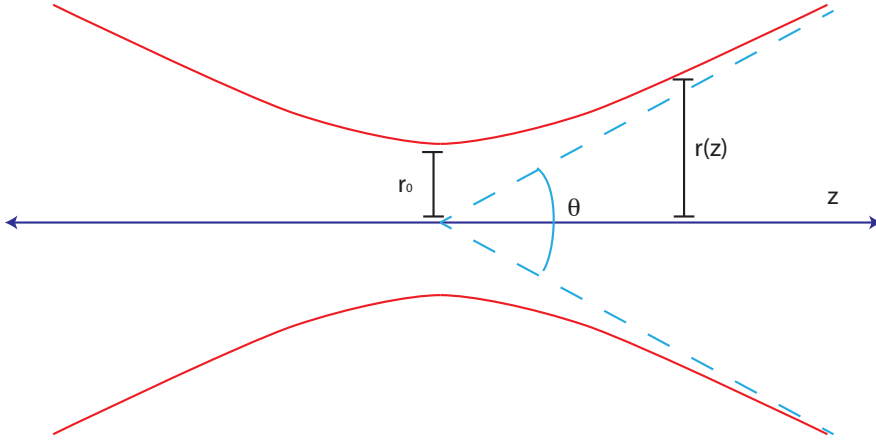


**Figure 2.2**: Diagram showing the important characteristics of a Gaussian mode.

## 2.4   Optical metrology

### 2.4.1   Heterodyne interferometry

For an optical phased array we are primarily concerned with the measurement of the phase of light from many individual sources. To accomplish this we will use a technique called *heterodyne interferometry*[20]. This functions as follows: Suppose we have some light of which we would like to know the phase. We call this beam the *science beam.* Suppose we combine this with another, the *local oscillator,* that has been shifted slightly in frequency. Let the science beam be represented by:

$$E_s(t) = A_s e^{i(\omega t + \phi_s)} \tag{2.16}$$

where $A_s$ is some real constant denoting the amplitude of the signal, $\omega$ is the frequency of the laser and $\phi_s$ is the phase we would like to know. We represent the local oscillator by:

$$E_{LO}(t) = A_{LO}e^{i((\omega-\omega_h)t+\phi_{LO})} \tag{2.17}$$

Where $A_{LO}$ is another amplitude, $\omega_h$ is the frequency shift of the local oscillator; the *heterodyne frequency*. Again we refer to equation 2.4. The signal on our detector will be:

$$D = A_{LO}^2 + A_s^2 + 2A_sA_{LO}\cos(\omega_h t + \phi_s - \phi_{LO})$$

Neglecting the DC components of the signal, defining a phase reference point such that $\phi_{LO} = 0$. We find that the time varying component is:

$$D = 2A_sA_{LO}\cos(\omega_h t + \phi_s) \tag{2.18}$$

Note that $\omega_h$ is generally a frequency much lower than that of the laser, which is good because it means we can observe it on the detector. Thus we obtain a signal with the same phase as that of the light signal we wish to measure. All that remains is to somehow extract this phase information.
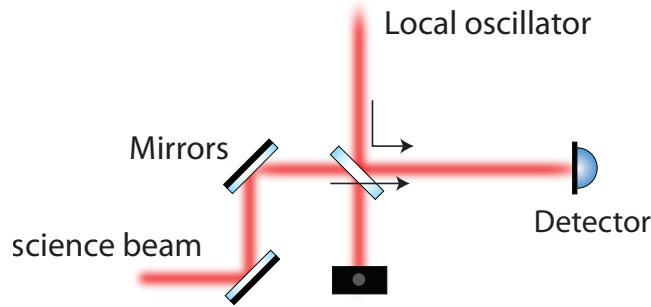


**Figure 2.3:** Diagram illustrating the combination of two beams in the case of heterodyne interferometry.

### 2.4.2 Phase-locked loops

Extracting the phase of a sinusoidal signal is accomplished by a phase-locked loop. A phase-locked loop is an algorithm that can be implemented digitally to process the signal from the detector. They essentially function by keeping their own oscillating signal with the expected frequency of the beatnote, and comparing this with the input signal. If their is a difference in the phase of these signals, the phase-locked loop adjusts its oscillator to match the input. In this way a phase-locked loop may track the phase of a signal from the moment it is initialised. By recording this phase, one recovers the phase of the light.

### 2.4.3 Digital interferometry

We need to measure the phase of multiple beams, however. One method of doing this could be to simply combine each beam with the local oscillator on a separate detector, however for a large array, with many elements, this would become expensive and complicated. It

turns out we may use only one detector, if we correctly prepare the light before it passes through the system and onto the detector.

The technique, called *digital interferometry* was developed by [17]. It allows for multiplexing of signals on a single detector by effectively "labeling" each beam of light. Consider two beams of light of which we wish to measure the phase. Suppose we represent the complex amplitude of each beam by the following, but we add in a phase modulation of $c(t)\pi$, where $c(t)$ is a pseudorandom string of $\pm 1's$. For the purpose of this thesis, we call each 1 in the sequence a *chip.* The frequency with which the code changes to the next number in its sequence is called the *chip frequency.*

With these codes, our complex amplitudes become: $E_1 = A_1 e^{-i(\phi_1+c(t)\pi)}$ and $E_2 = A_2 e^{-i(\phi_2+c(t)\pi)}$. Now suppose we propagate the beams through different optical paths and onto the same detector such that they pick up delays $\tau_1$ and $\tau_2$ respectively. The electric fields then become:

$$E_1 = A_1 e^{-i(\phi_1+c(t-\tau_1)\pi)} = A_1 c(t-\tau_1)e^{-i\phi_1} \tag{2.19}$$

$$E_2 = A_2 e^{-i(\phi_2+c(t-\tau_2)\pi)} = A_2 c(t-\tau_2)e^{-i\phi_2} \tag{2.20}$$

where we have noticed that $e^{i\pi} = -1$. If we mix both signals with a local oscillator on the detector, we know from equation 2.18 the signal will be proportional to:

$$D = A_1 c(t-\tau_1)\cos(\omega_h t - \phi_1) + A_2 c(t-\tau_2)\cos(\omega_h t - \phi_2) \tag{2.21}$$

Now suppose we multiply the detector signal by $c(t-\tau_1)$. Since the code is made of only $\pm 1$ we note that $c(t-\tau_1)c(t-\tau_1) = 1$, but $c(t-\tau_1)c(t-\tau_2)$ remains random. This means:

$$
\begin{aligned}
Dc(t-\tau_1) &= A_1 c(t-\tau_1)c(t-\tau_1)\cos(\omega_h t - \phi_1) + A_2 c(t-\tau_1)c(t-\tau_2)\cos(\omega_h t - \phi_2) \\
&= A_1 \cos(\omega_h t - \phi_1) + A_2 c(t-\tau_1)c(t-\tau_2)\cos(\omega_h t - \phi_2)
\end{aligned}
$$

From this, the signal $A_1 \cos(\omega_h t - \phi_1)$ may be recovered, while the second signal remains as random noise that may be filtered out.

One set of pseudorandom code that function well for this technique are called *m-sequences.* M-sequence based digital interferometry was used in the previous implementation of digital-interferometry based optical phased array [**?**]. In this design, the signal from each element had to be delayed by a different amount so as to be separated from the other signals. This was accomplished by adding long stretches of fibre before each element. This is not a scalable design, because with many elements the array would become unnecessarily large.

In this thesis we investigate the application of a digital interferometry in a slightly different way to resolve this issue. We borrow a technique used in telecommunications to separate channels in wireless networks called *Code Division Multiple Access* (CDMA). Further discussion of this investigation is detailed in chapter 5.

An important property of these codes is their *Autocorrelation.* For the purpose of this thesis this is defined to be the dot product of the code with itself over the period of the code. More explicitly, for a code of duration $T$ with some delay $\tau_1$ the autocorrelation is:

$$\int_0^T c(t-\tau_1)c(t-\tau_1)dt \tag{2.22}$$

The *cross correlation* will also become important in chapter 5. For two distinct codes $c_1$

and $c_2$, both with duration $T$, the cross correlation is the dot product between the two, or:

$$\int_0^T c_1(t)c_2(t)dt \tag{2.23}$$

## 2.5   Significant pieces of equipment

Key to the operation of the experiments conducted were the following pieces of technology.

### 2.5.1   Electro-optic Phase modulators

An electro-optic phase modulator is a device that modulates the phase of light. It's function is based on the Pockels effect, in which one observes a linear change in the refractive index with an applied voltage. An important characteristic of such devices is the voltage at which the phase is shifted by half a wavelength. This is called the *half-wave voltage* and will be denoted by $V_\pi$. Once one knows this parameter, the expected phase modulation in radians for a given applied voltage is:[18]

$$\phi = \phi_0 - \pi\frac{V}{V_\pi} \tag{2.24}$$

Where $\phi_0$ is some initial phase value.
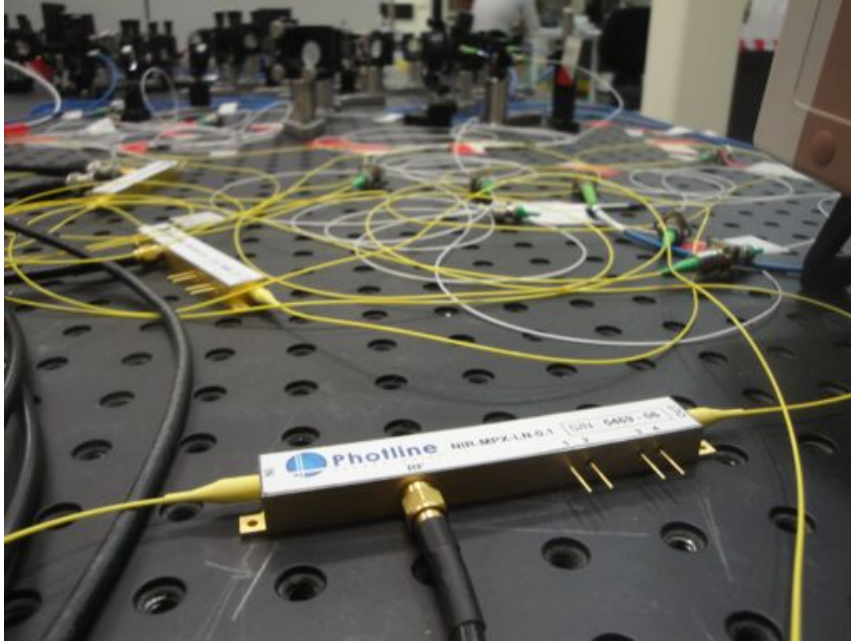


**Figure 2.4**: An image of an EOM used in this experiment.

### 2.5.2   Acousto-optic modulator

The heterodyne interferometry setup used in this experiment required the reference beam be frequency shifted to obtain a beatnote. This frequency shifting was accomplished through the use of an acousto-optic modulator (AOM). An AOM is a nonlinear element consisting of a crystal of glass or quartz through which light is passed as in figure 2.5. A piezoelectric device creates sound waves within the crystal that create a moving periodic

profile in the refractive index. The light diffracts through this grating in a manner similar
to a Bragg grating. However because the grating moves, the photons effectively collide
with the moving planes of the density gradient. This results in a doppler-shift in the light's
frequency. The result is a number of beams exiting the crystal with frequencies shifted by
multiples of the frequency of sound in the crystal.
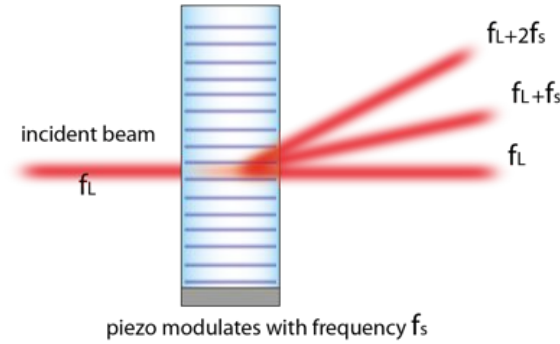


**Figure 2.5**: Diagram illustrating the function of an AOM

### 2.5.3   Field Programmable Gate arrays

In order to implement a sufficiently fast controller to suppress phase noise, a sufficiently
fast processing unit is needed to accomplish the digital signal processing required. This
can be done with a Field Programmable Gate Array's (henceforth FPGA) .

FPGA's are integrated circuits that are able to be re-structured in the field. They
consist of arrays of logic blocks that can be linked together as desired to perform many
complex logical operations. They have distinct advantages over conventional hardwired
chips, since they are inherently highly concurrent, can be reprogrammed to fix bugs,
and prototype designs implemented on them can be easily transferred to mass producible
hard-wired IC's. Their highly concurrent nature makes them ideal for the digital signal
processing problem at hand, as ultimately many phase channels will need to be controlled
independently and concurrently.

It is important to note that like all computers FPGA's have an internal clock that
synchronises each operation that occurs within the device. Ideally functions such as addi-
tion and multiplication happen at discrete intervals that coincide with ticks of the internal
clock, or multiples thereof.

It is also important to note that FPGA's are limited in the types of numbers they can
process rapidly. The system used in this thesis was the National Instruments PXI plat-
form, and programmed in Labview -a graphical programming language made by National
Instruments. This system maintained the restrictions that in order for fast operation
(40 MHz), the only data type that could be processed were integers of 8, 16, 32 and 64
bits in size. Further, general multiplication and division operations were inefficient, thus,
where possible, these were replaced with *bit shifts,* or multiplication by powers of two.
Multiplication by powers of two is fast on an FPGA due to the fact that numbers are
stored in binary.

# Optical Head Design

Figure 3.1 shows the expected configuration of the array we are investigating. It consists of some fibres held in place by some material, nominally aluminium, with their ends incident on a glass reference surface. This assembly, comprising the material supporting the fibres of the array, together with the reference surface, makes up the *optical head*. It will consist of a number of bright fibres, and necessarily their adjacent dark fibres.

One of the primary aims of this thesis is to ascertain whether the dark fibre solution is viable. In this chapter we develop theoretical models to test the performance of the dark fibre for a GRACE-like application. We find that it is viable, and suggest a preliminary design and associated tolerances.
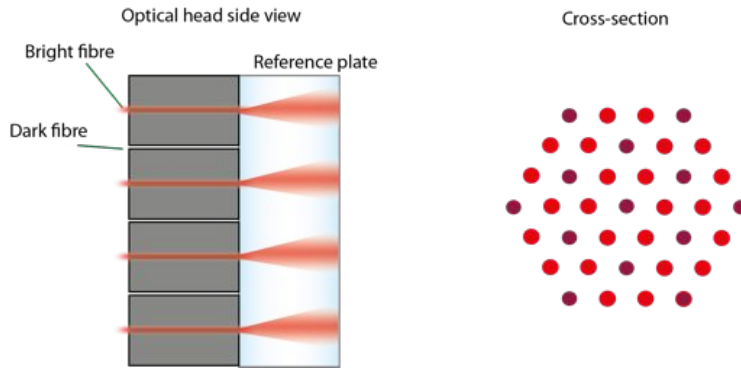


**Figure 3.1**: The optical head.

## 3.1   Further motivation

In both GRACE-like applications, and space debris deorbiting, a significant motivating factor for coherent combination of light comes from the possibility of much higher power transfer ratios with a large field of view. This can be seen from the following calculation.

Suppose we take an N element array with a single source of power $|P|^2$ (and electric field amplitude $P$), and maintain the goal of transferring power to a small point in the far field as illustrated in situation (A) of figure 3.2. We assume that we are in the regime where the divergence of the beam is much larger than the angle subtended by the receiving point. Now suppose that the amplitude of the electric field coupled into the small aperture from a single element is $\epsilon E_i$, where $E_i$ is the electric field of the $i^{th}$ element and $\epsilon_i$ is the coupling factor, or the fraction of electric field on this point. Note that $\epsilon$ is small and less than one in these limits. Suppose further that the power divides evenly between the

elements, we then have

$$N|E_i|^2 = |P|^2 \rightarrow |E_i| = \frac{|P|}{\sqrt{N}} \rightarrow E_i = \frac{|P|}{\sqrt{N}}e^{j\phi_i} \tag{3.1}$$

where $\phi_i$ is the phase of the light from element $i$. If we then combine these elements at a point in the far field, the electric field will be the sum of the contributions from each element:

$$\sum_{i=1}^{N} \epsilon E_i = \sum_{i=1}^{N} \frac{\epsilon P}{\sqrt{N}}e^{j\phi_i} \tag{3.2}$$

Now assuming that the phase is adjusted by the array such that each element constructively interferes at the point in the far field, we may set the phases to be equal, and the power at the point becomes:

$$P_p \equiv |\sum_{i=1}^{N} \frac{\epsilon P}{\sqrt{N}}|^2 = N\epsilon^2|P|^2 \tag{3.3}$$

which is equal to N times the power transmitted from a single element alone[1]. Thus, when constructively combined, we see that the power transfer efficiency scales linearly with the number of elements in the array, independent of the geometry.

Similarly, an identical phase array can be used to improve the power coupling factor at the receiver. In this case, illustrated in part (B) of figure 3.2, we have the ability to alter the phase of the light at the receiving aperture. The power at each of the elements of the receiving aperture will be given by the total power received divided by the number of elements, thus the electric field at each of these elements is:

$$E_{ri} = \sqrt{\frac{P_p}{N}} = \epsilon|P|e^{j\phi_i} \tag{3.4}$$

Again, assuming that the phase is controlled to ensure coherent recombining, we find the power at the detector due to the sum of these elements as:

$$P_d = |\sum_{i=1}^{N} \epsilon|P||^2 = N^2\epsilon^2|P|^2 \tag{3.5}$$

equal to $N^2$ times the power transmitted from a single element alone, and again independent of the array geometry. Thus regardless of the details of the emitter's and receiver's spatial distribution, some major benefits can be gained purely from phase control. With respect to the GRACE-like application, the $N^2$ scaling is of relevance, strongly motivating its use in this context.

With respect to beam combining for space debris deorbiting, the scaling is further improved if we use multiple lasers, since we no longer reduce the power by a factor of $\sqrt{N}$

---

[1]If $\epsilon = 1$ this result violates conservation of energy. However $\epsilon$ cannot equal one in the far field limit with an aperture small compared to the divergence. Heuristically, $\epsilon = 1$ would correspond to the situation where the receiving aperture is identical to the transmitting aperture and zero distance away. It is not physically possible to construct this situation for two emitters of the same size without changing the size of the aperture.

with increasing elements. In this case the power at a point becomes:

$$P_p \equiv |\sum_{i=1}^{N} \epsilon P|^2 = N^2 \epsilon^2 |P|^2 \tag{3.6}$$

Yielding a scaling of $N^2$.
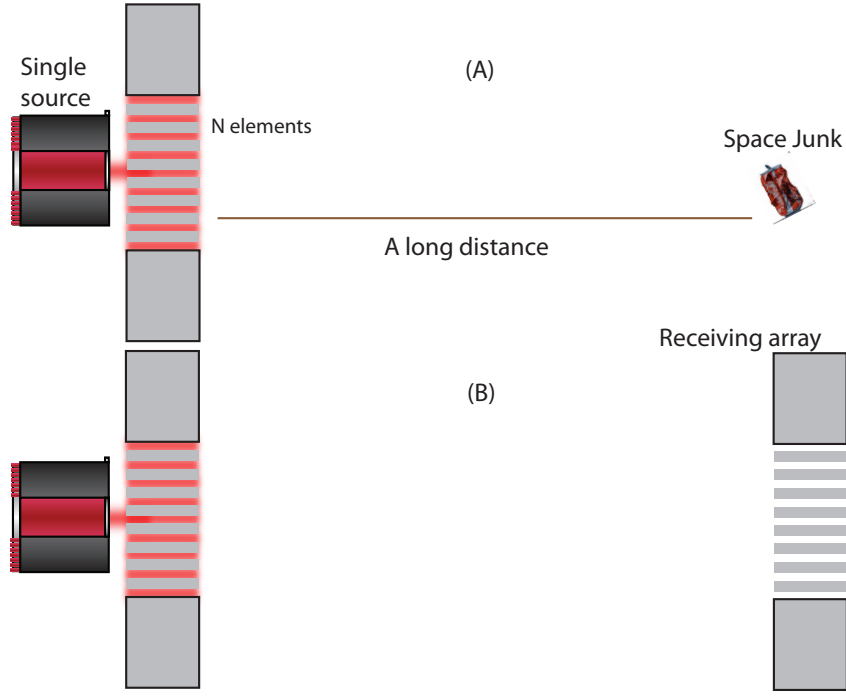


**Figure 3.2**:   An N element array

## 3.2   Initial intuition

Now we develop some intuition for the purpose of selecting design parameters. First consider the simplest case of a one dimensional array of identical sources shown in figure 3.3. Consider rays from the topmost and middle elements that both reach some point in the far field. In the far-field limit, both rays are parallel at some angle $\vartheta$ to the horizontal. We can see from the figure that the path length difference between these rays is $\frac{w}{2}\sin(\vartheta)$, where $w$ is the total width of the array. If we suppose that these rays interfere destructively, then the angle $\vartheta$ to the nearest minimum is:

$$\frac{w}{2}\sin(\vartheta) = \frac{n\lambda}{2} \rightarrow \vartheta \approx \frac{\lambda}{w}, \quad (n \in \mathbb{Z}) \tag{3.7}$$

The central peak width is given by twice this angle:

$$\vartheta_{pw} \quad \approx \quad \frac{2\lambda}{w} = \frac{2\lambda}{(N-1)s} \tag{3.8}$$

Which gives a measure of the width of the central peak as a function of both the number of array elements $N$ and their separation $s$. It indicates that increasing the total array

width, either by increasing the number of elements or by increasing emitter separation decreases the width of the central peak.

Further intuition may be gleaned from this simple picture by considering the distance to the nearest large peak. Take two adjacent elements, then suppose they are constructively interfering at a point in the far field at angle $\phi$ to the horizontal. Then by the same approximation as above:

$$s \sin(\phi) = n\lambda \rightarrow \phi \approx \frac{\lambda}{s}, \quad n \in \mathbb{Z} \tag{3.9}$$

With the result that the distance between these maxima is $\frac{\lambda}{s}$. As all adjacent elements will be in phase at these points, these will be the largest maxima in the fringe pattern. But as the distance to the nearest minima is far smaller than this, we should expect to see that the overall intensity distribution consists of these larger peaks separated by smaller peaks, and dropping to zero at multiples of $\vartheta$. We do indeed see this, the output of a linear array of 10 elements with a separation $s = 300\,\mu\mathrm{m}$, fibre width of $6.2\,\mu\mathrm{m}$, and equal power is shown in figure 3.4. For the purpose of further discussion, we will henceforth refer to the larger peaks as *Bragg peaks* (in analogy with those in X-ray diffraction) and any smaller undesirable peaks as *side lobes*.

## 3.3  Specifications: GRACE

Now we present order-of-magnitude design constraints inspired by the requirements for application in a GRACE-like setting. Below are explanations behind the choice of constraints.

### 3.3.1  Uncommon Dark fibre phase error

The phase of light reflected into the dark fibre will be altered by the distance that it has to travel from the bright fibre to the dark fibre in the optical head. If this additional phase is different for the light from the two bright fibres, then this will add to the error in the relative phase measurement of the two fibres. Such an error might be caused by an expansion of the fibre casing due to temperature. Referring to figure 3.5, if the block marked T1 is a different temperature to T2, then it would expand differently, causing a difference in the path to the dark fibre. We need the dark fibre to resolve the relative
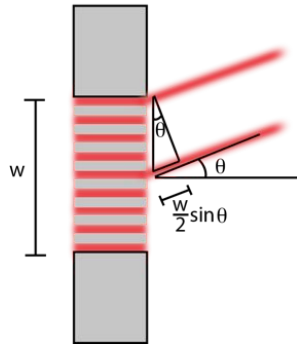


**Figure 3.3:** Diagram of a one dimensional optical phased array. In the limit of large numbers of elements one can treat such an array as a Bragg grating.
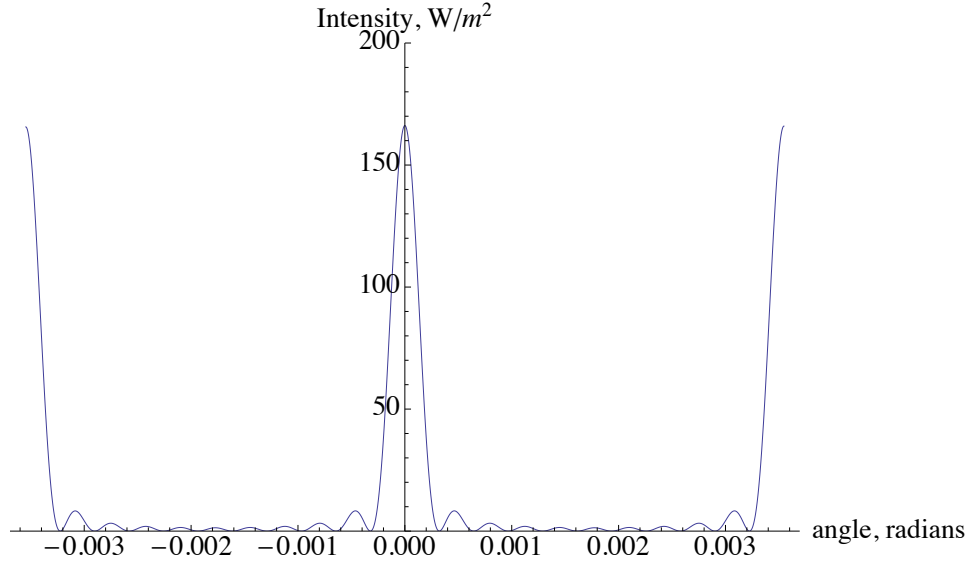
**Figure 3.4:** Output of a 10 element linear array of Gaussian modes in the far field with a waist radius of $3.3\,\mu$m, separated by $300\,\mu$m, with a total power of $1\,$W and at a distance of $2\,$m. This plot was obtained by numerically summing 10 gaussian modes with the appropriate parameters in mathematica.

phase of the light in the two bright fibres to a resolution of at least $\frac{\pi}{2}$ (see chapter 4 for more detail), when compared with the bright fibre. This places an upper bound of $\frac{\pi}{2}$ on this parameter.

Note that while static offsets may be calibrated out, thermal expansions that are not common between the two paths may create dynamic offsets that cannot be calibrated for, for example if the dark fibre moves laterally to become closer to one bright fibre and away from another. Thus there are two performance parameters here, the static uncommon phase, and the dynamic uncommon phase. Because the expected uncommon phase offset is:

$$dφ ≈ Δs × \frac{d}{ds}(φ_u(s)) \tag{3.10}$$

The dynamic uncommon phase is quantified by the derivative $\frac{d}{ds}(φ_u(s))$.

Assuming that the optical head is made of aluminium, which has a linear coefficient of thermal expansion of $α = 23 × 10^{-6}\,$K$^{-1}$ [21], and that the temperature difference is no more than $1\,$K between the bright and dark fibres, we find that for some nominal spacing of $300\,\mu$m we can expect length differences of $\sim 7\,$nm. As we require the phase difference to be no more than $\frac{\pi}{2}$ the rate of change of phase error must be: $\frac{d}{ds}(φ_u(s)) < \frac{\pi}{2×7×10^{-9}} ≈ 20 × 10^9\,$rad $\cdot$ m$^{-1}$.

Note that aluminium has a relatively high coefficient of thermal expansion compared to other materials that could be used to hold the fibres, such as glass ($α = 8.5×10^{-6}\,$K$^{-1}$), silicon ($α = 2.6 × 10^{-6}\,$K$^{-1}$).
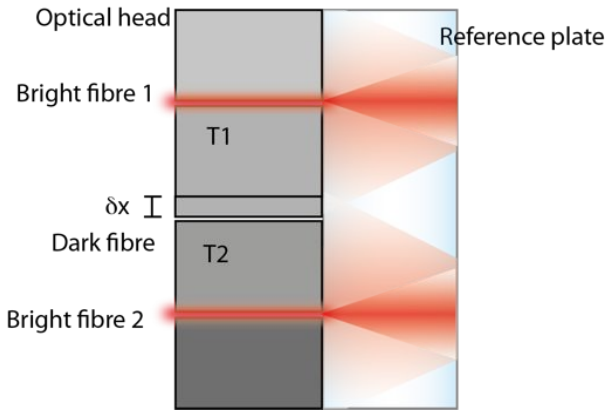
**Figure 3.5:** Diagram illustrating a source of phase error. The block marked T1 is at a different temperature to T2, thereby causing it to expand, and resulting in a path length difference between the paths from each bright fibre to the dark fibre. Static errors may be calibrated out, but dynamic errors will couple into the dark fibre phase measurement noise.

### 3.3.2 Dark fibre power coupling

We need a signal capable of detection from the dark fibre. From the experience of our group, at least $10^{-10}$ W was chosen to be the lowest detectable power for the dark fibre. With a reflection coefficient of $1 \times 10^{-3}$, and an input power of $10^{-2}$ W, this implies that the power transfer efficiency must be greater than $10^{-5}$. The power transfer efficiency will be called the *coupling factor*.

### 3.3.3 Bright fibre power coupling

There will also be light coupled between bright fibres. This light could cause interference if it were to reach the direct back reflection detector, as there could plausibly be two light sources with the same code but from different paths. However this was not deemed to be a problem, as the light should destructively interfere due to the symmetry of the situation, which is analogous to a Sagnac interferometer. This may be seen from figure 3.6.

The phase of the light reaching the detector from beam 1 by reflecting down the beam 2 path will be $\phi + \pi$, where $\phi$ is the phase offset from the total optical path and $\pi$ is the reflection phase change from the mirror and the reference surface. However the phase of light from beam 2 reflecting down the path of beam 1 and onto the detector will have a phase of $\phi + 2\pi$. Thus the two beams will be $\pi$ out of phase and destructively interfere, except in the instance that there is some asymmetry in the path, or the beamsplitter ratio. This path length should be on the order of $1$ m, so asymmetries would have to occur on a timescale of $\frac{1}{3 \times 10^8} \approx 3$ ns, corresponding to frequency noise of the order of $300$ MHz. Such noise is likely to be small in magnitude. Further, the power coupled between bright fibres will be far less than the signal from the direct back-reflection. Thus this problem was neglected.
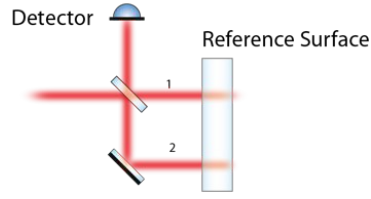
**Figure 3.6:** Coupling between bright fibres does not present a problem because of the Sagnac effect.

### 3.3.4 Power transfer efficiency

This is defined to be the ratio of the input laser power to the power at the desired steering point. This amounts to the minimum power required at the receiving satellite for the laser ranging instrument. This is approximately $100\,\text{pW}$. Since the laser provides $25\,\text{mW}$, this gives a lower bound on the efficiency of $4 \times 10^{-9}$.

### 3.3.5 Beam steering range

As per the requirements on GRACE, the steering range should be $2\,\text{mrad}$ [22].

### 3.3.6 Variance peak position

This is defined to be the maximum fluctuation in the peak position. This is constrained to be much less than the total peak width.

### 3.3.7 Summary

The desired performance of the optical phased array for application to GRACE is summarised in table 3.1.

| Output characteristic | Constraint |
|:---:|:---:|
| Uncommon dark fibre phase error | Static error: $< \frac{\pi}{2}$, Dynamic error: $< 20 \times 10^{9}\,\text{rad} \cdot \text{m}^{-1}$ |
| Dark fibre power coupling factor | $> 10^{-5}$ |
| Power transfer efficiency | $> 4 \times 10^{-9}$ |
| Steering range | $2\,\text{mrad}$ |
| Variance of peak position | $d\vartheta \ll \vartheta_{pw}$ |

**Table 3.1**: Design parameters and constraints from GRACE for optical head design.

## 3.4 Resulting feature tolerances

From the above desired performance aspects, the tolerances of various features of the optical head may be construed. The features considered, and the performance characteristics they affect are listed in table 3.2. Note that in reality there are very few truly independent things, and there will probably be a small amount of coupling between all the architecture features, and all the performance characteristics. However in the limits we are operating in, these inter-dependancies should be small.

In the following analysis we evaluate the constraints that the desired performance places on the architecture features. We assume that the beam from each element is a gaussian mode.

| Architecture feature | Characteristics the feature affects or is constrained by |
|---|---|
| Number of elements | Power transfer efficiency |
| Polarisation uniformity | Contrast, Variance of peak position |
| Glass flatness and phase control | Variance of peak position |
| power uniformity | Contrast, Variance of peak position |
| Magnitude of Fibre Spacing | Steering range, dark fibre power coupling |
| Emitter mode width | Uncommon dark fibre phase error, dark fibre power coupling, steering range |
| Precision of Fibre Spacing | Uncommon dark fibre phase error |
| Glass thickness | Uncommon dark fibre phase error, dark fibre power coupling |
| Beam pointing angle error | Uncommon dark fibre phase error, dark fibre power coupling, far field effects |

**Table 3.2**: Optical head feature dependancies.

## 3.5  Emitter mode width

It is required that the power at the receiving aperture never falls below 90% of the peak power. For an array with sufficiently small elements, pointing error much smaller than the beam divergence, and with sufficiently small separation, the width of the beam from a single element limits the output of the array. We assume that the receiving aperture is small compared to the far field beam width, and neglect effects of the phased array itself. We thus may consider the radius at some distance $z$ at which the intensity drops to 10% of the peak intensity for the gaussian mode from a single element to be the limit of the steering range.

The intensity at radius $\rho(z)$ of a gaussian mode with power $P$, radius $r(z)$ a distance $z$ from the waist is given by [18]:

$$I = \frac{2P}{\pi r(z)^2} \exp\left(-\frac{2\rho(z)^2}{r(z)^2}\right) \tag{3.11}$$

The radius at which this is 90% of the peak intensity is thus:

$$0.9 = \frac{I}{\frac{2P}{\pi r(z)^2}} = \exp\left(-\frac{2\rho(z)^2}{r(z)^2}\right) \rightarrow \rho(z) = r(z)\sqrt{-\frac{1}{2}\ln(0.9)} \approx 0.229 r(z) \tag{3.12}$$

[2]In this case the distance $z$ is the distance from the array to some point in the far field. The radius of a gaussian mode at distance $z$ is:

$$r(z) = r_0\sqrt{1 + \left(\frac{\lambda z}{\pi r_0^2}\right)^2} \tag{3.13}$$

---

[2]Note that in this case, and others in this section we have rounded down so as to provide a conservative estimate for the radius.

For large $z$ this simplifies to:

$$r(z) \approx \frac{\lambda}{\pi r_0} z \qquad (3.14)$$

Which implies that:

$$\rho(z) \approx 0.229 \frac{\lambda}{\pi r_0} z \qquad (3.15)$$

This is saying that in the far field the maximum angle over which we may steer before the intensity of a single element drops below 90% of the peak is:

$$\vartheta_r \equiv 0.229 \frac{2\lambda}{\pi r_0} \qquad (3.16)$$

Note that the actual range might be larger due to the effects of the array itself which we have neglected in this analysis. Since we require a steerable range of $\vartheta_r > 2\,\mathrm{mrad}$ this gives the required waist radius as:

$$\vartheta_r > 2 \times 10^{-3} \to 0.229 \frac{2\lambda}{\pi r_0} > 2 \times 10^{-3} \to r_0 < 77\,\mu\mathrm{m} \qquad (3.17)$$

Due to constraints from the power required at the other satellite, this was taken to be a nominal $70\,\mu\mathrm{m}$.

Note that single mode polarisation maintaining fibre must be used in this device, and the mode exiting such a fibre has a typical radius of $3.3\,\mu\mathrm{m}$. To achieve the mode radius required for the desired far field performance some form of lens-let array would need to be placed in the optical path.

## 3.6    Number of elements

From equation 3.5 we know that the power transfer efficiency is given by:

$$\eta \equiv N^2 \epsilon^2 \qquad (3.18)$$

where $\epsilon$ is the efficiency of electric field transferred onto the array aperture from a single element. For a transmitting element of width $70\,\mu\mathrm{m}$, and a circular receiving aperture with a $1\,\mathrm{mm}$ radius. We may calculate the power transfer efficiency using the model detailed inA. We calculate the overlap integral from a gaussian mode of waist radius $1\,\mathrm{mm}$ over the receiving aperture, with the apertures separated by the distance of $220\,\mathrm{km}$ between the two satellites. This gives:

$$\epsilon^2 = 3.53 \times 10^{-12} \qquad (3.19)$$

Thus to meet our requirement of a transfer efficiency of $\eta > 4 \times 10^{-9}$ we need at least:

$$N > \left(\frac{4 \times 10^{-9}}{3.53 \times 10^{-12}}\right)^{\frac{1}{2}} \approx 33 \qquad (3.20)$$

Note that without a phased array receiver, $N > 1133$. To investigate this case, N was chosen to be $N = 1512$.

## 3.7   Glass thickness

Once again the model detailed in appendix A was used to calculate the magnitude and phase of the fraction of power coupled from light traveling out from one fibre, reflecting off a reference surface, and into a neighbouring fibre (the *coupling factor*). From this model, the fraction of power coupled into the dark fibre could be calculated with various parameters. Figure 3.7 shows the magnitude of the coupling factor with glass thickness and separation for fibres with waist radius $70\,\mu$m. The polarisation-maintaining, single-mode fibre ordered for this prototype had a $125\,\mu$m cladding diameter, which provides a lower bound on how close the fibres can be. The lower bound of the z axis is the lowest coupling factor we may tolerate ($10^{-5}$). The plot shows that the spacing between the fibres dominates the magnitude of the coupling factor, almost independent of glass thickness, however thicker glass relaxes the spacing requirement roughly quadratically. A nominal glass thickness of 10 mm was selected.
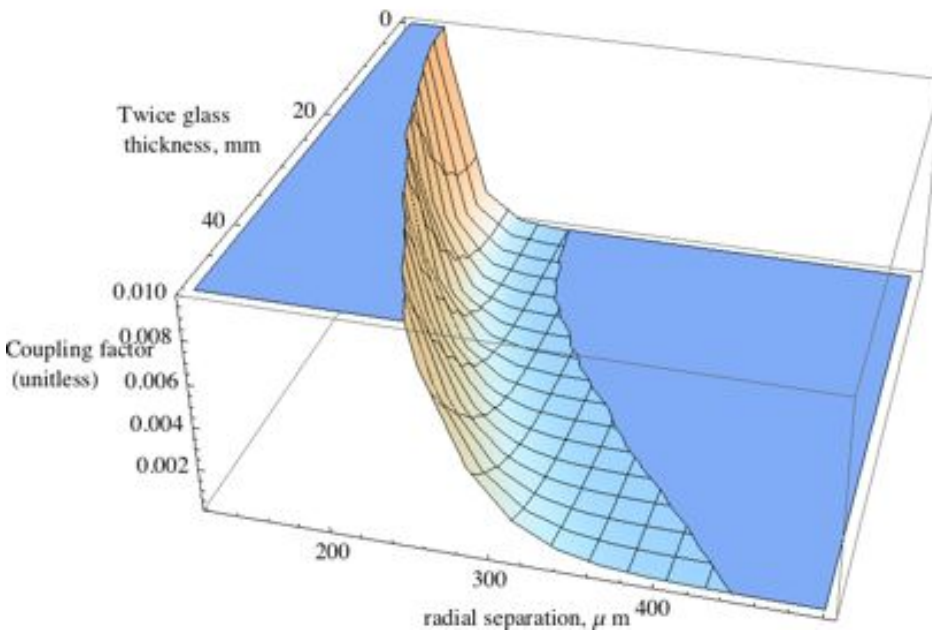


**Figure 3.7:** The coupling factor for mode radii of $70\,\mu$m, plotted against radial separation from $125\,\mu$m to $500\,\mu$m and glass thickness from 0 to 5 cm.

## 3.8   Magnitude of Fibre spacing

### 3.8.1   Constraints from Dark fibre power coupling

From the model detailed in A, the magnitude of the coupling factor was determined with spacing, with the selected glass thickness of 10 mm, and fibre widths of $70\,\mu$m. The magnitude of the coupling factor with radial separation was plotted, and the result is shown in figure 3.8. Since the coupling factor was constrained to be $10^{-5}$, which is the lower limit of this plot, we see that this constrains the spacing to be $s < 195\,\mu$m. For future calculations a value of $150\,\mu$m was selected.

Note the speed with which the coupling factor decreases with separation. This places

a strong restriction on the spacing precision. For our chosen separation of $150\,\mu$m this tolerance is about $\pm 45\,\mu$m, since the worst case scenario with an error greater than this could result in a separation greater than $195\,\mu$m.
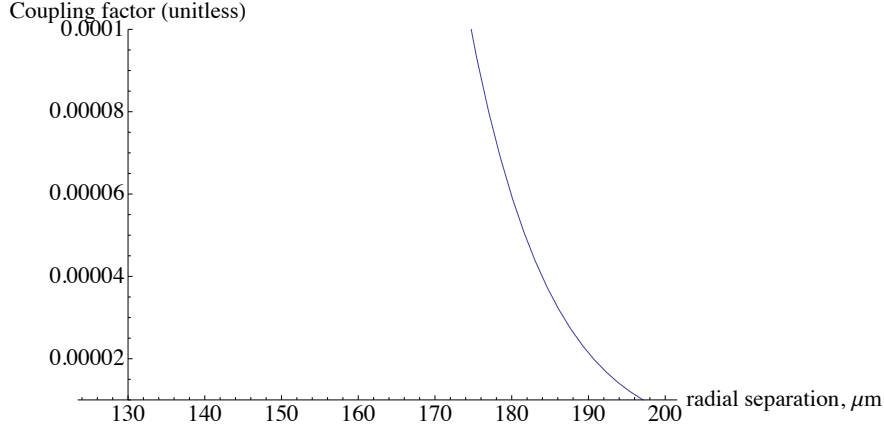


**Figure 3.8:** Magnitude of the coupling factor for emitter mode radii of $70\,\mu$m, and a glass thickness of $10\,$mm.

Recall that the array is two dimensional, and there exist many geometries in which the fibres could be spaced. Because steering range improves with tighter spacing, it is desirable to have the fibres as closely packed as possible. The optimal packing for circular disks in a two dimensional lattice is obtained with a hexagonal lattice[23], so this was selected. This also makes for a very scalable design, as the lattice may be broken up into smaller tessellating pieces that are simpler to manufacture. One such pattern is shown in figure 3.9, where the smaller piece is made up of two bright fibres and a dark fibre.
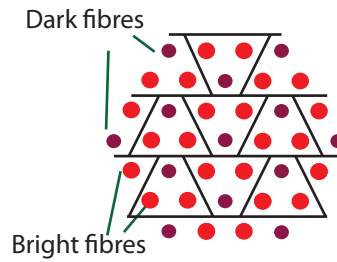


**Figure 3.9**: Nominal 2D array geometry for fibre array.

### 3.8.2   Constraints from dynamic uncommon dark fibre phase error

We have the constraint that the derivative of the phase of the coupling factor with respect to distance should be less than $20 \times 10^9\,$rad$\cdot$m. The model in A was used to plot this with fibre spacing. The resulting plot is shown in figure 3.10. This indicates that for the small fibre spacing we are considering, this constraint is not relevant.
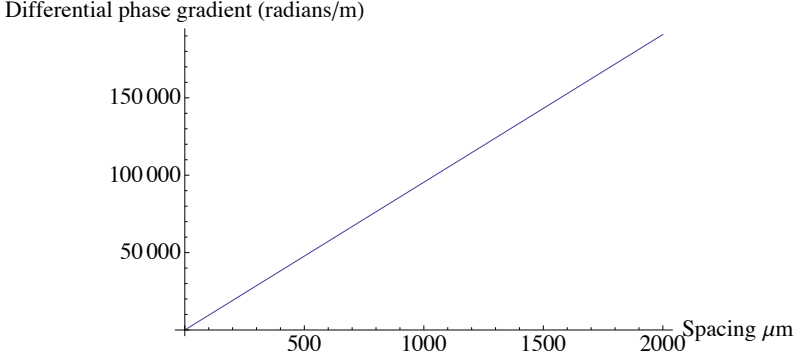
**Figure 3.10:** Derivative of the phase of the coupling factor with radial separation of the fibres, with fibre diametres of $70\,\mu$m, and glass thickness of $10\,$mm.

## 3.9 Precision of Fibre spacing

### 3.9.1 Constraints from static uncommon dark fibre phase errors

The situation sketched in figure 3.5 was simulated using the model detailed in A. The phase of the coupling factor for two bright fibres coupling into a dark fibre was calculated. Each bright fibre was assumed to be positioned with some tolerance with respect to the dark fibre. With a given tolerance the maximum offset that can be obtained between the fibres is twice the tolerance. This maximum difference in phase was then plotted with position tolerance as shown in figure3.11. This shows the differential phase of the coupling factor versus position tolerance for glass thickness of $10\,$mm and emitter mode radii of $70\,\mu$m shown in blue. Also shown in purple is the constraint of $\frac{\pi}{2}$. We see that the static offset is more than $\frac{\pi}{2}$ when the position tolerance exceeds about $50\,\mu$m, thus we should not need to calibrate for static phase error if our position tolerance is less than $50\,\mu$m. The tolerance imposed by the dark fibre power coupling is stronger than this.
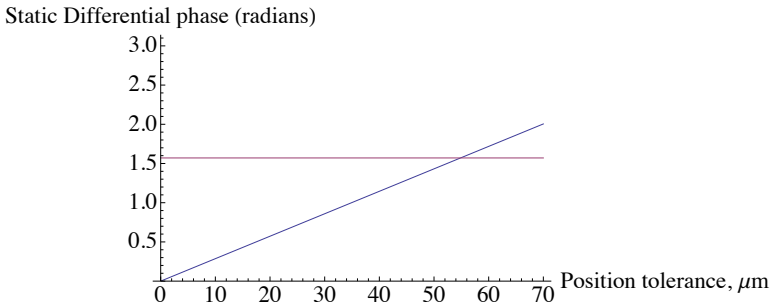


**Figure 3.11:** Differential phase of the coupling factor versus position tolerance for glass thickness of $10\,$mm and emitter mode radii of $70\,\mu$m shown in blue. Also shown in purple is the constraint of $\frac{\pi}{2}$. We want the blue line to be below the purple.

### 3.9.2 Constraints from power on target

As the power on the target is dependent on the phase, it is also dependent on the geometry. Thus there exists an upper bound on the fibre position errors from this dependancy. This was evaluated in the final evaluation simulation.

## 3.10 Beam pointing angle error

The bright fibres will be misaligned. It is of interest to know how much they can be misaligned before the error becomes detrimental to the array's performance.

The model used above was extended to include pointing angle error, as detailed in appendix B. For the parameters chosen above, the various restrictions on this error were evaluated using this model. We find a final tolerance of $\alpha < 0.5°$. Note that both of the dark fibre phase error and dark fibre power coupling are affected by tolerances in pointing angle, and spacing. The analysis performed here naively assumes infinite precision of one parameter while evaluating the other, thus in the actual construction, when both errors are present, more conservative restrictions should be made.

### 3.10.1 Restrictions from static uncommon dark fibre phase error
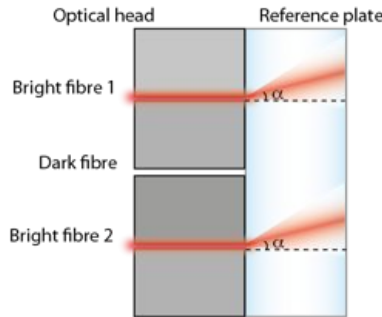


**Figure 3.12:** The situation modeled to determine the restrictions on the pointing angle from the uncommon dark fibre phase error. It was assumed that the above scenario would lead to the worst-case differences in phase at the dark fibre for a given pointing angle error $\alpha$.

Static uncommon dark fibre phase error could also be caused from different pointing directions of the two bright fibres with respect to the dark fibre. The situation sketched in figure 3.12, was assumed to lead to the worst-case differences in phase at the dark fibre for a given pointing angle error $\alpha$, as the resulting path length difference is maximised in this scenario. A plot of the uncommon phase error with pointing error from the model of this situation is shown in figure3.13. It indicates that the uncommon phase first becomes greater than our limit of $\frac{\pi}{2}$ at a pointing angle error of 2.5 mrad. It is unlikely that a manufacturing procedure will be able to align the fibres in the head to this level of precision. It is not critical, however, since the error is static and may be calibrated for later. This means there will almost definitely be some calibration required.

Uncommon phase difference, rad
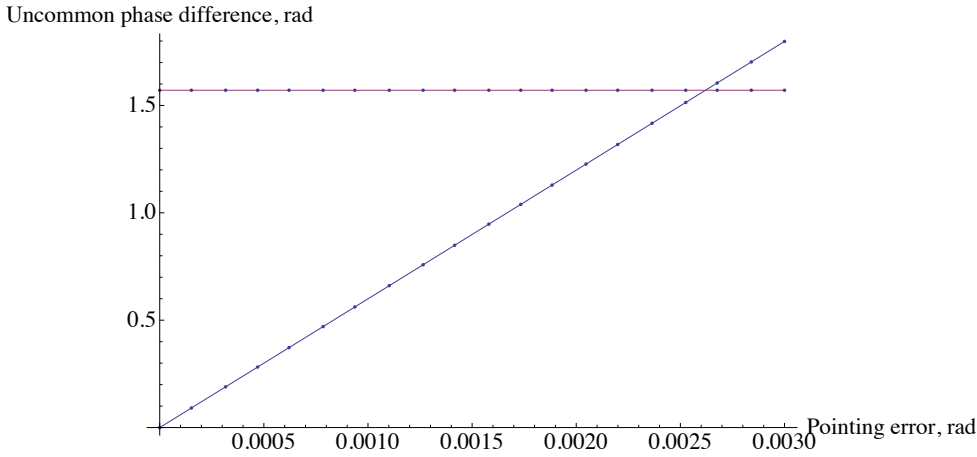


**Figure 3.13:** Worst case uncommon phase difference with pointing error for spacing of $150\,\mu$m, glass thickness of $10\,$mm and emitter mode radii of $70\,\mu$m. Note that the phase wraps because it is modulo $2\pi$.

### 3.10.2 Restrictions from dark fibre power coupling

The power coupled into the dark fibre was also evaluated for various worst-case pointing angles. A plot of the lowest power coupled into the dark fibre for a given pointing error is shown in figure 3.14. Again, setting the lower limit of the plot to be $10^{-5}$, the worst tolerable coupling factor, we see that this constrains the pointing error to be $\alpha < 8.5\,$mrad, or $\alpha < 0.5°$. This is a very tight constraint. Companies that will possibly manufacture the array have stated they could not maintain a tolerance of better than $1°$. Thus this suggests itself as a possible future concern for the array manufacture. The coupling factor appears to increase with glass thickness, so increasing the thickness of the glass might resolve this issue. Another alternative could be to coat the glass in some way.

Magnitude of coupling factor, unitless
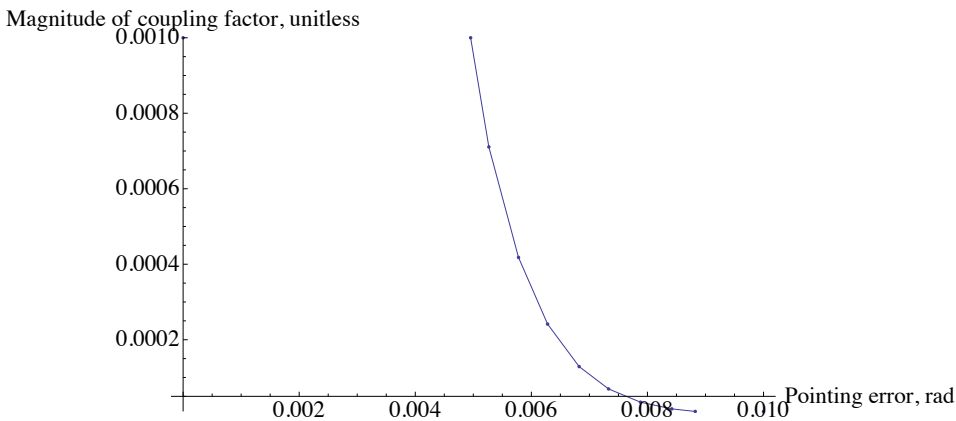


**Figure 3.14:** Worst case Dark fibre power coupling with pointing error for spacing of $150\,\mu$m, glass thickness of $10\,$mm and emitter mode radii of $70\,\mu$m. Not shown is the peak of this plot, at $0\,$rad which gives an ideal coupling factor of $3\,\%$.

### 3.10.3 Restrictions from far field effects

If the pointing error is a significant fraction of the beam divergence, it may have significant effect on the far field pattern. For our case we have a waist radius of $70\,\mu$m. This

corresponds to a beam divergence of:

$$\vartheta_d = \frac{2 * 1.064}{\pi * 70} = 9.6 \, \text{mrad} \tag{3.21}$$

Which is of the same order as the pointing error constraint from power coupling above ($\alpha < 8.5 \, \text{mrad}$). This physically makes sense, but also indicates that this could be a problem in the future. This was not analysed and should be investigated further.

## 3.11   Glass flatness and phase control

The control of the relative phase of each emitter will affect the control of the far field beam pattern in the same way that the quality of a telescope mirror effect the far field beam profile. As we are primarily concerned with the power at a single point for this application, the phase control is thus only limited by the characteristics of the interference maxima on the target. Specifically, errors in phase control are assumed only to couple into the position of the peak, and thus provide some variance in the peak power on the target.

For the power to vary little over the target, we require that the variations in position from phase jitter are far less than the peak width. From equation 3.8, this means changes in steering angle, $d\vartheta$ are constrained as follows:

$$d\vartheta \ll \frac{2\lambda}{(N-1)s} \tag{3.22}$$

From equation 2.9 we know that variations in the phase depend couple into variations in steering angle according to:

$$|d\phi| = \frac{s}{\lambda}d\vartheta \rightarrow d\vartheta = \frac{\lambda}{s}d\phi \tag{3.23}$$

thus:

$$\frac{\lambda}{s}d\phi \ll \frac{2\lambda}{(N-1)s} \rightarrow d\phi \ll \frac{2}{(N-1)} \tag{3.24}$$

For our $40 \times 40$ element array this implies:

$$d\phi \ll 5 \times 10^{-2} \tag{3.25}$$

a phase error of $10^{-3}$ cycles fits this restraint.

## 3.12   Power and Polarisation uniformity

It is desirable to have each element of the phased array radiate the same amount of optical power. To see this consider the case where two elements are interfering at a point, radiating intensities $I_1$ and $I_2$. We know from 2.4 that:

$$I = I_1 + I_2 + 2\sqrt{I_1 I_2} \cos(\phi_1 - \phi_2) \tag{3.26}$$

Where $\phi_1$ and $\phi_2$ are the phases of the two beams. From this equation it can be seen that if the two intensities are equal, the minimum value is 0, and the maximum value is $4I$, however if they are unequal, then the contrast is reduced. Further, the position of peak intensity will be shifted slightly.

The polarisation uniformity similarly couples into the contrast and peak position. If

we have two electric fields with linear polarisation angles $\vec{\psi}_1 + \delta\vec{\phi}_1$ and $\vec{\psi}_1 + \delta\vec{\phi}_2$ then only the component with the same polarisation will interfere in the way we want. The other polarisation's couple into power that is beyond our control, lowering the contrast. For a polarisation error $\delta\phi$, the fraction of intensity adding to the minimum intensity is the projection onto the polarisation axis perpendicular to the desired polarisation direction. That is, for a beam of intensity $I$:

$$I_{bad} = I \sin(\delta\phi) \tag{3.27}$$

These parameters were simulated numerically. The polarisation angle was assumed to be a normally distributed random variable with a standard deviation of one degree, and the power was assumed to vary between emitters also according to a normally distributed random variable with a standard deviation of 5%. The result of these noise terms contributed to error bars on modeled estimates of the other performance characteristics.

## 3.13   Final design evaluation

The summarised tolerances and design parameters are shown in table 3.3.

| Architecture feature | Tolerance or value |
| :---: | :---: |
| Beam pointing angle error | $\alpha < 85\,\mathrm{mrad}$ |
| Magnitude of Fibre Spacing | $s = 150\,\mu\mathrm{m},\ s < 195\,\mu\mathrm{m}$ |
| Precision of Fibre Spacing | $ds < 45\,\mu\mathrm{m}$ |
| Mode radius | $70\,\mu\mathrm{m}$ |
| Glass flatness and phase control | $d\phi < 10^{-3}\,\mathrm{cycles}$ |
| power uniformity | $dP < 5\%$ |
| Polarisation uniformity | $dp < 1°$ |
| Glass thickness | $d = 10\,\mathrm{mm}$ |
| Number of elements | $N > 33$ with phased array receiver. $N > 1133$ without. |

**Table 3.3**: Point design tolerances for optical head parameters.

The design was evaluated more concretely in a full two dimensional model. In order to do this, a model was developed that generated the output for the geometry in the far field by summing gaussian modes with waist positions in a hexagonal pattern shown in figure 3.15. To attain 1512 bright fibres, an array of 27 rings was simulated.
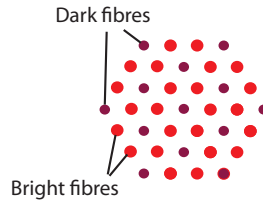


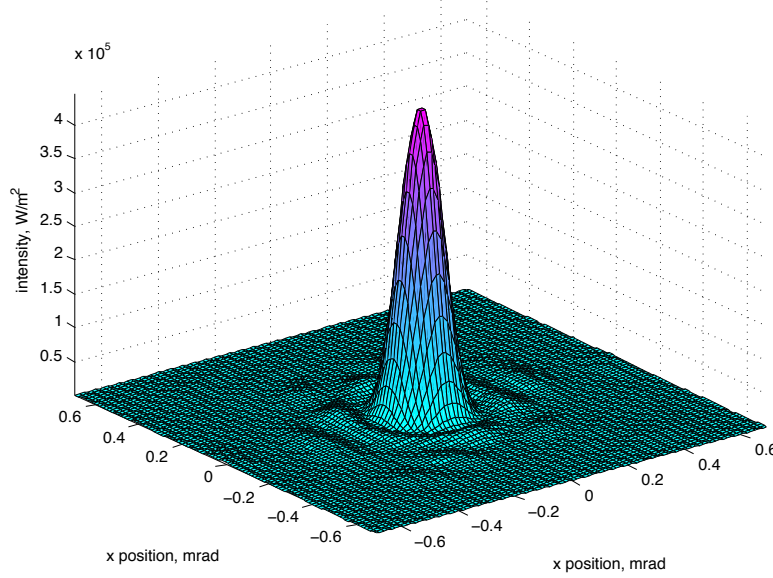**Figure 3.15**: A hexagonal array with 3 rings.

**Figure 3.16:** Sample output of the interference pattern about the desired steering point for the point design indicated.

The geometry was simulated in C with normally distributed random noise added to the power, polarisation and fibre positioning with standard deviations given according to the values in table 3.3. A sample output of the array is shown in figure 3.16. There are no other Bragg peaks visible because for the tolerances specified, the distance between the peaks is larger than the divergence of a single element. Therefore these other peaks are suppressed.

The power coupled into a 1 mm radius aperture at 220 km with no receiving array was calculated with this model. The total power input to the array was 1 W, so this gives a measure of the transfer efficiency of the array. The variance in the peak position was also calculated. The results are shown in table 3.4. The power in the aperture does not meet specification, but this could be easily fixed by adding a phased array at the receiver.

Thus we see that it is possible to construct an array with parameters such that the dark fibre solution functions appropriately, although some constraints, notably the pointing error tolerance, are quite harsh. With this direction theoretically justified, the remainder of this thesis will be concerned with an experimental test of the dark fibre solution, and testing of the more scalable CDMA codes.

| Output characteristic | Constraint | Expected performance |
|---|---|---|
| Uncommon dark fibre phase error | Static error:$< \frac{\pi}{2}$, Dynamic error: $< 20 \times 10^{9}$ rad/m | Static error: $\gg \frac{\pi}{2}$ (from pointing error). Dynamic error: $10^{5}$ rad/m |
| Dark fibre power coupling factor | $> 10^{-5}$ | 3% (ideal case, no pointing error) |
| Power transfer efficiency | $> 4 \times 10^{-9}$ | $0.62 \pm 0.01 \times 10^{-9}$ |
| Standard deviation of peak position | $d\vartheta \ll \vartheta_{pw}$ | $1\,\mu$rad |

**Table 3.4:** Design parameters and constraints from GRACE together with the expected performance from simulations for the point design.

# Controller Design

The *controller* is an algorithm implemented on the FPGA that calculates how the phase modulators (EOM's) actuate based on the sensor signal. It is a crucial part of the phased array because the phase of the light at the reference surface will be affected by noise from a number of sources, such as thermal noise and laser frequency noise. The controller is responsible for this suppression of deviations from the desired relative phase between bright fibre elements. Also coupled with the controller on the FPGA is the algorithm for the dark fibre correction. In the previous design of the optical phased array only the direct back reflected signals from the bright fibres was taken as a measurement of the phase. This results in the problem of the $\pi$ ambiguity, an ambiguity that can cause the phasemeters to initialise to values that are incorrect. This renders the array output unpredictable. The dark fibre resolves this issue by giving a measure of the real phase at the reference surface, which allows us to measure and correct for the phasemeter initialisation error.

In this chapter we discuss the controller design, and describe how it is implemented on the FPGA. We then detail its performance in the optical experiment described in chapter 6, demonstrating successful noise suppression at low frequencies and lock the phase to a standard deviation of $12\,\mu$cycles, improving on the previous design by a factor of more than 100. We also describe the implementation of the dark fibre correction, and detail its successful use to solve the $\pi$ ambiguity for two fibres.

## 4.1 Controller design

### 4.1.1 Controller requirements

The controller's primary task is to control the output of a system. In our case this means fixing the relative phase to some arbitrary set point. To do this the controller must remove noise in the relative phase signals. The controller accomplishes this by first sensing the deviation from the desired response; the *error signal*, then modifying it in some way, and subtracting the modified *control signal* from the input. A sketch of a standard *control loop* is shown in figure 4.1. It consists of some process that has some frequency-dependent output, $Y(\omega)$ where $\omega$ is the angular frequency. A sensor that senses the difference between the output and the desired output, and feeds this to the controller, which modifies the error signal in some way. The output of the controller is transferred to the actuator, which adds it back into the system, hopefully correcting the error and bringing the output closer to the desired output.

One of the most common methods of designing a controller is the frequency response design technique. In this technique, the desired overall response of the controller is first decided upon, chosen based on the frequencies over which the noise should be suppressed.

Then the frequency response of the other elements is analysed, and the controller designed to compensate for these other elements such that the overall frequency response is what is desired. However, the design must also be such that the whole control loop is stable.
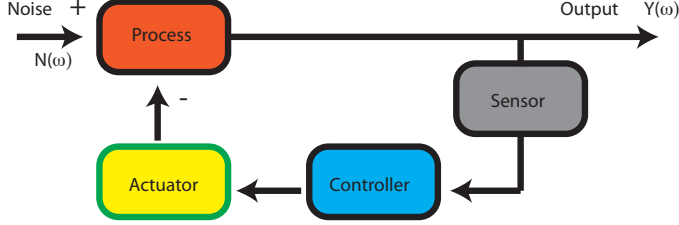


**Figure 4.1:** A typical control loop with complex-valued input noise signal $N(\omega)$ and output signal $Y(\omega)$.

To see how a control loop can become unstable we consider the performance of the loop in figure 4.1. We begin by assuming that the system is linear and in a steady state. The performance of the controller can be characterised by how well it suppresses the noise $N(\omega)$ incident on the system. This can be quantified by the *closed loop* transfer function, or the ratio of the output to the input:

$$T(\omega) = \frac{Y(\omega)}{N(\omega)} \tag{4.1}$$

If the transfer function is small over some frequency range, then the noise will be strongly suppressed in that range. Now consider the transfer function of the typical control loop shown in figure 4.1. If we suppose that each of the components has some transfer function, suppose $S(\omega)$ for the sensor, $C(\omega)$ for the controller, and $A(\omega)$ for the actuator, then the output of the loop will be given by:

$$Y(\omega) = N(\omega) - A(\omega)C(\omega)S(\omega)Y(\omega) \tag{4.2}$$

Which implies that the transfer function of the loop will be:

$$T(\omega) = \frac{Y(\omega)}{N(\omega)} = \frac{1}{1 + A(\omega)C(\omega)S(\omega)} = \frac{1}{1 + L(\omega)} \tag{4.3}$$

Where $L(\omega) = A(\omega)C(\omega)S(\omega)$ is the *open loop* transfer function, or open loop gain. Now consider the regime in which the transfer function suppresses the noise, as we desire. Recall that the transfer function is complex valued, that is, it has some phase as well as magnitude, the regime in which the transfer function suppresses noise is where:

$$\left|\frac{1}{1 + L(\omega)}\right| < 1 \rightarrow |1 + L(\omega)| > 1 \tag{4.4}$$

In other words, the noise is only suppressed if the complex value of the open loop gain $L(\omega)$ remains outside of the unit circle about $-1$ on an Argand diagram, as shown in figure 4.2. Also depicted in the figure is a typical open loop gain of some control system.

Unfortunately the gain will inevitably decrease to zero eventually, because of delays and inherent speed limitations of the system.
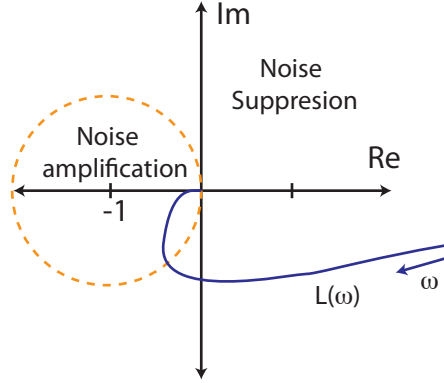


**Figure 4.2:** Parametric plot of the complex value of the open loop gain as a function of frequency, $L(\omega)$, and the regions where noise is suppressed.

For the purpose of this thesis, two criterion were used to evaluate the stability of a particular controller. These were the *phase margin, gain margin.* Also useful is the *unity gain frequency.* They are defined as follows [24]:

**Unity gain frequency**  The frequency at which the magnitude of the gain is unity.

**Gain Margin**  The gain in dB of the controller where the phase becomes $-180°$. For a typical stable system this is larger than $3\,\mathrm{dB}$. This is equivalent to the theoretical factor by which the gain can be raised before instability results.

**Phase margin**  The difference of the phase from $-180°$ at the unity gain frequency. That is $PM = \phi_{unity} + 180°$. To ensure stability we need the phase margin to be positive, experience shows $> 30°$ is the usual physical requirement for stability.

Hence to select an overall transfer function one first considers the noise in the system that is to be suppressed. The transfer function is then designed such that it is small at these frequencies. To ensure stability one then analyses the open loop gain of the proposed controller and makes use of the following theorem due to Bode[24]:

**Bode's Theorem**  For any stable system the phase of the open loop gain is uniquely related to its magnitude. That is $\arg(L(\omega)) = f(|L(\omega)|)$ for some function $f$.

If the slope of $|L(\omega)|$ versus frequency remains constant for roughly a decade of frequency, and is plotted on a log-log scale the relationship is given by:

$$\arg(L(\omega)) \approx 90°n \tag{4.5}$$

Where $n$ is the slope of $|L(\omega)|$ on the log-log scale when plotted with frequency. Since we want the phase margin to be $PM > -180°$, we require the slope of the phase of the open loop gain to be

$$n > -2 \tag{4.6}$$

Experimentally this requirement is usually restricted to $n = -1$ at the unity gain frequency. Note that the slope will generally be negative because of limits of the speed of the system.

Thus we design the controller such that the magnitude of the open loop gain has a slope of $-1$ for about a decade around the unity gain frequency when plotted on a log-log scale. For more information on the theory and operation of control systems refer to [24].

### 4.1.2 Useful components

Like electronics, there are a few useful "components" that are often utilised in control systems. The few of particular relevance are listed here. The first is the integrator, the data flow diagram of which is shown in figure 4.3. The integrator, as the name suggests, integrates the input signal $x(t)$ over time.

There are three operations in the digital non-floating point integrators used here; an adder, a shift register, and a gain. The gain stage multiplies the signal by some constant, while the shift register stores the value of the previous clock tick. To characterise the integrator, we find the transfer function. If we first suppose that the input signal at discrete time $n$ is $x(n)$ then the output for either integrator shown, in the time domain, is given by:

$$y(n) \quad = \quad G * (x(n) + y(n-1))$$

Now consider the case in the frequency domain:

$$Y(\omega) = G * (X(\omega) + Y(\omega)e^{-i\omega\tau}) \tag{4.7}$$

Where we have assumed that there is a delay of time $\tau$ associated with the shift register, which implies the phase delay $e^{-i\omega\tau}$.[1] This implies that the transfer function is:

$$\frac{Y(\omega)}{X(\omega)} \quad = \quad \frac{G}{1 - e^{-i\omega\tau}}$$

$$= \quad \frac{Ge^{\frac{i\omega\tau}{2}}}{e^{\frac{i\omega\tau}{2}} - e^{-\frac{i\omega\tau}{2}}}$$

$$= \quad \frac{Ge^{\frac{i\omega\tau}{2}}}{2i\sin(\frac{\omega\tau}{2})}$$

Now assume that our system is sufficiently fast that the condition $\omega\tau \ll 1$ holds. Then we have:

$$\frac{Y(\omega)}{X(\omega)} \quad \approx \quad \frac{G}{i\omega\tau} = e^{-i\frac{\pi}{2}}\frac{G}{\omega\tau}$$

So we see that an integrator has a transfer function proportional to $\frac{1}{\omega}$, and adds a phase delay of $\frac{\pi}{2}$.

However there is some subtlety to the actual implementation of an integrator in an FPGA. As the numbers processed in the integrator are integers with some finite bit length, this means there is a bound to the output of the integrator. It also happens that from the nature of the representation of integers in the FPGA, once we exceed this bound, the number will wrap from the upper to the lower bound and vice-versa. Suppose, for example, the integrator used signed 32 bit integers (denoted $I32$). These can represent numbers from $-2^{31}$ to $2^{31} - 1$. If an integrator has integrated a signal such that the value

---

[1] This is analogous to the shift theorem for regular fourier transforms.

in the shift register is at its bound of $2^{31} - 1$, and the signal is some positive number, say 1, then on the next clock tick, the output of the integrator will be:

$$(2^{31} - 1)_{I32} + 1_{I32} = (-2^{31})_{I32} \qquad (4.8)$$

The integrator has "wrapped". These wraps are characterised by jumps in the output of the integrator, and can be detrimental to controller performance.
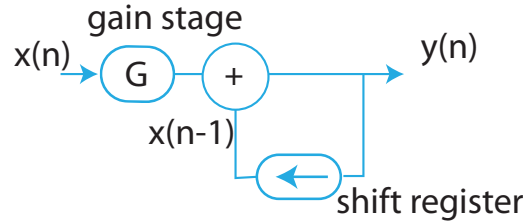


**Figure 4.3**: Figure showing an integrator.

The second important component is that of a proportional stage. It is simply a gain stage, and its transfer function is given by:

$$\frac{Y(\omega)}{X(\omega)} = G \qquad (4.9)$$

This is constant with frequency, with no phase changes.

## 4.2   Controller implementation

Refer again to figure 4.1. In the context of this experiment we wish to design a controller for the relative phase between two bright fibres. The system consists of the laser light traveling from the EOM's to the reference surface. The sensor stage consists of a number of phase-locked loops, together with a modulation-demodulation scheme that will be addressed in chapter 5. The actuator stage is made up of the EOM's and the associated driving electronics, and the controller stage is comprised of the controller program running on the FPGA. This consisted of two of the controllers described below; controlling the relative phase between all three of the bright fibres.

In designing this controller it was considered that the noise in the system is primarily driven by ambient acoustic and temperature fluctuations. These are low frequency ($\sim 1\,\mathrm{KHz}$). For this reason we want a controller with plenty of gain at these frequencies. Such a controller may be achieved by staggering two integrators. The final controller is shown in figure 4.4. It takes two inputs procured from the sensor stage. These inputs are error signals derived from measurement of the relative phase between two bright fibres from the bright fibre back reflections and from the dark fibre. The *input wrapper* ensured that this signal was modulo one cycle. This is important because it is only desired that the controller lock to the nearest multiple of a cycle. If the input to the controller were not modulo one cycle, then the controller would attempt to feed back over a range larger than

the range of the EOM. An offset was also added to the error signal so that the relative phase could be set to arbitrary values. This would result in the controller feeding back to drive the relative phase to the negative of the offset.

The signal from the bright fibre back reflection was used for the controller error signal, while that from the dark fibre was used to correct possible bright fibre calibration errors[2].

From the integrators, the output was fed through another overall gain stage. This was necessary to calibrate the output values of the controller to those of the Digital to analogue converter used to drive the EOM's (see figure 6.6).
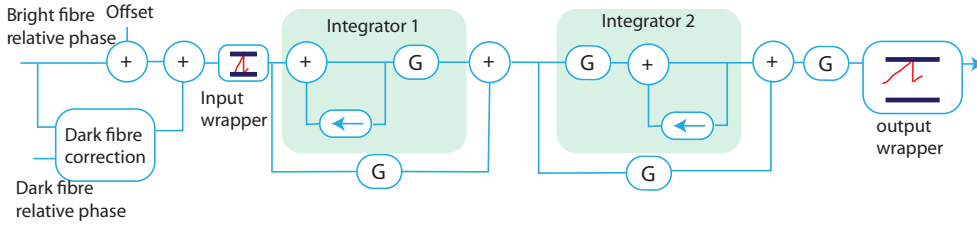


**Figure 4.4:**   Diagram illustrating the final controller used to control the relative phase of two channels.

After the gain the output passes through a "wrapper" to the EOM on one of the fibres, with the other kept as a fiducial. The wrapper was included because the range of the EOM was only about 2 cycles, which meant that if the relative noise drifted beyond this range, the controller could not cancel this drifting because the actuator would saturate.The wrapper was designed such that if the signal at its input was greater than a cycle, it would "wrap" the signal back to zero. Similarly, if the input was less than minus one cycle, it would wrap back up to zero. This wrapping behaviour introduces noise to the system due to the lag of the modulator. However the wrapping was sufficiently fast not to be observed in phase measurements.

This controller was duplicated and used to control the relative phase between modes 1 and 3 and modes 2 and 3 as per the labeling in figure 6.1. For the purpose of further discussion, the controller for the relative phase between modes 1 and 3 was called controller 0, and the controller between modes 2 and 3 was called controller 1.

## 4.3   Dark fibre correction

The dark fibre correction was a chief component of this design and represented a significant novel contribution of this thesis work. It's role was to compare the relative phase signal from the bright and dark fibres, and correct the bright fibre signal if necessary.

The problem of the $\pi$ ambiguity occurs at the initialisation of the bright fibre phasemeters. Suppose, for example, that there is a phase difference of $\pi$ between two fibres. This means that the phase seen at the bright fibre phasemeters will be $2\pi$ because the light travels through the same path twice. When the bright fibre phasemeters initialise they will interpret this as zero leading to an actual relative phase of $\pi$ for a measured phase of

---

[2]Because there are two measurements of the same relative phase, these could be combined by way of some kind of weighted average. However, in the final configuration with the optical head, the signals from the bright fibre back reflections will have a much higher signal to noise ratio than that from the dark fibre measurement. This was not the case in this experiment as the bright fibre signals passed through more beamsplitters than the dark fibre measurements, and thus were attenuated more than the signal from the dark fibre. The controller was developed for the final configuration nonetheless.

0. This is particularly bad because if we desire the beams to constructively interfere at the output we will get destructive interference instead.

If the phasemeters have locked to the correct relative phase, however, then there is no problem. As the phase drifts, the bright fibre phasemeters will measure this, and so long as they do not jump cycles or *cycle slip*, half of the phase they measure will correspond to the phase at the reference surface. Thus we see that the $\pi$ ambiguity is purely a problem of initialisation when the starting phase offset is computed.

The dark fibres resolve this problem by providing a alternate, non-degenerate measurement of the relative optical phase at the reference surface. This means that the initial relative phase can be determined, and corrected for. If we let $\Delta\phi_B$ be the relative phase measured by two bright fibres, and $\Delta\phi_D$ be that measured by the corresponding dark fibre, then the dark fibre looks at $\Delta\phi_B - \Delta\phi_D$. If $\Delta\phi_D - \Delta\phi_B = \pi$ the bright fibre signal needs to be corrected and $\Delta\phi_D - \Delta\phi_B = 0$ means it does not. [3] Although the correction need only be done at start-up, for development it was included live in the code so it could be tested.

To see why the dark fibre correction functions like this consider figure 4.5. This shows the two cases that the dark fibre check had to distinguish for two bright fibres. The first is when one of the phasemeters has been incorrectly initialised. In this case we suppose the phase at the reference surface for bright fibre 1 was initialised to zero at a real phase of $\pi$ and expansion of the fibre has caused this to drift by $\vartheta_1$. Bright fibre 2 has been initialised correctly at 0 and has drifted by $\vartheta_2$. The resulting measurements from the bright fibre signals thus lead to a relative phase of $2(\vartheta_1 - \vartheta_2)$. However the actual relative phase is $\pi + (\vartheta_1 - \vartheta_2)$.

But the dark fibre measures the phase due to propagation through each fibre ($\vartheta_1$ and $\vartheta_2$), plus some common phase due to propagation down the dark fibre. Let these be $\phi_{C1}$ and $\phi_{C2}$ respectively. Thus the relative phase from the dark fibre measurement will be:

$$(\vartheta_1 + \phi_{C1}) - (\vartheta_2 + \phi_{C2}) \approx \vartheta_1 - \vartheta_2 \tag{4.10}$$

Where we have assumed that the differential phase error from differences in the paths of the beams through the dark fibre is negligible (i.e. $\phi_{C1} \approx \phi_{C2}$). This result is independent of the initial calibration of the phasemeters. Thus the relative phase measured by the dark fibre is the actual relative phase at the reference surface, and the difference between the bright and dark fibre relative phase measurements allows us to determine the initialisation errors.

---

[3]Thus we see that the dark fibre measurements need to measure the relative phase to a precision of $\frac{\pi}{2}$, as discussed in chapter 3.
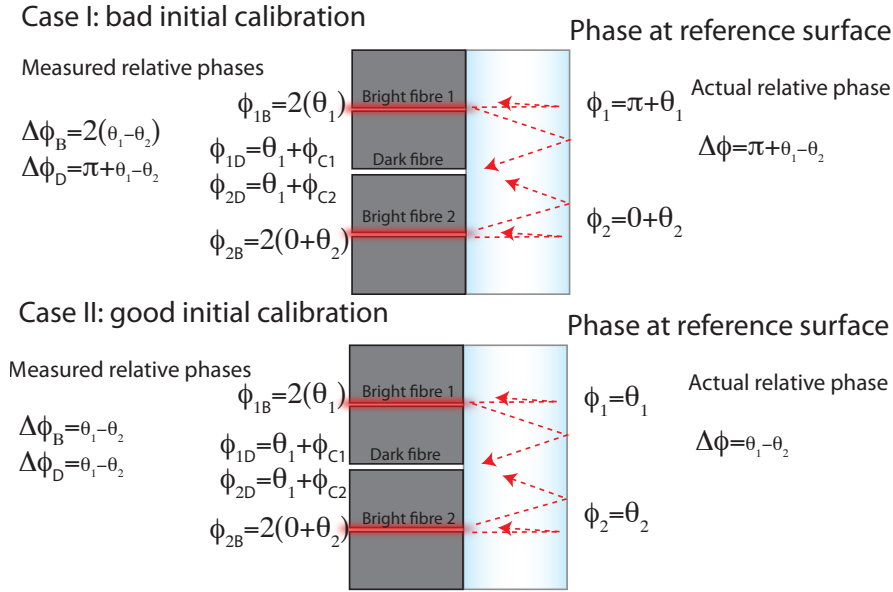
Case I: bad initial calibration

Phase at reference surface

Measured relative phases

Actual relative phase

$\phi_{1B}=2(\theta_1)$  Bright fibre 1

$\Delta\phi_B=2(\theta_1-\theta_2)$

$\phi_{1D}=\theta_1+\phi_{C1}$  Dark fibre

$\Delta\phi_D=\pi+\theta_1-\theta_2$

$\phi_{2D}=\theta_1+\phi_{C2}$

Bright fibre 2

$\phi_{2B}=2(0+\theta_2)$

$\phi_1=\pi+\theta_1$

$\Delta\phi=\pi+\theta_1-\theta_2$

$\phi_2=0+\theta_2$

Case II: good initial calibration

Phase at reference surface

Measured relative phases

Actual relative phase

$\phi_{1B}=2(\theta_1)$  Bright fibre 1

$\Delta\phi_B=\theta_1-\theta_2$

$\phi_{1D}=\theta_1+\phi_{C1}$  Dark fibre

$\Delta\phi_D=\theta_1-\theta_2$

$\phi_{2D}=\theta_1+\phi_{C2}$

$\phi_{2B}=2(0+\theta_2)$  Bright fibre 2

$\phi_1=\theta_1$

$\Delta\phi=\theta_1-\theta_2$

$\phi_2=\theta_2$

**Figure 4.5**: Diagram illustrating the function of the dark fibre correction.

## 4.4   Results

A number of tests of the performance of the controllers are detailed below.

### 4.4.1   Bode plot of controllers

The open loop transfer function of both controllers was measured by feeding a swept-sine signal from the Stanford Research Systems SR785 dynamic signal analyzer into the controller via the analogue inputs provided with the PXI system. The ratio of the input amplitude to the output was then measured automatically for each frequency by the SR785. The results are shown in figure 4.6. The phase margin, gain margin and unity gain frequency of both controllers are detailed in table 4.1. They are similar, but differ slightly probably due to slight differences in the modulator's and driving electronics.
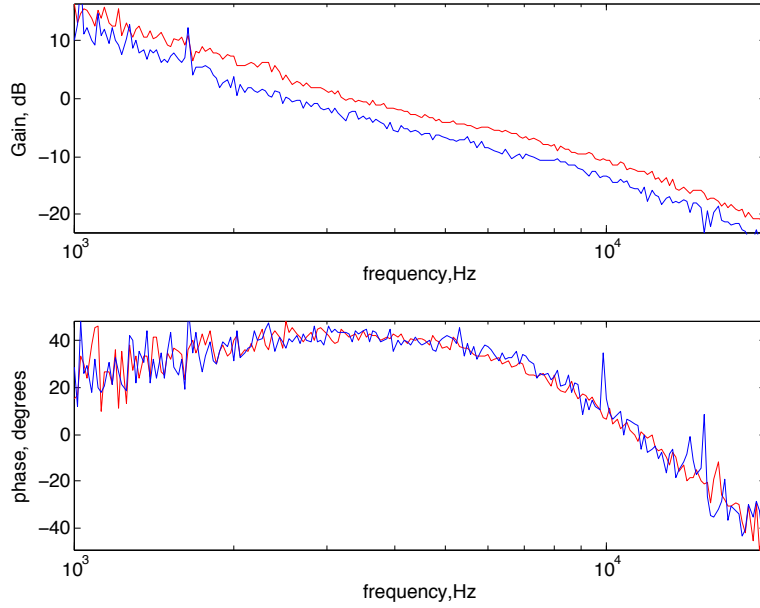
**Figure 4.6:** Plot showing the transfer functions of the two controllers. Controller 0 (relative phase between modes 1 and 3) is blue, controller 1 (relative phase between modes 2 and 3) is red.

| Characteristic | Controller 0 | Controller 1 |
|---|---|---|
| Phase Margin | $\sim 40°$ | $\sim 40°$ |
| Gain Margin | $14\,\text{dB}$ | $12\,\text{dB}$ |
| Unity gain frequency | $\sim 2.5\,\text{kHz}$ | $\sim 3.0\,\text{kHz}$ |

**Table 4.1**: Performance characteristics of the controllers.

### 4.4.2   Phase noise

To determine the effectiveness of the controller at suppressing noise in the system, the relative phase between both modes 1 and 2 and modes 0 and 1 was measured in loop with and without the controller. The resulting power spectral density for controller 1 is shown in figure 4.7. The spectrum of controller 2 was similar. It clearly shows strong suppression at low frequencies as we desire.

Figure 4.8 displays the relative phase signal for controller one when the controller was switched on. As we expect, the controller locks to the nearest cycle. The standard deviation of the relative phase while locked for a period of $6.5\,\text{s}$ was found to be $12\,\mu\text{cycles}$. This is well below the requirement of $10^{-3}$ cycles set out in chapter 3. Since this parameter for the previous design was $\frac{\lambda}{100}$[?] this improves on the previous design by a more than a factor of 800. Additionally, as is shown by the power spectral density below, this RMS noise calculation will be dominated by the audio frequency pickup around $50\,\text{Hz}$.
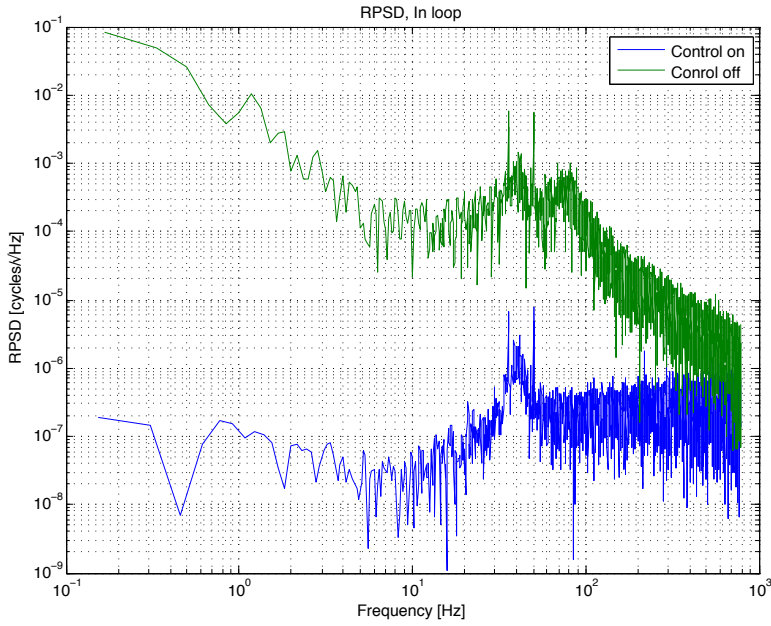
**Figure 4.7:** Plot showing the relative phase noise in the system with (blue) and without (green) controller 1. The spectrum for controller 2 was similar.
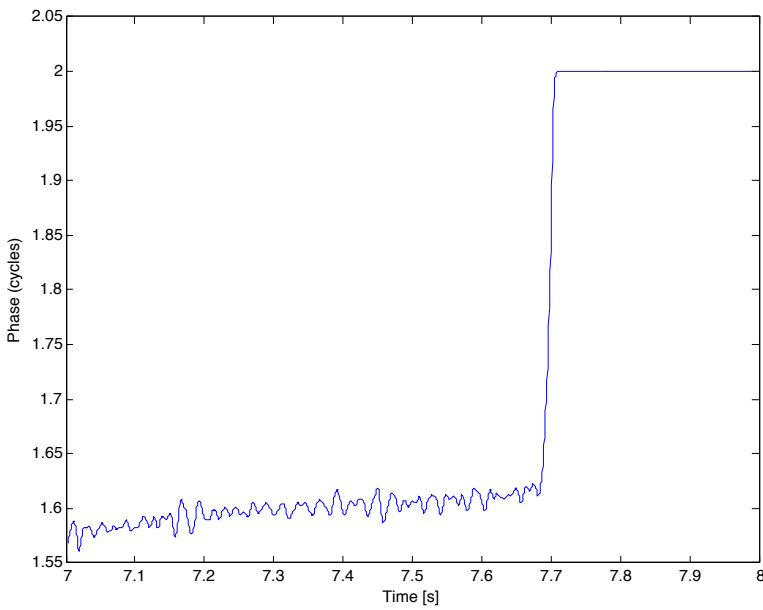


**Figure 4.8:** Plot showing the relative phase when controller 1 was switched on and set to lock to zero. The controller locks to the nearest cycle as expected.

### 4.4.3 Demonstration of dark fibre correction

To test the proficiency of the dark fibre both of the controllers was made to lock the relative phase to a constant with only two beams incident on the reference surface and

the other blocked. The $\pi$ ambiguity meant that the array output always locked to one of two possible states -with the two beams in phase, and with the two beams $\pi$ out of phase. The dark fibre correction was observed to correctly switch between the states as expected. These two states are shown in figure 4.9.

However the difference in the relative phases measured from the dark and bright fibres often changed by half a cycle when this occurred. From the analysis above, this difference should not change, thus this was an unexpected result. It is possible this was a result of one of the phasemeters "cycle slipping" or failing to track the phase of the signal. This could occur because when the dark fibre correction is switched, the desired lock point shifts very rapidly. If the controller feeds back with similar rapidity, this could cause the phasemeter to cycle slip, thus prompting the change in the difference. This could be remedied through further improving the phase meter performance.

The dark fibre was also observed to function with all three beams on the reference surface, but its performance was unreliable. Similar to the case with two beams, with three beams locked to a constant, there are four possible output states (phase measured modulo $2\pi$):

1. All in phase: $\phi_1 = \phi_2 = \phi_3$

2. $\phi_3$ out of phase: $\phi_1 = \phi_2 = \phi_3 + \pi$

3. $\phi_2$ out of phase: $\phi_1 = \phi_2 + \pi = \phi_3$

4. $\phi_1$ out of phase: $\phi_1 + \pi = \phi_2 = \phi_3$

These output states were observed however we could not switch between them reliably.
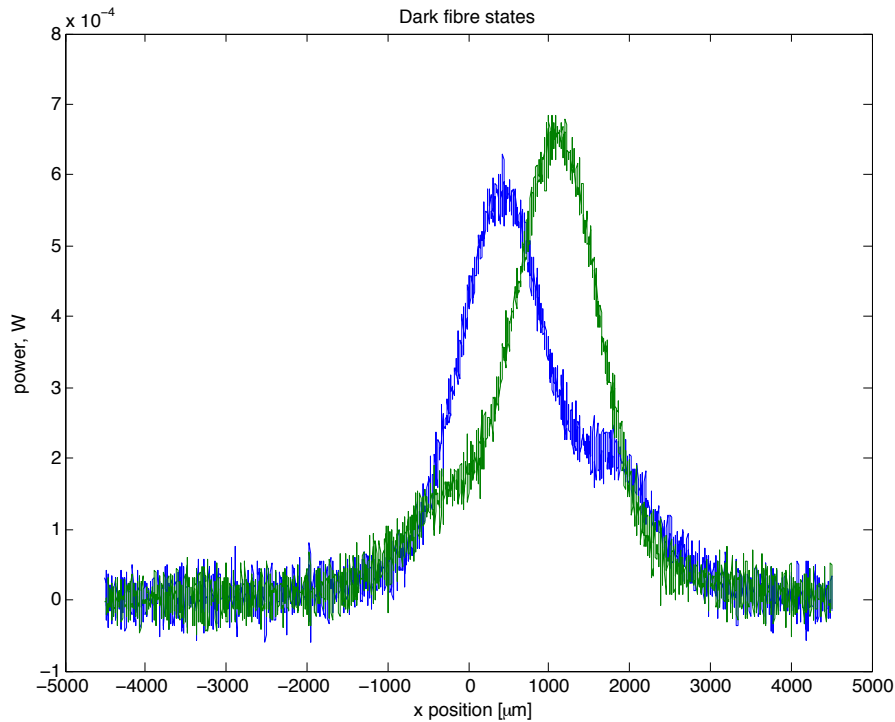


**Figure 4.9:**   The x-axis intensity profiles of the two dark fibre states for two beams observed and switched between.

## 4.5   Problems with the controller

Despite functioning acceptably, the controller exhibited various problems. The first of these would manifest itself in sudden large jumps in the controller output, and also the phase of the dark fibre on the controlled channel. There are two plausible reasons for this. The first could be that an integrator was still wrapping within the controller. This would describe the sudden large jumps, and is plausible because with significant steering the error signal would be more biased toward a particular sign, and not average to zero as when locking to a constant value. This could be fixed by ensuring that the wrap point was never attained, by using 64 bit numbers in the integrator, for example, or by engineering the wrap point to be a multiple of a cycle.

The second plausible hypothesis is that the phasemeter is cycle slipping. This would result in the controller quickly adjusting for the now incorrect signal thereby causing jumps in its output. This could be fixed, as was suggested above, by improving the bandwidths of the relevant phasemeters. In the best performance achieved, this issue was resolved through a choice of gains that resulted in the magnitude of these jumps being exactly equal to one cycle at the output .

Another unresolved issue with the controller was that the difference between the dark and bright fibre relative phases changed by a quarter of a cycle when the controller was switched on. To fully resolve these issues further debugging of the digital signal processing is needed.

# CDMA-based Digital Interferometry

In order for the controller to function, it is necessary to measure the phase. In the previous implementation of the optical phased array [**?**], the sensor stage consisted of a single detector. The signals from each fibre were then separated from their delay using m-sequence based digital interferometry. In m-sequence based digital interferometry, separation of signals is attained by modulating the light with a single code, and ensuring that the autocorrelation of the code falls off sharply with delay. Signals can then be separated using their delay by demodulating with differently delayed codes. This was done by imposing a different length of fibre on each emitter. This is not a scalable approach for many elements because the lengths of fibre involved would become ungainly. In addition, such an array would be limited by dispersion. The delays would be dependent on the wavelength, and consequently the array could not receive at a different frequency than it transmits, limiting the array's applicability. For this reason *Code Division Multiple Access* (CDMA) based digital interferometry was evaluated to resolve these limitations. In broad terms, the CDMA based approach solves these problems by modulating each signal with a separate code, and requiring that the cross correlation between these codes is zero. This enables the light to be separated by its code, eliminating the need for any artificially imposed delay. This significantly simplifies the architecture. In the following chapter various design problems in the implementation of such a system are addressed. The system is found to separate signals with negligible crosstalk.

## 5.1 Requirements of the demodulation procedure

The modulation procedure provides us with the ability to multiplex the phase signals on a single detector. Similarly to the m-sequence based approach used in the previous design, the CDMA-based modulation-demodulation procedure makes use of digital codes made up of strings of $\pm 1's$. For the CDMA-based scheme to function, these codes must satisfy certain requirements. Here we discuss the requirements with the object of selecting the codes for use in the experiment. The first requirement is:

- The codes must be orthogonal[1]. If we let $C_i[n]$ denote the $n^{th}$ element of code $i$, then two code sequences $i$ and $j$ of length $N$ are orthogonal if:

---

[1]Note that if we were to relax the condition of perfect orthogonality, we may attain more codes at the cost of lower suppression. This was not investigated and might prove an interesting avenue of further work.

$$\sum_{n=0}^{n=N} C_j[n]C_i[n] = N\delta_{ij} \qquad (5.1)$$

This restriction forces us to use orthogonal vectors of $\pm 1$. For some code of length $N$, there are $N$ possible orthogonal vectors, since that is the dimension of the space, thus we are limited to $N$ perfectly orthogonal codes. These are called Hadamard codes. Hadamard codes of length 8 were used in this thesis. These are shown in table 5.1.

| Code | Sequence |
|:----:|:--------:|
| 1 | 1,1,1,1,1,1,1,1 |
| 2 | 1,-1,1,-1,1,-1,1,-1 |
| 3 | 1,1,-1,-1,1,1,-1,-1 |
| 4 | 1,-1,-1,1,1,-1,-1,1 |
| 5 | 1,1,1,1,-1,-1,-1,-1 |
| 6 | 1,-1,1,-1,-1,1,-1,1 |
| 7 | 1,1,-1,-1,-1,-1,1,1, |
| 8 | 1,-1,-1,1,-1,1,1,-1 |

**Table 5.1**: The Hadamard codes of length 8.

The second restriction required by the CDMA scheme is that:

- The codes average to zero over a code period. That is, they must be *balanced.* More explicitly, for a code $C_i[n]$ is balanced if:

$$\sum_{n=0}^{n=N} C_i[n] = 0 \qquad (5.2)$$

This eliminates code 1 in table 5.1 but we still may select any of the other 7.

However, in order for the demodulation to function, the demodulating codes need to be orthogonal with the codes modulated onto each signal. Since the codes on different channels will pass through differing optical paths, they will have different delays. Thus the demodulating code may need to be "tuned" to become synchronous with the code on the input signal, as not all the Hadamard codes remain orthogonal when delayed.

It is thus of interest to note that some Hadamard codes are better than others in terms of their orthogonality with respect to delay. One may observe that, codes 2, 3 and 5 are distinct in their period of 1 and -1, however codes 3 and 4 are simply permuted versions of one another, as are codes 5 and 7. This means that these pairs do not remain orthogonal when either is delayed, as eventually they will be identical, and their dot product will be the code length. The codes, 2, 3 and 5 are orthogonal in the event of any delay. For this reason, the codes 2, 3 and 5 were selected for the experiment. These codes are simply square waves with frequencies that are power of two multiples of the lowest frequency. The codes will henceforth be re-labelled as in table 5.2. Phase measurements from different codes will be called channels.

| Code | Sequence |
|------|----------|
| 0 | 1,-1,1,-1,1,-1,1,-1 |
| 1 | 1,1,-1,-,1,1,1,-1,-1 |
| 2 | 1,1,1,1,-1,-1,-1,-1 |

**Table 5.2**: Naming convention used from here on.

The final requirement is:

- The code repetition rate is much higher than the phase noise frequency.

To see how these requirements come to pass we consider the demodulation procedure.

From 2.18, a signal modulated with code $C[n]$ incident on the photodetector will be proportional to:

$$
\begin{aligned}
S &= \cos\left(\omega_h t + \phi_s + C[n]\delta\right) \\
&= Re\left(\exp(j(\omega_h t + \phi_s + C[n]\delta))\right)
\end{aligned}
$$

where $\omega_h$ is the heterodyne frequency and $\delta$ is the modulation depth. This modulation depth will need to be small in the final array, as altering the phase of the light is detrimental to the array performance[2]. In the event that the modulation depth is half a cycle, the modulation has the effect of changing the sign of the beatnote. To demodulate such a signal, we multiply the signal by the code. When the modulation depth is low, however, it is harder to see how one demodulates. It turns out that we can do exactly the same thing.
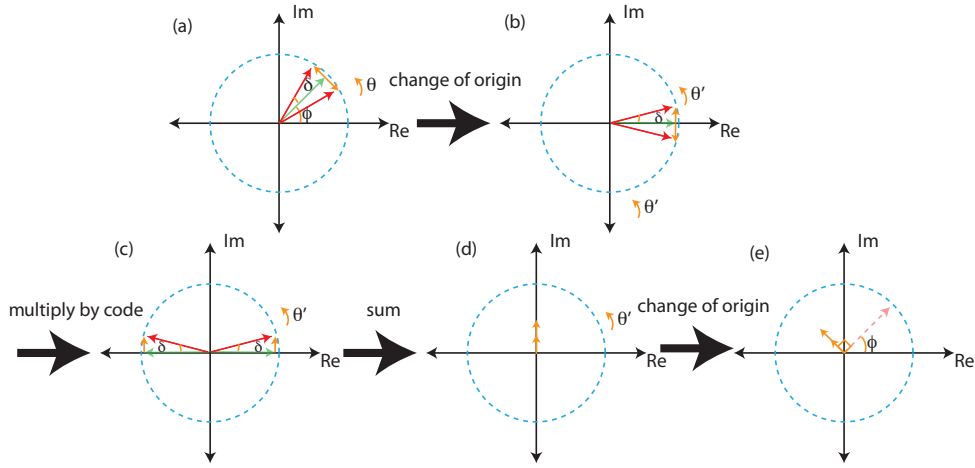


**Figure 5.1:** Phasor diagram illustrating the demodulation procedure for light modulated with a code of some small modulation depth $\delta$. See text for explanation.

This is best understood by considering the phasor diagram of the situation. This is shown in figure 5.1. The phase of the main carrier over the period of a code is represented by the green phasor. Over the period of the code, we assume that the change in the phase of the main carrier is negligible. This means $\omega t \approx$ constant for our analysis. The

---

[2]Note that we actually modulate the phase with $+\delta$ and 0. This is equivalent to modulating with $\frac{1}{2}\delta$ and $-\frac{1}{2}\delta$, with a constant phase offset. Since we only care about relative phase between channels, this constant offset can be ignored, and we can consider the phase to be modulated by $\pm\frac{1}{2}\delta$.

modulation has the effect of adding small phase offsets of angle $\delta$ about the main carrier. The resulting phasors are shown in red. Note that there will be multiple red phasors superimposed, depending on the code length. We desire the phase $\phi$ of the carrier, which we can measure if we "remove" the code offsets. This can be done by multiplying the encoded signal by the code directly, and summing over the length of the code.

The process is illustrated in the figure. The initial phasors of the carrier over the period of a code $C[n]$ of length $2N$ are shown superimposed in part (a). The phasor for the carrier offset by code chip $n$ may be represented by:

$$\vec{p}_n \equiv \exp\left(j(\omega t + \phi + C[n]\delta)\right) \tag{5.3}$$

For convenience we make a change of variables in the argument of the phasors, $\vartheta$. We define a new argument $\vartheta' = \vartheta - \phi$ so that the phase of the main carrier is shifted to $\vartheta' = 0$. Our representation becomes:

$$\vec{p}_n = \exp\left(j(\omega t + C[n]\delta)\right) \tag{5.4}$$

Now we multiply by the code $C_i(t)$ as in part (c). This has the result of flipping the phasors with negative offsets about the imaginary axis. If we then sum these phasors over the length of the code, and require that the code has the same number of $1's$ and $-1's$, the result will be a phasor that is the sum of the offset vectors. This is approximately perpendicular to the original carrier, thus we may recover the phase of the carrier by measurement of the phase of the resulting signal. Thus we see that the code must be balanced.

We may see this with our mathematical representation too. Let $S_{demod}$ represent the demodulated signal. Multiplying by the code and summing over the chips in the code gives:

$$
\begin{aligned}
S_{demod} = \sum_{n=1}^{2N} C[n] \exp\left(j(\omega t + C[n]\frac{\delta}{2})\right) &= \sum_{n=1}^{N} \left[\exp\left(j(\omega t + \delta)\right) - \exp\left(j(\omega t - \delta)\right)\right] \\
&= \exp(j\omega t) \sum_{n=1}^{N} \left[\exp\left(j\delta\right) - \exp\left(-j\delta\right)\right] \\
&= 2Nj\sin(\delta)\exp(j\omega t) \\
&= 2N\sin(\delta)\exp(j(\omega t + \frac{\pi}{2})) 
\end{aligned}
\tag{5.5}
$$

As we only care about relative phase, and the constant $\frac{\pi}{2}$ offset is common to all signals, it is not inimical to our interests. Reversing the change of origin we obtain:

$$S_{demod} = 2N\sin(\frac{\delta}{2})\exp(j(\omega t + \frac{\pi}{2} + \phi_s)) \tag{5.6}$$

A sinusoid with the phase that we desire, weighted by the sine of the modulation depth and the length of code. We may then obtain the phase $\phi_s$ from this sinusoidal signal by passing it to a phase-locked loop. Note the the strength of the signal depends on the length of the code and the modulation depth. We desire a small modulation depth, because the modulation disrupts the phase at the reference plate, however if we make the modulation depth too small, the signal to noise ratio of our phase measurements will decrease. We can improve this by increasing the length of the code, but if the code becomes too long,

we violate the assumption that the phase noise is constant over the code repetition rate. These compromises will need to be considered to find the optimal modulation depth for an optical phased array, and provide a matter for further investigation.

Now recall that multiple signals are incident upon both the bright and dark fibre detectors. These signals need to be separated. To ensure this we make the assumptions that the codes are orthogonal and balanced. This explains why we need this requirement. To see this more rigorously suppose we have $M$ codes of length $N$ incident on our detector so that the signal is proportional to:

$$S = \sum_{i=0}^{M} \exp\left(j(\omega t + C_i[n]\frac{\delta}{2})\right) \tag{5.7}$$

Then suppose we perform the demodulation described above for code q. We multiply by the values of code $i$ and sum to give:

$$S_{demod} = \sum_{n=1}^{2N} C_q[n] \sum_{i=0}^{M} \exp\left(j(\omega t + C_i[n]\frac{\delta}{2})\right) \tag{5.8}$$

$$= \exp(j\omega t) \sum_{i=0}^{M} \sum_{n=1}^{2N} C_q[n] \exp\left(jC_i[n]\frac{\delta}{2}\right) \tag{5.9}$$

Consider what happens when we evaluate $\sum_{n=1}^{2N} C_q[n] \exp\left(jC_i[n]\frac{\delta}{2}\right)$ for two orthogonal codes. We know from the orthogonality condition that:

$$\sum_{n=1}^{2N} C_q[n]C_i[n] = 0 \tag{5.10}$$

Suppose we divide this sum into two sums, one over all the $+1's$ in code $i$ and one over all the $-1's$. We may do this because code $i$ is balanced. Let $n^+ = \{n : C_i[n] = 1\}$ and $n^- = \{n : C_i[n] = -1\}$. Then our sum becomes:

$$\sum_{n \in n^+}^{N} C_q[n]C_i[n] + \sum_{n \in n^-}^{N} C_q[n]C_i[n] = 0 \tag{5.11}$$

Which simplifies to:

$$\sum_{n \in n^+}^{N} C_q[n] - \sum_{n \in n^-}^{N} C_q[n] = 0 \rightarrow \sum_{n \in n^+}^{N} C_q[n] = \sum_{n \in n^-}^{N} C_q[n] \tag{5.12}$$

But since code q is balanced too, this implies that there must be an equal number of $+1's$ as $-1's$ in $\{C_q[n] | n \in n^+\}$ and $\{C_q[n] | n \in n^-\}$ [3].

---

[3]To see this suppose that for a balanced code of length $2N$, and for two arbitrary sets of indices $W, M \subset [1..2N]$ we have:

$$\sum_{i \in W}^{N} C_i = \sum_{j \in M}^{N} C_j \tag{5.13}$$

Suppose for a contradiction that $\sum_{i \in W}^{N} C_i = \sum_{j \in M}^{N} C_j = k$, then there must be $k$ more $1's$ than $-1's$ in $\{C_i | i \in W\}$, and likewise for $\{C_i | i \in M\}$. This contradicts our assumption that the code was balanced.

Thus we see that we may break up our initial sum:

$$\sum_{n=1}^{2N} C_q[n] \exp\left(jC_i[n]\frac{\delta}{2}\right) = \sum_{n=1}^{N}\left[(\exp\left(j\frac{\delta}{2}\right) - \exp\left(j\frac{\delta}{2}\right)) + (\exp\left(j\frac{-\delta}{2}\right) - \exp\left(j\frac{-\delta}{2}\right))\right]$$
$$= 0$$

So for two orthogonal codes, the sum $\sum_{n=1}^{2N} C_q[n] \exp\left(C_i[n]\frac{\delta}{2}\right)$ is also orthogonal and all the terms of equation 5.8 corresponding to products between different codes go to zero, and we recover the signal modulated with the same code with which we demodulated:

$$\begin{aligned}
S_{demod} &= \exp(j\omega t)\sum_{i=0}^{M}\sum_{n=1}^{2N} C_q[n]\exp\left(jC_i[n]\frac{\delta}{2})\right) \\
&= \exp(j\omega t)\sum_{n=1}^{2N} C_q[n]\exp\left(jC_q[n]\frac{\delta}{2})\right) \\
&= 2N\sin(\frac{\delta}{2})\exp(j(\omega t + \frac{\pi}{2}))
\end{aligned}$$

Where in the last step we have used the result from equation 5.5.

### 5.1.1   Code length

To see why codes of length 8 were selected we first consider that the chip frequency needs to be high, to ensure the assumption that the phase noise is slow compared to the code repetition rate remained valid. However there is an upper bound on this frequency. This is because the phase we measure at the reference surface is what we need to control. This phase will comprise the sum of the phases from not only the light initially incident on the reference surface, but also light that has reflected from the reference surface, back through parts of the optical layout, and back to the reference surface again, possibly multiple times. A phasor diagram of this situation is shown in figure 5.2. The phasor from the first light to reach the reference surface will contribute most strongly because it will have the largest intensity. The phase of scattered light will contribute less, and are represented by the smaller phasors added to the larger one in the figure. The resultant phase is the sum of these phasors.

Since the largest contribution from scattered light will be from first few round trips between possible etalons, the chip frequency must be long enough to include this scattering within a chip. If the length of the setup is of the order of $\sim 3\,\mathrm{m}$, then this implies the frequency must be less than $f < \frac{c}{3} \approx 100\,\mathrm{MHz}$. Thus a nominal $10\,\mathrm{MHz}$ was selected.
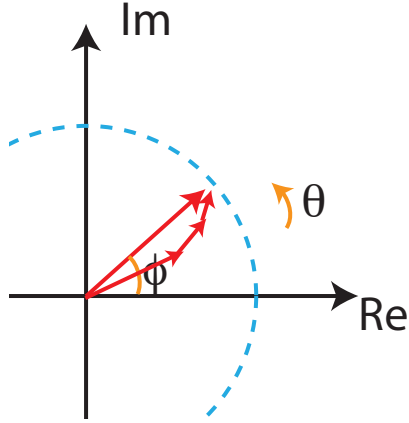
**Figure 5.2:** The phase at the reference surface $\phi$ comes from the sum of the phase of the light plus scattering between etalons within the optical setup.

## 5.2    Results

In order to measure the degree to which the coding scheme separated the respective phase signals, one fibre was phase modulated with a 67 Hz sinusoid of amplitude $380 \pm 20$ mVPP using the analogue outputs from the Labview system. Attenuators were placed on the digital outputs driving the codes such that the modulation depths were those indicated in table 5.3. The resulting cross talk between channels was determined by taking the amplitude of the 67 Hz frequency component of each of the phase measurements from each code. The ratio of the amplitudes from the unmodulated channels to the modulated channel was taken to be the measure of the cross talk. This is equivalent to taking the ratio of the respective peaks circled in the power spectral density plot in figure 5.3. This process was repeated for each fibre.
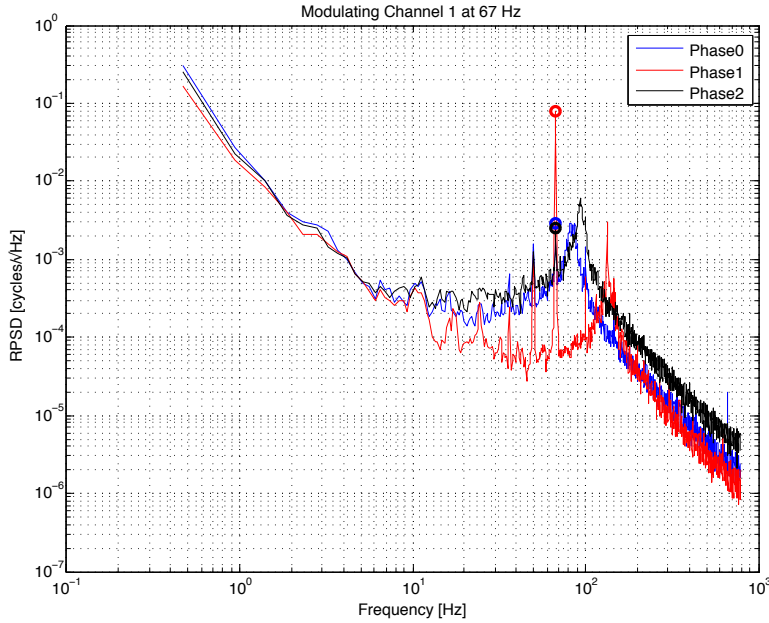
**Figure 5.3:** Plot showing the power spectral density of the unlocked phase of all three channels while modulating channel 1 with a 67 Hz sinusoid.

### 5.2.1 Initial code separation

Initially the coding scheme was implemented with a common chip frequency for all codes of 10 MHz. Table 5.4 displays the results for the cross talk from the dark fibre phase measurements, and table 5.5 displays the cross talk from the bright fibre phase measurements.

It was observed that this initial crosstalk was particularly bad in this scenario, especially from code 1 to code 0. This problem is resolved in the next section. The most likely explanation for this is that it is due to imperfections in the digital output. It was found that the output of the FPGA had some jitter in the duty cycle, or length of time spent in the on position. This was found to be up to $\pm 10\%$ from the desired $50\%$ over a code length and varied from code to code. Further, there was some lag in the switching between the "on" and "off" voltages. This effect would result in the higher frequency components of the square wave being attenuated, meaning that the proportion of power in the signal is more heavily weighted toward the lower frequency harmonics. Because the other codes are simply square waves of multiples of the lowest frequency, some of these harmonics will be common, resulting in crosstalk.

| Fibre | code | Modulator $v_\pi$ | code modulation depth (cycles) | Sinusoid modulation depth |
|---|---|---|---|---|
| Mode 1 | 0 | $2.1 \pm 0.1$ | $0.27 \pm 0.01$ | $0.18 \pm 0.01$ |
| Mode 2 | 2 | $2.1 \pm 0.1$ | $0.27 \pm 0.01$ | $0.18 \pm 0.01$ |
| Mode 3 | 1 | $2.2 \pm 0.1$ | $0.25 \pm 0.01$ | $0.17 \pm 0.01$ |

**Table 5.3**: Table showing the properties of the modulators on each fibre and the code used.

| Crosstalk onto code | code 0 modulated | code 1 modulated | code 2 modulated |
|:---:|:---:|:---:|:---:|
| 0 | 1 | $1.2 \pm 0.02$ | $(2 \pm 0.2) \times 10^{-3}$ |
| 1 | $(100 \pm 60) \times 10^{-3}$ | 1 | $(1 \pm 1) \times 10^{-3}$ |
| 2 | $(70 \pm 25) \times 10^{-3}$ | $(30 \pm 25) \times 10^{-3}$ | 1 |

**Table 5.4:** Table showing the crosstalk between channels as measured by the ratio of the amplitudes of the frequency components with the same frequency as the modulated sinusoid (67 Hz). The ratios in this table are derived from the dark fibre phase.

| Crosstalk onto code | code 0 modulated | code 1 modulated | code 2 modulated |
|:---:|:---:|:---:|:---:|
| 0 | 1 | $0.9 \pm 0.2$ | $(80 \pm 50) \times 10^{-3}$ |
| 1 | $(200 \pm 200) \times 10^{-3}$ | 1 | $(2 \pm 1) \times 10^{-3}$ |
| 2 | $(370 \pm 150) \times 10^{-3}$ | $(50 \pm 7) \times 10^{-3}$ | 1 |

**Table 5.5:** Table showing the crosstalk between channels as measured by the ratio of the modulated frequency components. These measurements were taken from signals from the bright fibre phase.

### 5.2.2    Improved code separation

To reduce the cross talk observed, the frequencies of the codes were shifted slightly with respect to one another as in table 5.6. This resolved the problem as is demonstrated in the cross-talk measurements shown in tables 5.7 and 5.8. It is believed this resolved the problem because the codes are now asynchronous, and shift with respect to one another over time. This causes the cross talk to average out to zero.

| Code | Chip frequency |
|:---:|:---:|
| 0 | 9.70 MHz |
| 1 | 10 MHz |
| 2 | 9.85 MHz |

**Table 5.6:** Table showing the crosstalk between channels as measured by the ratio of the modulated frequency components.

| Crosstalk onto code | code 0 modulated | code 1 modulated | code 2 modulated |
|:---:|:---:|:---:|:---:|
| 0 | 1 | $(40 \pm 20) \times 10^{-3}$ | $(4 \pm 1) \times 10^{-3}$ |
| 1 | $(3.1 \pm 1.5) \times 10^{-3}$ | 1 | $(3 \pm 2) \times 10^{-3}$ |
| 2 | $(0.06 \pm 2) \times 10^{-3}$ | $(40 \pm 20) \times 10^{-3}$ | 1 |

**Table 5.7:** Table showing the properties of the modulators on each fibre and the code used. These ratios were taken from signals from the dark fibre phase.

| Crosstalk onto code | code 0 modulated | code 1 modulated | code 2 modulated |
|:---:|:---:|:---:|:---:|
| 0 | 1 | $(72 \pm 40) \times 10^{-3}$ | $(9 \pm 4) \times 10^{-3}$ |
| 1 | $(2 \pm 1) \times 10^{-3}$ | 1 | $(30 \pm 6) \times 10^{-3}$ |
| 2 | $(15 \pm 5) \times 10^{-3}$ | $(100 \pm 20) \times 10^{-3}$ | 1 |

**Table 5.8:** Table showing the properties of the modulators on each fibre and the code used. These ratios were taken from signals from the bright fibre phase.

### 5.2.3   DAC output noise with and without codes

Further evidence attesting to the imperfections present in the Labview system output is given in figure 5.4. It shows the power spectral density of the output of the digital electronics with and without codes while driving a 5 Hz sinusoid out of the DAC on channel 0. Note that the code chip frequency was 10 MHz, and the longest code has a period of 8 chips. This means the lowest frequency we should expect to see noise at is 1.25 MHz. We clearly see noise below this threshold introduced by the code. This is most probably due to lag in the digital outputs.
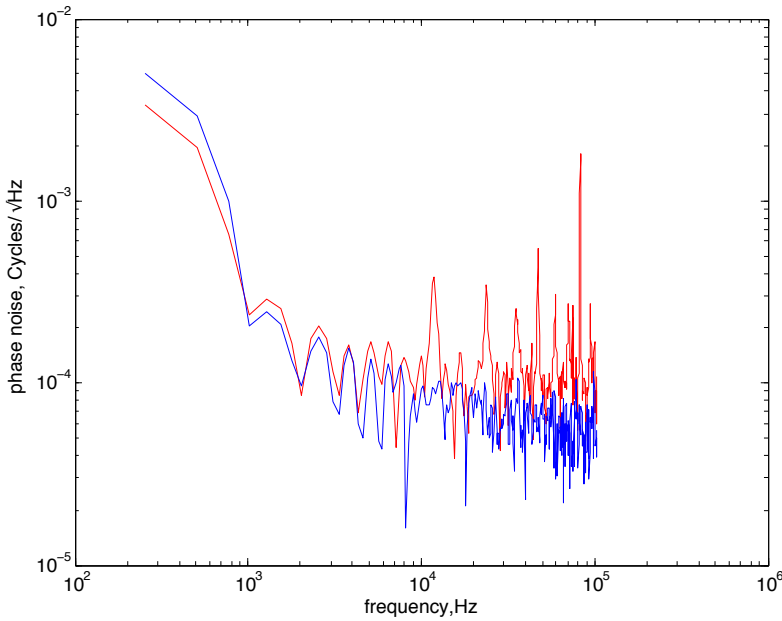


**Figure 5.4:** Plot showing the noise in the output of the ADC while driving a 5 Hz sinusoid with (red) and without codes (blue).

# Experimental Setup and Results

In order to test the main new features of the architecture, a prototype simulating some of the characteristics was constructed. The primary test goals for this experiment were to:

1. Ascertain whether the dark fibre could resolve the ambiguity in the measurement of the bright fibre.

2. Verify the function of the novel CDMA-based digital interferometry scheme, and measure the characteristics of its performance in terms of signal separation.

3. Assess the performance of the architecture with respect to two dimensional beam steering.

## 6.1   Optical Setup

In order to test the goals above, an optical prototype was constructed that combined three bright fibres with a single dark fibre. The layout is displayed in figure 6.1. 1064 nm light was used in accordance with the GRACE specifications[22].

Three bright fibres were chosen because this was the minimum required to demonstrate two dimensional beam steering. The beam path was aligned so as to begin at the laser, pass through some lenses to re-shape the laser mode, which was found to be elliptical, and then a faraday isolator to protect the laser from backscattered light. The beam was then split into two paths. One became the local oscillator path, and was frequency shifted by 79.3 MHz by an AOM, and directed to the bright and dark fibre detectors through further beamsplitters and steering mirrors.

The other path was coupled into polarisation maintaining optical fibre splitters, which split the beam into three paths to be used to simulate the bright fibres. Each of the bright fibres were phase modulated with photline NIR-LN-0.1 phase modulators.

Polarisation maintaining fibre is necessary, as the polarisation of the beam must remain the same for each of the three bright fibre modes.

Half-wave plates were used to match the polarisation of the free space beams to the axes of the polarisation maintaining fibres. This was because the splitting ratio of the splitters, as well as the input attenuation of the modulators is dependent on the polarisation of the light passing through them.

The light from the fibres was then released through fibre collimators and passed through half wave plates and polarising beamsplitter cubes. This ensured that the linear polarisation of the light from each mode was identical, and also allowed control over the intensity of each of the three modes, as the polarisation could be rotated with the half waveplate to allow different splitting ratios at the polarising beam splitter cube.

The light was then guided via steering mirrors onto beamsplitters where they were positioned relative to one another in a configuration that yielded both vertical and horizontal fringes, so as to allow for two dimensional beam steering.

After positioning, the beams were passed through a lens. This lead to a $170 \pm 2\,\mu$m waist size for the dark fibre and all of the bright fibre modes. This increased the divergence of the beams, allowing for observable overlap and steering within reasonable distances from the reference surface. Then the beams were directed to a $90 : 10$ beamsplitter, which acted as the reference surface.[1]

Back reflections from the reference surface were split by another beamsplitter, with one beam traveling to the dark fibre detector, and the other passing directly back into the fibre splitters, and onto the bright fibre detector. Each of these back reflections was mixed with the local oscillator at its respective detector in order to obtain a visible beatnote.

---

[1]In the actual final design, this will be replaced with a glass reference surface. This experiment was not concerned with simulating this aspect of the design, as the geometry is far from representative. Thus a 90:10 beamsplitter was used for ease of alignment.
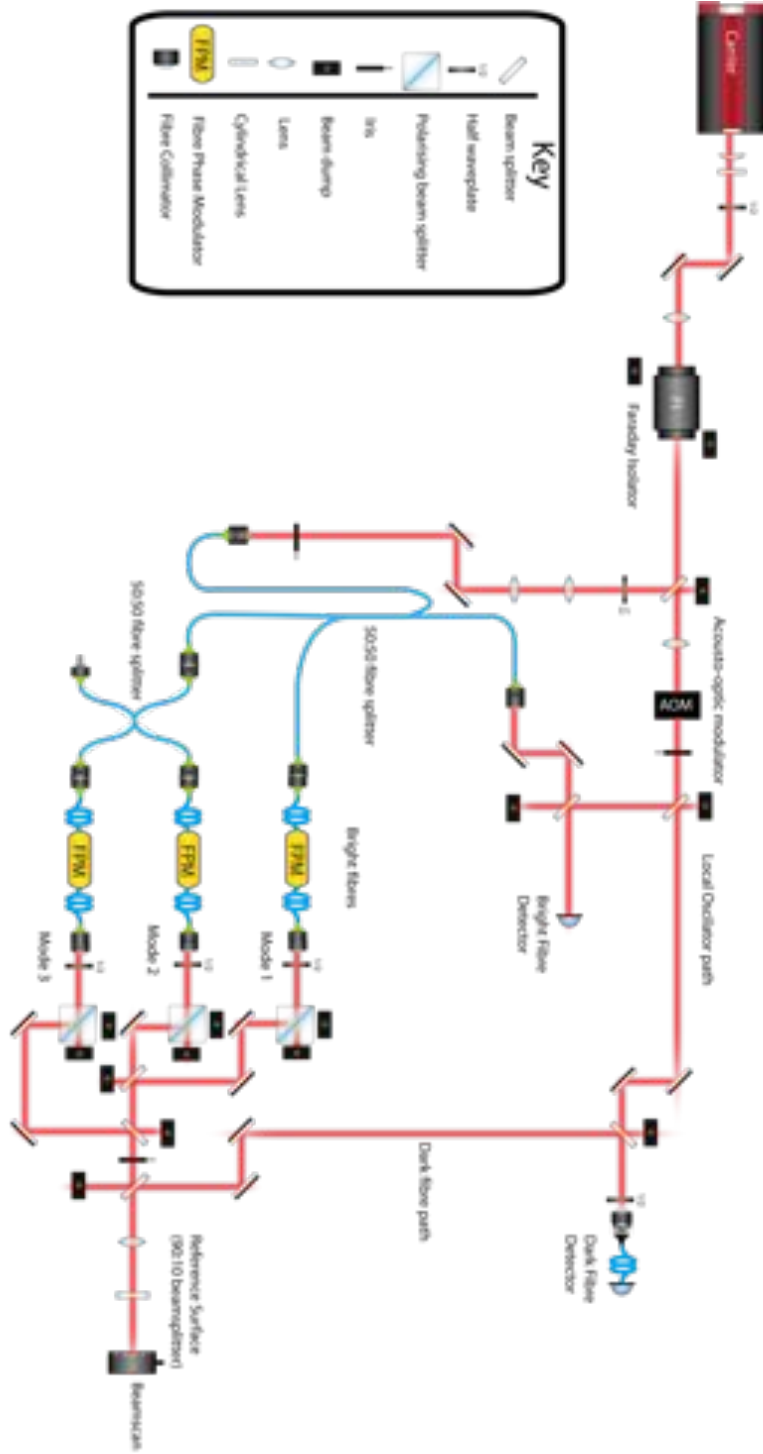
**Figure 6.1:** Diagram showing the prototype array constructed for the testing of the CDMA-based internally sensing optical phased array. The Laser used was an Innolight Prometheus, the modulators used for mode 1 2 and 3 were the photline NIR-LN-0.1 phase modulators. The AOM was an ISOMET 1205-843, and the detectors were both the newfocus 1811's.
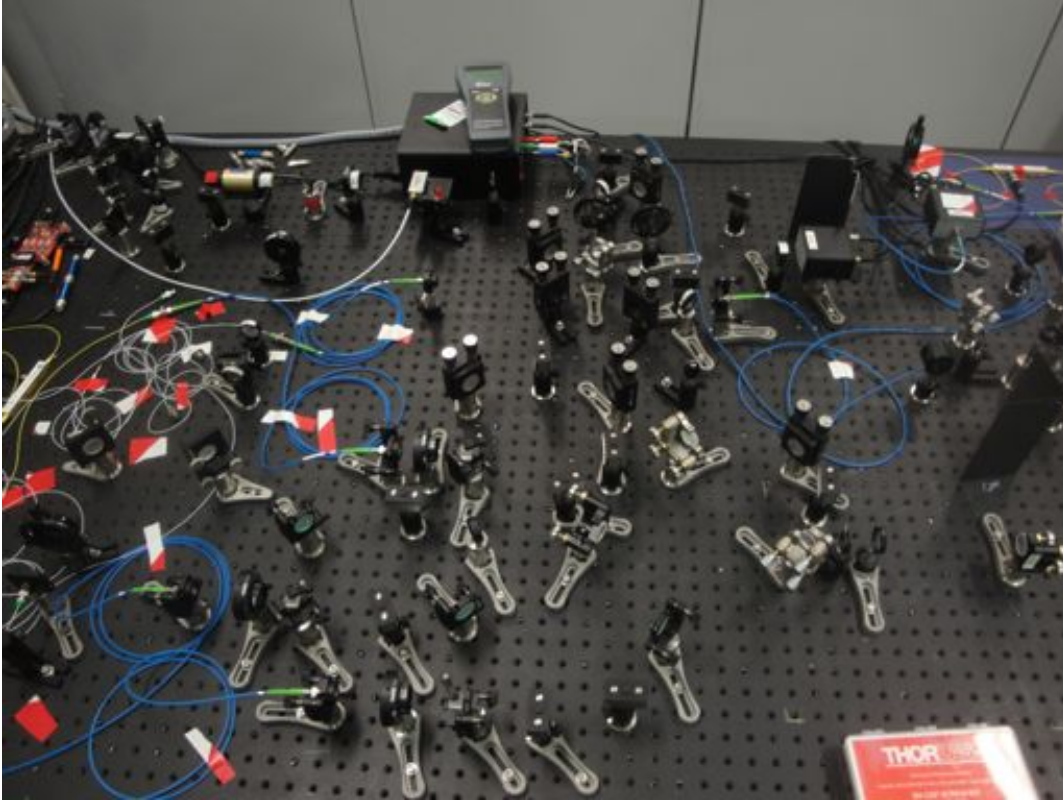
**Figure 6.2:** Photo showing the real layout constructed for the testing of the CDMA-based internally sensing optical phased array.

## 6.2 Techniques

There are a host of tricks and techniques that allow for speedy alignment of optical setup. The following are some that were used in my experiment. A theme that runs through all of the these techniques is that of maximisation: if one wants to position a beam in some manner, then one should first find a measurable quantity that is uniquely maximised when the beam is in that position. Then the method for attaining the desired beam position simply becomes a maximisation problem, whereby one iterates over the available degrees of freedom (for example, angles of a steering mirror) to maximise the aforementioned quantity. Examples of this follow.

### 6.2.1  Combination of science and local oscillator beams.

In order to properly mix the science and local oscillator beams at the detectors it was necessary to ensure that the modes of the beams roughly match. To accomplish this, the waist size of both beams must be the same, on the same side, and the same distance away from the beamsplitter on which they are combined. Further, the beams must be collinear. With two beams, there are thus a daunting 6 degrees of freedom to match, that is: the waist position, waist size, pointing angles, and positions of the beams in the plane perpendicular to the beam direction.

This problem was approached by considering the problems of waist size and position independent from the position and pointing angles alignment. First the beam modes were measured with a beam profiler by determining the beam waist at different positions, and

fitting the measurements to a gaussian model. If necessary one of the modes was then altered with one or more lenses so that the new effective waist was matched with that of the other beam. It should be noted that this matching is not particularly crucial in practice, and if the modes are not differing more than about 50% in spot size, and have a divergence to within about 10% at the beamsplitter, reasonable results may still be attained without the need for a lens.

After that, one beam was aligned with the other using steering mirrors placed in the path of the beam. Two steering mirrors are necessary, because for each mirror there are two degrees of freedom, thus there are four degrees of freedom for two mirrors, the same as the number of dimensions to be matched. To make the beams collinear, it is necessary to iterate over these four degrees of freedom to find the correct position. The iteration procedure is made significantly easier, and faster if one notes that the position of the beam in the near field is most significantly affected by the near field mirror, as labelled in figure 6.3. The iteration procedure then becomes to first align the beams by eye in the near field by overlapping their positions on an IR card using the near field mirror, then align the beam positions in the far field using the far field mirror, then return to the near field and align the beams there again, and repeat until interference fringes are visible.

If very good alignment is required, the procedure is continued, only with the fringes visible, the method is slightly changed. The beams are now steered in the vertical direction until horizontal fringes are visible, and then in the horizontal direction until vertical fringes are visible, with the near and then far field mirrors as above. The larger the fringes, the more closely aligned the beams, so this determines the direction of steering. It is sometimes easier to perform this task if the phase of one of the beams is modulated with a slow sinusoid with an amplitude of about 1 cycle. This means that the fringes oscillate with this frequency, and once the alignment is near-perfect, the fringes become the size of the beam, and the beam becomes a single pulsing dot.
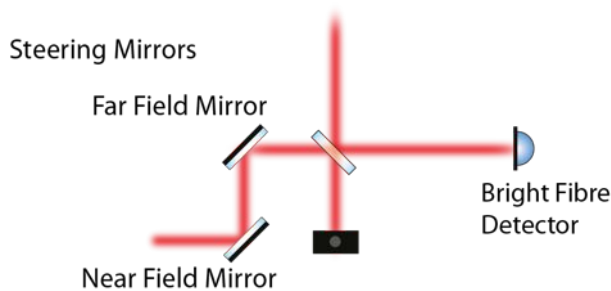


**Figure 6.3:**  Diagram showing the placement of steering mirrors for alignment on a beamsplitter of the local oscillator and science beam.

### 6.2.2  Coupling light into a fibre

To accomplish this stage, the setup shown in figure 6.4 was used. A fibre coupled light source was plugged into one side of the 50:50 fibre splitter. The subsequent beam emerging from the fibre would thus be the mode to which we should match the the incoming light. This was then accomplished in a similar manner to the above.

The outgoing mode was first measured with a beam scan, then the incoming mode was altered with lenses to roughly match this mode. Then the beams were made collinear by eye using an IR card in the manner described above. Once this was accomplished, there was enough light in the fibre to be visible on the readout of the fibre coupled power meter. From then on, the task becomes the simple but tedious one of maximising the power readout.

In order to accomplish this maximisation, one must iterate over the four dimensions of angle and position of the beam. Experience shows the best way to do this is to select the knobs on both the near and far field mirrors that steer the beam vertically. Then twist one of the knobs, say on the far field mirror to maximise the power. Then twist the other by a small amount in some direction, and twist the first to maximise the power again. Repeat this until it becomes obvious as to whether the maximum powers achieved through twisting the knob on the far field mirror are increasing or decreasing, and choose the subsequent direction of increments on the near field mirror accordingly. This method was dubbed "walking the beam".

It is important to note that if there are lenses in the path of one of the beams, then the beams must be made to overlap at two points on one side of the lenses. If the near and far field points are either side of the lenses, alignment at these two points does not imply collinearity, as the two beams might overlap at the two points, but have different angles at these points. This is why it is a good idea to have the steering mirrors after the lenses.
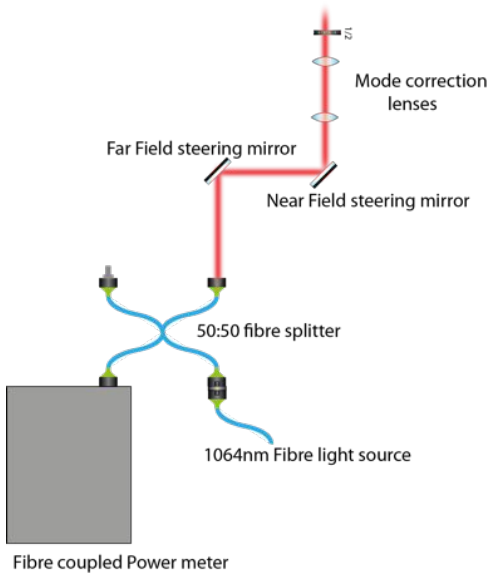


**Figure 6.4**: Diagram illustrating the setup used for aligning into a fibre.

### 6.2.3   Final alignment method for 2D beam steering

To accomplish two dimensional beam steering it was necessary to position the modes of the three bright fibres so they were offset from one another in such a way as to provide fringes in both the vertical and horizontal direction, to allow for two dimensional beam steering. Together with this are the requirements that the back reflection from each of the beams couple sufficiently well into themselves, and the dark fibre. This makes for a

highly constrained, and difficult, alignment problem, which was approached as follows.

The first step addressed the constraint that all the beams couple into the dark fibre. Some light was fed into the dark fibre, and the modes of the bright and dark fibres were compared. It was found that despite the different path lengths, the waist size and position of the modes from all four beams were approximately the same after the lens. Mode 2 shown in figure 6.5 was used as the reference beam, and the dark fibre was made collinear with this beam through the alignment methods for combining beams on a beamsplitter. This was performed while phase modulating mode 2 to the level that the interference displayed a single pulsing point of light. Now that the mode of the dark fibre and mode 2 were collinear, the waist position of the beams was measured, and the reference surface was placed about a centimetre further away from the lens.

The back reflections from both mode two and the light coupled into the dark fibre should now be collinear. This meant the reference surface could be made perpendicular to both beams, by ensuring the back reflection from the dark fibre was collinear with the output light from mode 2. This alignment was done by eye, placing the IR card between the mode 2 collimator and BS7, and steering the reference surface, which was mounted on a steering mirror mount, so that the the reflection and the beam from mode 2 overlapped well on the card. If this was done well enough, a beatnote would become visible from the signal from the dark fibre detector on an oscilloscope. This could then be maximised by aligning reference surface. Once this was done we know that the reference surface is perpendicular to the dark fibre mode, and should be perpendicular to mode 2, but may not be, due to errors in the initial alignment.

Then modes 1 and 3 could be positioned relative to mode 2. They were made collinear with mode 2, but not perfectly. Mode 1 was aligned such that large horizontal fringes were visible after BS4 when combined with mode 2 alone, and mode 3 was aligned so that large vertical fringes were visible after BS5 when combined with mode 2 alone. In this way, the net fringe pattern had both vertical and horizontal fringes, allowing two dimensional steering of the beam.

If necessary, the beatnote from the direct back reflections from all bright fibres was then maximised by choosing two of the steerable mounts in the path, and walking the beam. It was found this could be done without affecting the positioning too much.

Once this alignment was completed and results obtained, the mode positions were determined by removing the reference surface and determining the waist position and size with a beam scan.
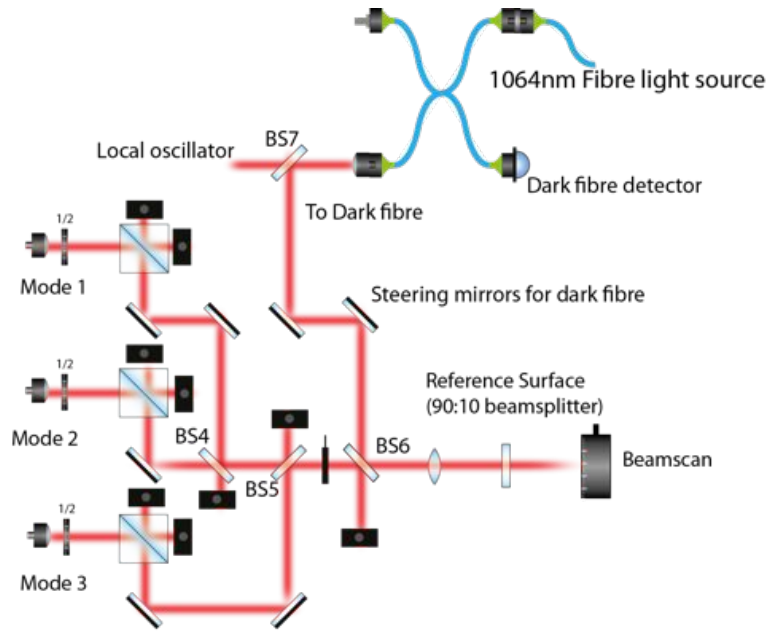
**Figure 6.5:** Diagram showing the part of the set up used to position the beams for 2d beam steering.

## 6.3 Digital Setup

To control the phase of the light, it was necessary to process the signals from the photodetectors in real time at high speeds (40 MHz). In order to accomplish this, the National Instruments PXI platform system was used. The data flow is shown in figure 6.6. Signals from the detectors were passed into two Analogue to Digital Converters (ADC's) which were operating at 40 MHz as triggered by a clock signal from the FPGA. A clock signal was also sent to the function generator so the beatnote frequency could be synchronised with the digital processing.

With a beatnote of 79.3 MHz, the under-sampling resulted in the signal being aliased down to $\sim 0.7$ MHz. This signal was then processed by a controller on the FPGA. The relatively low frequency feedback from the controller was taken directly from the in-built labview Digital to Analogue Converter's (DAC's). Each signal also needed to be modulated with the 10 MHz CDMA code signal. This could not be fed through these outputs, as the DAC's did not have the required bandwidth. Thus the digital signals were taken directly from the digital outputs, and combined with the analogue outputs with bias-T's. The digital outputs were also attenuated with attenuators so the modulation depth could be lowered.
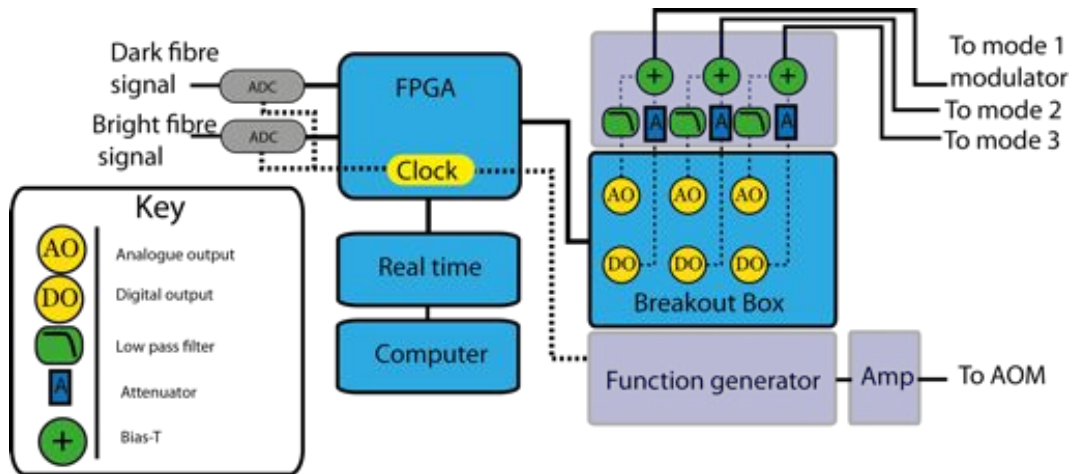
**Figure 6.6:** Diagram showing the digital processing data flow used. The FPGA used was the NI-PXI-7852R, the "Real time" embedded computer was the NI PXI-8106, and the NI-PXI-5404 clocks were used for synchronisation. The ADC's used were the MAX19588 and were 16bit, running at 100Mbps, and the function generator was the Agilent 33250-A. The mixers used were the minicircuits model ZFBT-4R2GW.

The controller was implemented in Labview, a graphical programming language. This was then compiled into Hardware Description language and transferred onto the FPGA. An image of roughly a quarter of my labview code is shown in figure The function of the controller could be monitored with the configuration by passing data from the FPGA to the "Real-time", a small computer running in parallel to the FPGA. The "Real-Time" was configured to then pass data onto the computer where it could be saved.
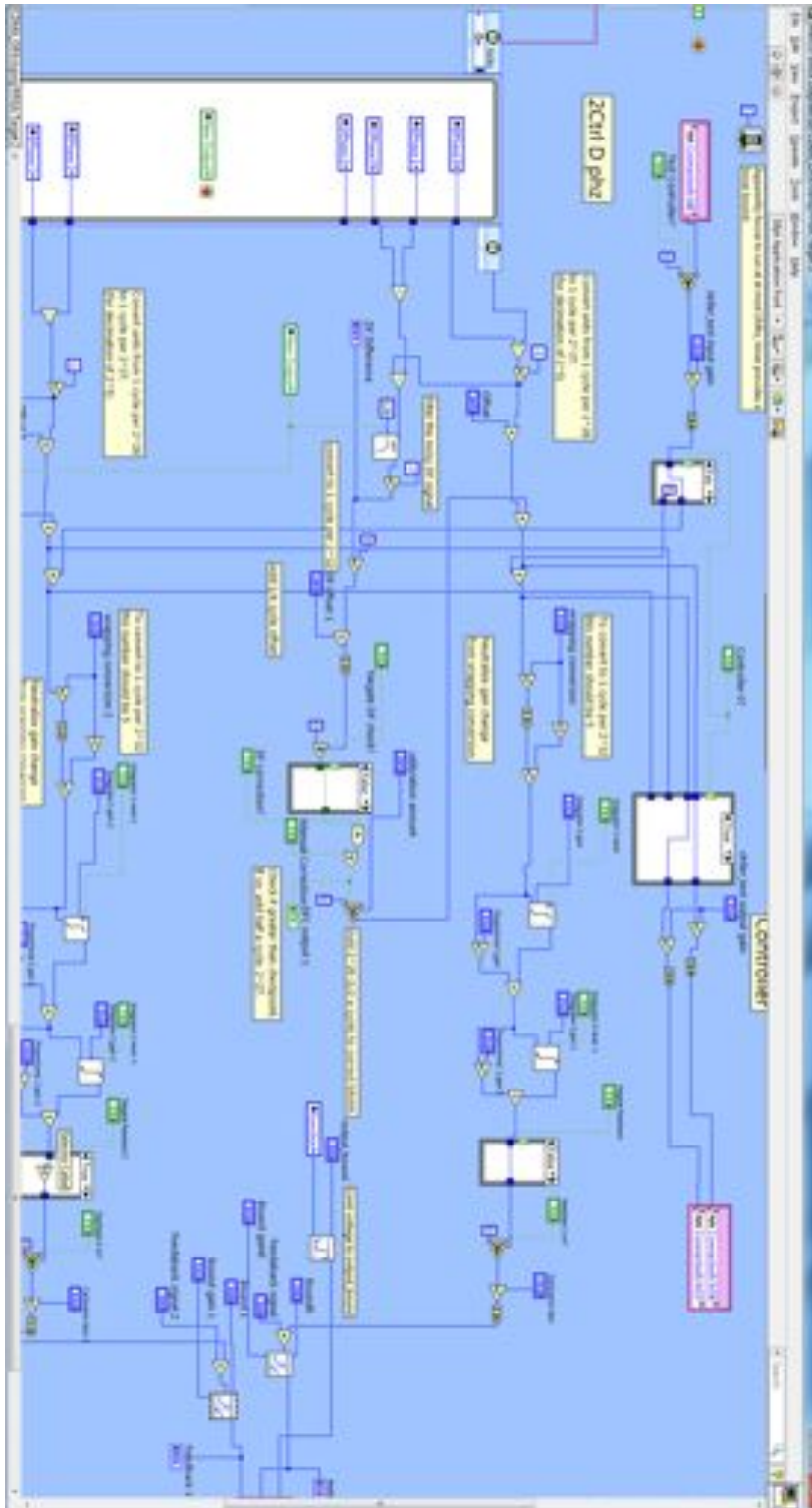
**Figure 6.7:** Part of the Labview code showing the two controllers. Not shown, but of similar size are the demodulation stage, the encoding stage and code for transferring data off the FPGA.

## 6.4   Array output

The function of the array was tested by shifting the lock point of the relative phase of both channels to steer the intensity peak in 2D. The relative phase of each pair of bright fibres was modulated sinusoidally with an amplitude of 0.5 cycles and a frequency of[2] $0.05 \pm 0.01$ Hz. The phase of one sinusoid was shifted relative to the other so the pattern traced by the peak was an ellipse. The ellipse could be clearly seen live on the beam scan, and a plot of the locus of intensity maxima is shown in figure 6.8. The coordinates used to generate this ellipse are shown in figure 6.9.

The ellipse was generated by finding the position of maximum intensity in the x and y planes at each point in time. The intensity measurements were taken from the beamscan, and were quite noisy. This noise was independent of any modulation and is presumably an artifact of the beamscan function. This explains the jitter in the peak position seen in both plots.

These results clearly indicate the ability of the array to perform two dimensional beam steering. Steering could be performed almost indefinitely, and was observed to function for times in excess of 10 minutes. The array could only be steered quite slowly for large amplitude steering, however. The results shown here were at the limit of the fastest sinusoid that could be steered of this magnitude. It is expected this is due to the wrapping problem discussed in chapter 4 that may have been caused by malfunctions in the phase-locked loops used to sense the phase. As discussed, it is believed this problem could be resolved through further controller development, and optimisation of the phasemeters.

---

[2]The error comes from how well the frequency was estimated, which was done by eye, it is not a measure of the jitter in frequency.
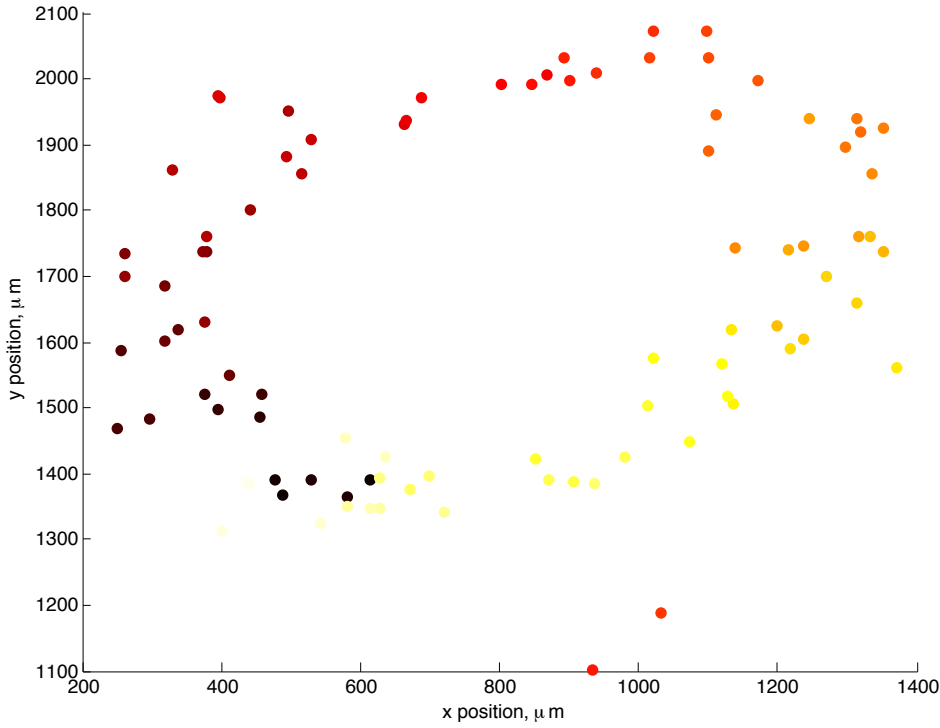
**Figure 6.8:** Plot of the positions of peak intensity over time while modulating both channels with a sinusoid, dark spots are less recent. The outliers on the lower right are when there are two peaks present on the y axis, so the position of maximum intensity is ambiguous.
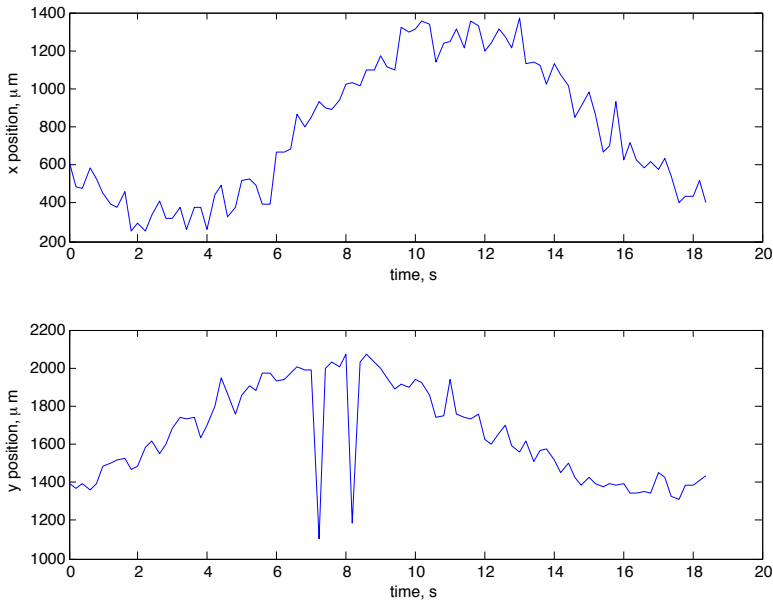


**Figure 6.9:** Plot of the positions of maximum intensity over time while modulating both channels with a sinusoid. The two sharp spikes in the y position are where there were two fringes present, thus the peak location was ambiguous.

# Conclusions and Further work

This thesis presented significant developments toward the goal of a scalable active optical phased array. Prior to this work, the design for the array sustained two main flaws. The first was an issue with the phase measurement within the array. The geometry was such that the phasemeters could initialise incorrectly, resulting in unreliable performance. We have solved this issue through a theoretical and experimental evaluation of the dark fibre solution. The theoretical studies investigated the application of an array of this design in a GRACE-like context. We concluded that such an array could function in this context, and suggested a more detailed initial design for a larger array. We also calculated the design tolerances required for this design, and highlight that pointing error may be a difficulty in future construction.

Having successfully evaluated the design in theory, we then provided experimental evidence supporting the viability of this new design. We demonstrated the ability of the dark fibre design to correct the phasemeter initialisation problem between two bright beams.

The second issue with the previous implementation was that it required significantly different optical path lengths for each emitter of the array in order to separate the phase signals. This would lead to an unscalable design. We provide a solution to this problem by the replacement of an m-sequence based modulation scheme with a CDMA-based modulation scheme. We concluded that the CDMA-based scheme separated the signals with minimal crosstalk, without the need for different fibre lengths.

A controller was developed, and tested experimentally with the result that the relative phase could be locked to within a standard deviation of $12\,\mu$Cycles in the presence of external noise. This improved on the previous controller by a factor of more than 800.

Finally, the array was scaled to two dimensions, and successfully performed two dimensional beam steering.

These results imply that the dark fibre is viable and are sufficiently convincing that further development will be conducted. With respect to the GRACE application, this will involve scaling the array to a large number of elements, the construction of the optical head, and integration with small waveguides with integrated phase modulators that are already under development at NASA's Jet Propulsion Laboratory. In order to improve the performance of the array for this, it would be worthwhile investigating ways to reduce the pointing error by varying other less critical parameters such as the glass thickness.

With respect to the space debris application, the phased array will form the basis of our group's involvement in a cooperative research centre for space debris tracking with EOS. The array will need to be scaled so we may drive each emitter with an individual laser, allowing for the significant power gains possible from coherent beam combining. With respect to this application, further study of the optimal modulation depth required

for a particular array with the CDMA modulation scheme should be performed.

An additional avenue that relates to both applications is further study of the scaling of the number of bright fibres with the size of the array. This will be reduced from the presence of the dark fibres. It might thus be prudent to look at the minimum fraction of dark fibres required for a functional array.

Beyond the two motivating this thesis, the possible applications of a scalable optical phased array are many, applications include optical communication networks [3, 4], high power beam combining [5], and wireless power beaming. Because of the increase in transfer efficiency that scales with $N^2$ for a phased-array emitter-receiver pair, the optical phased array would significantly improve laser power beaming systems. Another of particular relevance is that of Laser radar. The rapidity with which a phased array could be steered, together with its ability to increase the power on target would provide significant developments in the field of laser radar [2, 9].

# Bibliography

[1] R.C. Hansen. *Phased array antennas*, volume 213. Wiley-Interscience, 2009.

[2] Neha Sharma and Henry Zmuda. MIMO based optical phased array technology with electronic beam steering for laser radar applications. 7700:77000E–77000E–9, 2010.

[3] Karel Van Acoleyen, Hendrik Rogier, and Roel Baets. Two-dimensional optical phased array antenna on silicon-on-insulator. *Optics express*, 18(13):13655–60, June 2010.

[4] Y. Vilenchik, B.I. Erkmen, N. Satyan, A. Yariv, W.H. Farr, and J.M. Choi. Optical phase lock loop based phased array transmitter for optical communications. *The Interplanetary Network Progress Report*, 42:184, 2011.

[5] H. Injeyan and G.D. Goodno. *High power laser handbook*. McGraw-Hill Professional, 2011.

[6] Robert Spero. Orbiting laser interferometer to measure Earth's gravity. pages 10–12, 2002.

[7] Claude Phipps. Clearing space debris with lasers. *SPIE Newsroom*, pages 10–12, January 2012.

[8] D.J. Kessler, N.L. Johnson, JC Liou, and M. Matney. The kessler syndrome: Implications to future space operations. In *33rd Annual American Astronautical Society, Rocky Mountain Section, Guidance and Control Conference*, pages 6–10, 2010.

[9] Paul F Mcmanamon, Senior Member, Terry A Dorschner, David L Corkum, Larry J Friedman, Douglas S Hobbs, Michael Holz, Sergey Liberman, H U Y Q Nguyen, Daniel P Resler, Richard C Sharp, and Edward A Watson. Array Technology. *Proceedings of the IEEE.*, 84(2):268–298, 1996.

[10] Xiaozhang Wang, Qi Li, and Qi Wang. Progress and analysis of the liquid crystal phased array technology in ladar. *2010 Academic Symposium on Optoelectronics and Microelectronics Technology and 10th Chinese-Russian Symposium on Laser Physics and Laser TechnologyOptoelectronics Technology (ASOT)*, pages 273–276, July 2010.

[11] Shawn M Redmond, Daniel J Ripin, Charles X Yu, Steven J Augst, Tso Yee Fan, Peter A Thielen, Joshua E Rothenberg, and Gregory D Goodno. Diffractive coherent combining of a 2 . 5 kW fiber laser array into a 1 . 9 kW Gaussian beam. 37(14):2832–2834, 2012.

[12] Paul McManamon. An overview of optical phased array technology and status. *Proceedings of SPIE*, 5947:59470I–59470I–10, 2005.

[13] Sajjad Khan and Nabeel Riza. Demonstration of 3-dimensional wide angle laser beam scanner using liquid crystals. *Optics express*, 12(5):868–82, March 2004.

[14] Gregory D Goodno and S Benjamin Weiss. Automated co-alignment of coherent fiber laser arrays via active phase-locking. *Optics express*, 20(14):14945–53, July 2012.

[15] C X Yu, J E Kansky, S E J Shaw, D V Murphy, and C Higgs. Coherent beam combining of large number of PM fibres in 2-D fibre array. 42(18):1–2, 2006.

[16] Mikhail a Vorontsov, Svetlana L Lachinova, Leonid a Beresnev, and Thomas Weyrauch. Obscuration-free pupil-plane phase locking of a coherent array of fiber collimators. *Journal of the Optical Society of America. A, Optics, image science, and vision*, 27(11):A106–21, November 2010.

[17] Daniel Anthony Shaddock. Digitally enhanced heterodyne interferometry. *Optics letters*, 32(22):3355–7, November 2007.

[18] B. E. A Saleh and M. C. Teich. *Fundamentals of photonics*, volume 2. Wiley Interscience, 2007.

[19] W.E. Boyce, R.C. DiPrima, and D. Mitrea. *Elementary differential equations and boundary value problems*, volume 9. Wiley New York, 1977.

[20] A.E. Siegman. Lasers, 1986.

[21] A.M. James, M.P. Lord, and M.P. Lord. *Macmillan's chemical and physical data*. Macmillan, 1992.

[22] Benjamin Sheard and Gerhard Heinzel. GRACE follow-on laser ranging instrument Preliminary instrument specifications. 2012.

[23] H. Steinhaus. *Mathematical snapshots*. Dover Publications, 1999.

[24] G.F. Franklin, J.D. Powell, A. Emami-Naeini, and J.D. Powell. *Feedback control of dynamic systems*, volume 6. Addison-Wesley Reading, MA, 2010.

# Derivation of the Coupling Factor

In order to calculate the power coupled into the dark fibre for various geometries the following model was developed. The mode from both the bright and dark fibres were assumed to have gaussian form, with a waist at the end of the fibre. The amount of light then coupled into the dark fibre depends on how "similar" the mode of the bright fibre is to that of the dark fibre. This similarity is quantified in an overlap integral-the projection of the mode of the transmitting fibre onto the mode of the receiving fibre. In the following, the overlap integral between the mode from the receiving fibre, and the mode of the transmitting fibre is calculated to find the coupling factor; the fraction of power coupled into the dark fibre.

The geometry of the situation is shown in figure A.1. On the left is the actual geometry modeled, consisting of a single bright fibre and dark fibre. The reflection off the glass-air interface was accounted for by assuming that the power would be attenuated by a factor of 4%. This allowed the calculation of the overlap integral for the analogous situation on the right, where the modes have been reflected about the axis formed from the reference-plate air interface.

Once the below expressions for the magnitude and phase of the coupling factor had been derived, they were plotted in mathematica for the various situations of interest.
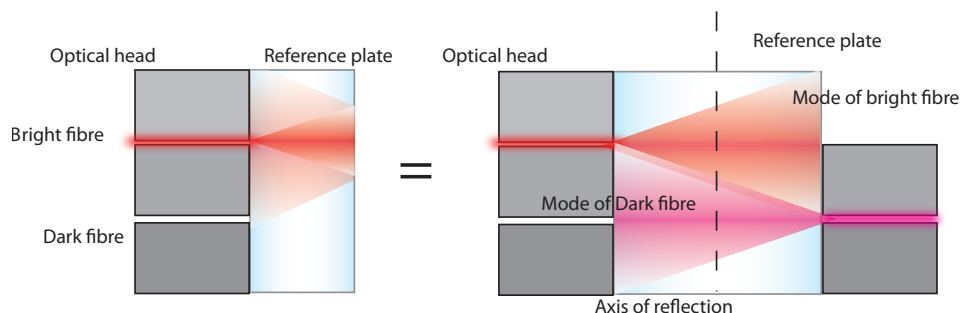


**Figure A.1:** The situation considered for the calculation of the coupling factor. Because of symmetry the power coupled from the reflected light from the bright fibre into the dark fibre (left) is the same as the power coupled into a dark fibre reflected about the axis shown, with the power attenuated according to the reflectance of the glass-air interface (right). To find the coupling factor, the overlap integral between the gaussian mode of the bright fibre (red) and dark fibre (pink) was found.

## A.1 Derivation

To find the fraction of power coupled from transmitting mode $E_t$ to receiving mode $E_r$, we find the projection of the mode from the transmitting fibre onto a mode from the receiving fibre and normalise appropriately. That is, the transfer efficiency $\eta$ is:

$$\eta = \frac{|\int_{\partial A} E_t E_r^* dA|^2}{\int_{\partial A} E_t E_t^* dA \int_{\partial A} E_r E_r^* dA} \tag{A.1}$$

Where $\partial A$ is some surface, in our case this will be a the 2D plane parallel to the receiving fibre tip. Both transmitting and receiving modes are assumed to have gaussian form with radius $d_r$ for the receiver and $d_t$ for the transmitter, corresponding to the fibre width. Light of wavelength $\lambda$ is assumed to travel distance $z$ in the direction of beam propagation from a source located at the origin. The beam from the transmitter, at $(0, 0, z)$ is given by [**?**]:

$$E = E_T \frac{d_t}{W_t} \exp\left[ -\frac{(x^2 + y^2)}{W_t^2(z)} - j\left( kz + k\frac{(x^2 + y^2)}{2R_t(z)} - \zeta_t(z) \right) \right] \tag{A.2}$$

Where $E_T = \sqrt{\frac{2P_0}{\pi d_t^2}}$, $W_t = d_t \sqrt{1 + (\frac{z}{z_t})^2}$, $z_t = \frac{\pi d_t^2}{\lambda}$, $\zeta_t(z) = \arctan(\frac{z}{z_t})$, $k = \frac{2\pi}{\lambda}$ and

$$R_t(z) = \begin{cases} \infty & z = 0 \\ z\left[ 1 + \left( \frac{z_t}{z} \right)^2 \right] & z \neq 0 \end{cases} \tag{A.3}$$

This definition indicates that at $z = 0$ there is no phase term. The mode for the receiving dark fibre at $(x_0, y_0, z)$ is given by[1]:

$$E = E_R \frac{d_r}{W_r} \exp\left[ -\frac{1}{d_r^2}(x^2 + y^2 + 2xx_0 + 2yy_0 + x_0^2 + y_0^2) \right] \tag{A.4}$$

Where, similarly to the above, $E_R = \sqrt{\frac{2P_0}{\pi d_r^2}}$, $W_r = \omega_r \sqrt{1 + (\frac{0}{z_t})^2} = d_r$. Now we evaluate the overlap integral over all space at $z = 0$, and note that over this domain $\int_{\partial A} E_t E_t^* dA = \int_{\partial A} E_r E_r^* dA = 1$. Thus:

$$\eta = |\int_{-\infty}^{\infty} \int_{-\infty}^{\infty} E_t E_r^* dx dy|^2 \tag{A.5}$$

Evaluating the integral:

$$\int_{-\infty}^{\infty} \int_{-\infty}^{\infty} E_t E_r^* dx dy = \int_{-\infty}^{\infty} \int_{-\infty}^{\infty} E_T E_R \frac{d_t}{W_t} \exp\left[ -\frac{1}{d_r^2}(x^2 + y^2 + 2xx_0 + 2yy_0 + x_0^2 + y_0^2) \right] \times$$
$$\exp\left[ -\frac{1}{W_t^2(z)}(x^2 + y^2) - j\left( kz + k\frac{(x^2 + y^2)}{2R_t(z)} - \zeta_t(z) \right) \right] dx dy$$

---

[1]Note that there are no phase terms because we are considering the receiving mode at the waist.

More explicitly: $E_T E_R = \sqrt{\frac{2P_0}{\pi d_t^2}} \sqrt{\frac{2P_0}{\pi d_r^2}} = \frac{2P_0}{\pi d_r d_t}$ , so:

$$
\begin{aligned}
CF &= \frac{2}{\pi d_t d_r} \int_{-\infty}^{\infty} \int_{-\infty}^{\infty} \frac{d_t}{W_t} \exp\left[ -\frac{1}{d_r^2}(x^2 + y^2 + 2xx_0 + 2yy_0 + x_0^2 + y_0^2) \right] \times \\
&\quad \exp\left[ -\frac{1}{W_t^2(z)}(x^2 + y^2) - j\left( kz + k\frac{(x^2 + y^2)}{2R_t(z)} - \zeta_t(z) \right) \right] dxdy
\end{aligned}
$$

(A.6)

taking out constants and rearranging:

$$
\begin{aligned}
CF &= \frac{2}{\pi d_t d_r} \exp\left[ -j(kz - \zeta_t(z)) \right] \frac{d_t}{W_t} \times \\
&\quad \int_{-\infty}^{\infty} \int_{-\infty}^{\infty} \exp\left[ -\frac{1}{d_r^2}(x^2 + y^2 + 2xx_0 + 2yy_0 + x_0^2 + y_0^2) \right. \\
&\quad \left. -\frac{1}{W_t^2(z)}(x^2 + y^2) - jk\frac{(x^2 + y^2)}{2R_t(z)} dxdy \right]
\end{aligned}
$$

We will now concern ourselves with the integral. Considering the following simplified form and making changes of variable, noting that $\int_{-\infty}^{\infty} \exp(x^2)dx = \sqrt{\pi}$ we see:

$$
\begin{aligned}
\int_{-\infty}^{\infty} \exp(-(ax^2 + bx + c))dx &= \frac{1}{\sqrt{a}} \int_{-\infty}^{\infty} \exp(-(w^2 + \frac{b}{\sqrt{a}}w + c))dw \\
&= \frac{1}{\sqrt{a}} \int_{-\infty}^{\infty} \exp(-(w + \frac{b}{2\sqrt{a}})^2 - c + \frac{b^2}{4a})dw \\
&= \sqrt{\frac{\pi}{a}} \exp(\frac{b^2}{4a} - c)
\end{aligned}
$$

Rewriting our integral into the above form:

$$
\begin{aligned}
I &= \int_{-\infty}^{\infty} \int_{-\infty}^{\infty} \exp\left[ -(\frac{1}{d_r^2} + \frac{1}{W_t^2(z)} + \frac{jk}{2R_t(z)})x^2 - \frac{2}{d_r^2}xx_0 \right] \times \\
&\quad \exp\left[ -(\frac{1}{d_r^2} + \frac{1}{W_t^2(z)} + \frac{jk}{2R_t(z)})y^2 - \frac{2}{d_r^2}yy_0 - \frac{(x_0^2 + y_0^2)}{d_r^2} \right] dxdy
\end{aligned}
$$

Now let $Q = \frac{1}{d_r^2} + \frac{1}{W_t^2(z)}$, $B = \frac{k}{2R_t(z)}$

$$
\begin{aligned}
I &= \int_{-\infty}^{\infty}\int_{-\infty}^{\infty} \exp\left[-(Q+jB)x^2 - \frac{2}{d_r^2}xx_0 - (Q+jB)y^2 - \frac{2}{d_r^2}yy_0 - \frac{(x_0^2+y_0^2)}{d_r^2}\right] dx\,dy \\
&= \sqrt{\frac{\pi}{(Q+jB)}} \int_{-\infty}^{\infty} \exp\left[\frac{1}{(Q+jB)\omega_r^4}x_0^2 - (Q+jB)y^2 - \frac{2}{d_r^2}yy_0 - \frac{(x_0^2+y_0^2)}{d_r^2}\right] dy \\
&= \sqrt{\frac{\pi}{(Q+jB)}} \int_{-\infty}^{\infty} \exp\left[-(Q+jB)y^2 - \frac{2}{d_r^2}yy_0 - \frac{(x_0^2+y_0^2)}{d_r^2} + \frac{1}{(Q+jB)d_r^4}x_0^2\right] dy \\
&= \frac{\pi}{(Q+jB)} \exp\left[\frac{1}{(Q+jB)d_r^4}y_0^2 - \frac{(x_0^2+y_0^2)}{d_r^2} + \frac{1}{(Q+jB)d_r^4}x_0^2\right] \\
&= \frac{\pi}{(Q+jB)} \exp\left[(\frac{1}{(Q+jB)d_r^4} - \frac{1}{d_r^2})(x_0^2+y_0^2)\right] \\
&= \frac{\pi}{(Q^2+B^2)^{\frac{1}{2}}} \exp(-jAtan2(B,Q)) \exp\left[(\frac{Q-jB}{(Q^2+B^2)d_r^4} - \frac{1}{d_r^2})(x_0^2+y_0^2)\right] \\
&= \frac{\pi}{(Q^2+B^2)^{\frac{1}{2}}} \exp(-jAtan2(B,Q)) \exp\left[(\frac{Q}{(Q^2+B^2)d_r^4} - \frac{1}{d_r^2})(x_0^2+y_0^2) - j\frac{B(x_0^2+y_0^2)}{(Q^2+B^2)d_r^4}\right]
\end{aligned}
$$

Where we have used the identity $x + jy = \sqrt{x^2+y^2}\exp(jAtan2(y,x))$ to convert all complex numbers to polar form for easier identification of the phase. Here $Atan2(y,x)$ is defined as below:

$$
Atan2(y,x) = \begin{cases}
\arctan(\frac{y}{x}) & x > 0 \\
\arctan(\frac{y}{x}) + \pi & y \geq 0, x < 0 \\
\arctan(\frac{y}{x}) - \pi & y < 0, x < 0 \\
\frac{\pi}{2} & y > 0, x = 0 \\
-\frac{\pi}{2} & y < 0, x = 0 \\
undefined & y = 0, x = 0
\end{cases}
\tag{A.7}
$$

Combination with the above gives the coupling factor as:

$$
\begin{aligned}
CF &= \frac{2}{\pi d_t d_r} \exp\left[-j(kz - \zeta_t(z))\right] \frac{d_t}{W_t} \times I \\
&= \frac{2}{d_r W_t (Q^2+B^2)^{\frac{1}{2}}} \exp\left[(\frac{Q}{(Q^2+B^2)d_r^4} - \frac{1}{d_r^2})(x_0^2+y_0^2)\right] \times \\
&\quad \exp\left[-j\left(kz - \zeta_t(z) + Atan2(\frac{B}{Q}) + \frac{B(x_0^2+y_0^2)}{(Q^2+B^2)d_r^4}\right)\right]
\end{aligned}
$$

Hence the magnitude is given by:

$$
|CF| = \frac{2}{d_r W_t (Q^2+B^2)^{\frac{1}{2}}} \exp\left[(\frac{Q}{(Q^2+B^2)d_r^4} - \frac{1}{d_r^2})(x_0^2+y_0^2)\right]
$$

Which means the power transfer efficiency is $\eta = |CF|^2$. The phase is given by:

$$
\arg(CF) = \arg\left(\exp\left[-j\left(kz - \zeta_t(z) + Atan2(\frac{B}{Q}) + \frac{B(x_0^2+y_0^2)}{(Q^2+B^2)d_r^4}\right)\right]\right)
\tag{A.8}
$$

It should be noted that because of the special case at $z = 0$, $B$ is defined as:

$$B = \begin{cases} 0 & z = 0 \\ \frac{k}{2R_t(z)} & z \neq 0 \end{cases} \tag{A.9}$$

We see that the argument of the coupling factor becomes 0 when $z = 0$ with this definition, as is expected.

## A.2 Relative phase as a function of distance between the transmitter and receiver

Expansion of the material between the fibres may cause relative phase errors at the receiving fibre. It is thus useful to know the derivative of the phase with distance so that this error may be estimated for a given separation. The phase of the signal at the receiving fibre is given by:

$$\text{arg}(CF) \quad = \quad \left( kz - \zeta_t(z) + \arctan(\frac{B}{Q}) + \frac{B(x_0^2 + y_0^2)}{(Q^2 + B^2)d_r^4} \right)$$

Let $r_0 = \sqrt{x_0^2 + y_0^2}$ be the radial separation between the fibres. Then we see that:

$$arg(CF) = kz - \zeta_t(z) + \arctan(\frac{B}{Q}) + \frac{Br_0^2}{(Q^2 + B^2)d_r^4} \tag{A.10}$$

Thus the derivative with respect to distance is:

$$\frac{darg(CF)}{dr_0} = \frac{2Br_0}{(Q^2 + B^2)d_r^4} \tag{A.11}$$

## A.3 Mathematica commands used

The following mathematica commands were executed to calculate the coupling factor in the various situations detailed in chapter 3.

**Figure A.2**: Mathematica commands executed to define the functions derived above.

# Incorporation of Pointing angle error

As the fibre pointing angle may not be perfectly aligned with both the surface of the glass and the receiving dark fibre, it is necessary to determine whether these angle deviations could have significant effect on the coupling factor and phase error. To derive this we consider the situation as sketched below:
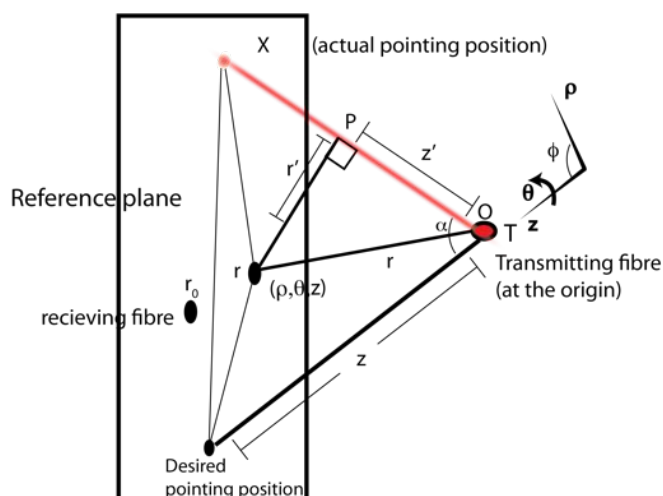


**Figure B.1**: Geometry for fibre pointing off desired axis by some angle $\alpha$.

We need only have one fibre rotated, since we can choose our coordinates such that the plane over which we conduct the overlap integral is normal to the direction of the receiving fibre. We exploit symmetry in the problem, and use cylindrical polar coordinates. We desire the electric field the at interrogation point $\vec{r} = (\rho, \vartheta, z)$. This will be given by the gaussian mode from the transmitting fibre at radius $\vec{r'}$, and distance $\vec{z'}$. The line $\overline{TX}$ can be parametrised by some $t \in \mathbb{R}$, such that its locus is given by:

$$v\vec{(t)} = \hat{k}t \tag{B.1}$$

where $\hat{k} = (k_\rho, k_\vartheta, k_z)$, is the unit wavevector for the transmitting gaussian mode, and we have positioned the transmitter at the origin. The vector from any point on this line to I is thus given by:

$$\vec{p}(t) = \vec{r} - v\vec{(t)} = \vec{r} - \hat{k}t \tag{B.2}$$

Now we know that the vector $\vec{r'}$ is perpendicular to $\vec{k}$, hence we can find the value of the parameter $t$ at which this occurs:

$$p(\vec{t}) \cdot \hat{k} = 0 \rightarrow t_p = \frac{\vec{r} \cdot \hat{k}}{||\vec{k}||^2} = \vec{r} \cdot \hat{k} \tag{B.3}$$

Since $||\hat{k}|| = \hat{k} \cdot \hat{k} = 1$. Thus

$$\vec{r'} = \vec{p}(t_p) = \vec{r} - \hat{k}t_p = \vec{r} - \hat{k}(\vec{r} \cdot \hat{k}) \tag{B.4}$$

and

$$\vec{z'} = \hat{k}(\vec{r} \cdot \hat{k}) \tag{B.5}$$

Let the receiving fibre be positioned at $\vec{r_0} = (\rho_0, \vartheta_0, z)$, the coupling factor then becomes, in polar coordinates:

$$
\begin{aligned}
CF \quad = \quad & \frac{2}{\pi W_t d_r} \int_0^{2\pi} \int_0^{\infty} \exp\left[-\frac{1}{d_r^2}||\vec{r} - \vec{r_0}||^2\right] \times \\
& \exp\left[-\frac{||\vec{r'}||^2}{W_t^2(||\vec{z'}||)} - j\left(k||\vec{z'}|| + k\frac{||\vec{r'}||}{2R_t(||\vec{z'}||)} - \zeta_t(||\vec{z'}||)\right)\right] \rho \, d\rho \, d\vartheta
\end{aligned}
$$

Note from B.4:

$$
\begin{aligned}
||\vec{r'}||^2 \quad = \quad & \vec{r}^2 - 2(\vec{r} \cdot \hat{k})^2 + \hat{k}^2(\vec{r} \cdot \hat{k})^2 \\
= \quad & \vec{r}^2 - (\vec{r} \cdot \hat{k})^2 \\
= \quad & \rho^2 + z^2 - (\rho k_\rho \cos(\vartheta - k_\vartheta) + zk_z)^2
\end{aligned}
$$

and from B.5:

$$||\vec{z'}|| = \rho k_\rho \cos(\vartheta - k_\vartheta) + zk_z \tag{B.6}$$

Now all of $W_t(||\vec{z'}||)$, $R_t(||\vec{z'}||)$, and $\zeta_t(||\vec{z'}||)$ depend on $\rho$ and $\vartheta$, rendering the integral much more difficult, thus the solution will be obtained numerically.

To do this it was necessary to specify bounds over which it was reasonable to assume the value of the integral differed little from the exact solution. These bounds can be found by noting the gaussian form of the receiving fibre mode becomes very small for large $\rho$. More specifically the integrand is:

$$\exp\left[-\frac{||r'||^2}{W_t^2(||\vec{z'}||)} - j\left(k||\vec{z'}|| + k\frac{||\vec{r'}||}{2R_t(||\vec{z'}||)} - \zeta_t(||\vec{z'}||)\right)\right]\exp\left[-\frac{1}{d_r^2}||\vec{r} - \vec{r_0}||^2\right] \leq \tag{B.7}$$

$$
\begin{aligned}
\exp\left[-\frac{||r'||^2}{W_t^2(||\vec{z'}||)}\right]\exp\left[-\frac{1}{d_r^2}||\vec{r} - \vec{r_0}||^2\right] \quad \leq \quad & \exp\left[-\frac{1}{d_r^2}||\vec{r} - \vec{r_0}||^2\right] \\
= \quad & \exp\left[-\frac{1}{d_r^2}\left(\rho^2 + \rho_0^2 - 2\rho\rho_0\cos(\vartheta - \vartheta_0)\right)\right]
\end{aligned}
$$

so the integrand is bounded above by the integral over the receiving mode, which since it is evaluated at the waist of the receiving fibre, may be well approximated by integrating about the receiving fibre by some finite length. Note that shifting the origin to the receiving

fibre we may write:

$$\int_0^{2\pi} \int_0^{\infty} \exp\left[-\frac{1}{d_r^2}||\vec{r} - \vec{r_0}||^2\right] d\rho d\vartheta = \int_0^{2\pi} \int_0^{a} \exp\left[-\frac{1}{d_r^2}\rho^2\right] d\rho d\vartheta + \int_0^{2\pi} \int_a^{\infty} \exp\left[-\frac{1}{d_r^2}\rho^2\right] d\rho d\vartheta \tag{B.8}$$

it was found numerically that for $\frac{a}{d} = 5$, the error:

$$\int_0^{2\pi} \int_a^{\infty} \exp\left[-\frac{1}{d_r^2}\rho^2\right] d\rho d\vartheta \approx 10^{-11} \times d \tag{B.9}$$

This is an upper bound on the error of the actual function, and for our purposes will be more accurate than our knowledge of the pointing angle of the transmitting fibre, and thus will suffice. Since $d \approx 7\,\mu m$, we integrate over a radius of $a \approx 35\,\mu m$ around the receiving fibre. Again, making the origin the at receiving fibre, so that the new vector pointing to the interrogation position is: $\vec{r_2} = \vec{r} - \vec{r_0} = (\rho_2, \vartheta_2, 0)$, the integral becomes:

$$\begin{aligned} CF &= \frac{2}{\pi W_t d_r} \int_0^{2\pi} \int_0^{a} \exp\left[-\frac{1}{d_r^2}||\vec{r_2}||^2\right] \times \\ &\quad \exp\left[-\frac{||\vec{r'}||^2}{W_t^2(||\vec{z'}||)} - j\left(k||\vec{z'}|| + k\frac{||\vec{r'}||}{2R_t(||\vec{z'}||)} - \zeta_t(||\vec{z'}||)\right)\right] \rho_2 d\rho_2 d\vartheta_2 \end{aligned} \tag{B.10}$$

Where

$$||\vec{r_2}||^2 = \rho_2^2 \tag{B.11}$$

Define $\hat{x}$, $\hat{y}$, to be cartesian basis vectors in the receiving fibre plane, the magnitudes $||\vec{r'}||$ and $||\vec{z'}||$ now become:

$$\begin{aligned} ||\vec{r'}||^2 &= ||\vec{r}||^2 - (\vec{r} \cdot \hat{k})^2 = ||\vec{r_2} + \vec{r_0}||^2 - ((\vec{r_2} + \vec{r_0}) \cdot \hat{k})^2 \\ &= ||(\rho_2 \cos(\vartheta_2) + \rho_0 \cos(\vartheta_0))\hat{x} + (\rho_2 \sin(\vartheta_2) + \rho_0 \sin(\vartheta_0))\hat{y} + z\hat{z}||^2 \\ &\quad - ((\rho_2 \cos(\vartheta_2) + \rho_0 \cos(\vartheta_0))k_\rho \cos(k_\vartheta) + (\rho_2 \sin(\vartheta_2) + \rho_0 \sin(\vartheta_0))k_\rho \sin(k_\vartheta) + k_z z)^2 \\ &= \rho_2^2 \cos^2(\vartheta_2) + \rho_0^2 \cos^2(\vartheta_0) + 2\rho_0\rho_2 \cos(\vartheta_2)\cos(\vartheta_0) + \\ &\quad \rho_2^2 \sin^2(\vartheta_2) + \rho_0^2 \sin^2(\vartheta_0) + 2\rho_0\rho_2 \sin(\vartheta_2)\sin(\vartheta_0) + z^2 - \\ &\quad (\rho_2 \cos(\vartheta_2)k_\rho \cos(k_\vartheta) + \rho_0 \cos(\vartheta_0)k_\rho \cos(k_\vartheta) + \\ &\quad k_\rho\rho_2 \sin(\vartheta_2)\sin(k_\vartheta) + k_\rho\rho_0 \sin(\vartheta_0)\sin(k_\vartheta) + k_z z)^2 \\ &= \rho_2^2 + \rho_0^2 + 2\rho_0\rho_2 \cos(\vartheta_2 - \vartheta_0) + z^2 - \\ &\quad (\rho_2 k_\rho \cos(\vartheta_2 - k_\vartheta) + \rho_0 k_\rho \cos(\vartheta_0 - k_\vartheta) + k_z z)^2 \end{aligned} \tag{B.12}$$

and

$$\begin{aligned} ||\vec{z'}|| &= \vec{r} \cdot \hat{k} = ((\vec{r_2} + \vec{r_0}) \cdot \hat{k})^2 \\ &= \rho_2 k_\rho \cos(\vartheta_2 - k_\vartheta) + \rho_0 k_\rho \cos(\vartheta_0 - k_\vartheta) + k_z z \end{aligned} \tag{B.13}$$

Now we may evaluate the integral over the receiving fibre plane with respect to $\rho_2$ and $\vartheta_2$. For just two fibres, we may choose the angular position of the receiving fibre from the

transmitting fibre to be $\vartheta_0 = 0$. If we desire the beam from the transmitter to be at some angle $\alpha$, relative to the intended direction, we find:

$$\tan\alpha = \frac{k_\rho}{k_z} = \frac{k_\rho}{\sqrt{1-k_\rho^2}} \rightarrow k_\rho(\alpha) = \frac{\tan\alpha}{\sqrt{1+\tan^2\alpha}} \tag{B.14}$$

$k_\vartheta$ may be chosen arbitrarily between 0 and $2\pi$, though for analysis of error it is simplest to choose it at the angle that affects the phase at the receiving fiber the most, and detriments the coupling factor the most. For $\vartheta_0 = 0$, this angle was found to be $\pi$. Finally, $k_z$ is chosen to make $\hat{k}$ have magnitude 1. This gives the expression:

$$k_z^2 + k_\rho^2 = 1 \rightarrow k_z(\alpha) = \sqrt{1-k_\rho^2(\alpha)} \tag{B.15}$$

Using equations B.11,B.12,B.13,B.14 and B.15, the integral B.10 was computed numerically in mathematica for the cases of interest. It was found to agree with the previous model in the case of no pointing error as expected. More specifically, the following commands were executed with varying parameters:



**Figure B.2:** Mathematica commands that define the function used to evaluate the magnitude and phase of the coupling factor for various parameters.

```
w0 = 6.2;
p0 = 1;

kr[α_] := Tan[α] / (1 + Tan[α]²)^0.5;

krA[α_] := α / (1 + α²)^0.5;

ks[α_] := (1 - kr[α]^2)^0.5;

ksA[α_] := 1 / (1 + α²)^0.5;

zmn[r_, θ_, zo_, kth_, α_, ro_, θo_] := r * kr[α] * Cos[θ - kth] + ro * kr[α] * Cos[θo - kth] + zo * ks[α];

rmn[r_, θ_, zo_, kth_, α_, ro_, θo_] := (r² + ro² + 2 * ro * r * Cos[θ - θo] + zo² - zmn[r, θ, zo, kth, α, ro, θo]²)^0.5;

CF[zo_, kth_, α_, ro_, θo_] := 2 / (π * W[zo, w0] * w0) NIntegrate[r * Upol[r, 0, w0, p0, 0] * \
    Upol[rmn[r, θ, zo, kth, α, ro, θo], zmn[r, θ, zo, kth, α, ro, θo], w0, p0, 0], \
    {r, 0, 5 * w0}, {θ, 0, 2π}, AccuracyGoal → 5, PrecisionGoal → 5]
```

**Figure B.3:** Further mathematica commands that define the function used to evaluate the magnitude and phase of the coupling factor for various parameters.

# Far Field model

## C.1 Calculation of power at point.

To calculate the power in a 1 mm radius aperture at 220 km, the following model was developed in c. It first calculates the position of all the bright fibres in the hexagonal pattern, and adds a 5% normally distributed random error to the spacing. It then goes through each point on a grid in the far field, and calculates the electric field contribution from the bright fibres by approximating their modes as gaussian, and summing them. It also adds the following normally distributed random errors with means and standard deviations as follows:

- Intensity: $\mu = 1$, $\sigma = 0.05$.

- Polarisation: $\mu = 0$, $\sigma = 1°$.

- Phase error: $\mu = 0$, $\sigma = 10^{-3}$.

The electric field thus calculated, it then finds the overlap integral over the region of interest and normalises appropriately. It does this 10 times and takes the mean and standard deviation of the results to find the power coupled. In calculating the overlap integral a digital grid of resolution $100 \times 100$ is used.

```
//
//  Hex_FF_2D_power.c
//
//
//  Created by Emmanuel Malikides on 27/09/12.
//  Generates the far field output of a hexagonal-lattice optical phased array
//  with dark fibres.
//


//


// UNITS ARE IN MICRONS!
#include <stdio.h>
#include <complex.h>
#include <stdlib.h>
#include <assert.h>
#include <string.h>
#include <math.h>
```

```
#include <time.h>

const double pi=3.14159265358979323846264338327950288419716939937510;

#define df 0
#define lf 1

// function that returns the value of a gaussian mode with source at xo yo on a
// plane a distance z away, and at position x,y, phase shifted such that the peak
// is at px,py.
complex double gmode(double x, double y, double z, double w0, double po,
                     double lambda, double xo, double yo, double px, double py){
    double R=0.0;
    complex double mag;
    // calculate the intensity
    double E0=sqrt(2.0*po/pi/w0/w0);
    // calculate the rayleigh range
    double z0=pi*w0*w0/lambda;
    // calculate the waist size
    double wz=w0*sqrt(1.0+(z*z)/(z0*z0));
    // calculate the wavefront radius
    if (z!=0.0) R=z*(1.0+(z0*z0)/(z*z));
    // calculate radial vector squared over the grid
    double rhosq=(x-xo)*(x-xo)+(y-yo)*(y-yo);
    double ph =(px-xo)*(px-xo)+(py-yo)*(py-yo);
    // wavenumber
    double k=2.0*pi/lambda;
    // deal with zero case
    if (z==0.0) {
        mag=(complex double)E0*(w0/wz)*exp(-rhosq/wz/wz);
    } else {
        mag=((complex double)E0*(w0/wz)*exp(-rhosq/wz/wz))*
        cexp(-I*k*(rhosq-ph)/(2.0*R));
    }
    return mag;
}

// calculate the variance of a list
double var(double ns[], int length, double mean){
    double sum=0.0;
    int i=0;
    for (i=0;i<length;i++) {
        sum+=(ns[i]-mean)*(ns[i]-mean);
    }
    return sum/(double)length;
}

// calculates the mean of a list
```

```
double mean(double ns[], int length) {
    double sum=0.0;int i=0;
    for (i=0;i<length;i++) sum+=ns[i];
    return sum/(double)length;
}

// calculates a normally distributed random number.
double rand_normal(double mean, double stddev) {
    static double n2 = 0.0;
    static int n2_cached = 0;
    double x,y,r;

    if (!n2_cached) {
        do {
            x = 2.0*rand()/RAND_MAX - 1;
            y = 2.0*rand()/RAND_MAX - 1;
            r = x*x+y*y;
        } while (r == 0.0 || r > 1.0);

        {
            double d = sqrt(-2.0*log(r)/r);
            double n1 = x*d;
            n2 = y*d;
            double result = n1*stddev + mean;
            n2_cached = 1;
            return result;
        }
    } else {
        n2_cached = 0;
        return n2*stddev + mean;
    }
}

// rotates a point counter clockwise about the origin by a given angle
void rotate(double source[3], double output[3], double angle) {
    output[0]=source[0]*cos(angle)+source[1]*sin(angle);
    output[1]=source[0]*sin(angle)-source[1]*cos(angle);
    output[2]=source[2];
    return;
}

// generates list of positions for hexagonal array, the centre of the pattern is
// always a dark fibre.
void hex_grid(double array[][3], int nRings, double pos[2],double rad, double error

    int tmp=0,tmp1=0,i,j;
    array[tmp][0]=pos[0];
    array[tmp][1]=pos[1];
```

```
        array[tmp][2]=df;
        tmp++;
        //Array stores the coorinates as well as the type of fibre (dark = 0,
        //light=1)
        int nTri=nRings*(nRings+1)/2;
        double triangle[nTri][3];
        double dx=rad/2,dy=rad*sqrt(3)/2;

        //generate a triangle
        for (i=1;i<=nRings;i++) {
            for (j=0;j<=i-1;j++) {
                triangle[tmp1][0]=(2*j-i)*dx+rand_normal(0,error);
                triangle[tmp1][1]=i*dy+rand_normal(0,error);
                triangle[tmp1][2]=((i+j)%3==0?df:lf);
                tmp1++;
            }
        }

        //add rotated versions of the triangle to the list to complete the hexagon
        for (i=0;i<6;i++) {
            for (j=0;j<nTri;j++) {
                rotate(triangle[j],array[tmp],i*pi/3);
                tmp++;
            }
        }
        return;
}


int main()

{

        //wavelength of light
        const double LL=1.064;
        //fibre aperture, 3.3 is Mode field Radius for thorlabs PM980-XP PM fibre
        const double WW=70;
        // calculate the rayleigh range
        double z0=pi*WW*WW/LL;
        //distance to far field
        //    const double ZZ=1000*z0;
        //200km
        const double ZZ=220000000000;
        printf("distance to far field: %e\n",ZZ);
        const double sep=150;
        //number of rings in hexagon
        const int Rings=27;
        //resolution of simulation grid
```

```
const int  m=100;
//receiving mode width in microns
const double WR=1000;
//length and width of simulation grid in microns
const double l=2*WR;
const double w=2*WR;

//pointing position
const double PX=0.0;
const double PY=0.0;
double pos[2]={PX,PY};
const double dy=(double)l/(double)(m-1);
const double dx=(double)w/(double)(m-1);
int i=0;
// number of sources
const int NSources=6*(Rings*(Rings+1)/2)+1;
double sources[NSources][3];
hex_grid(sources,Rings,pos,sep,0);
int NBright=0;
for (i=0;i<NSources;i++) {
    NBright+=sources[i][2];
}
printf("The number of bright fibres was: %d\n",NBright);
printf("The number of dark fibres was: %d\n",NSources-NBright);
// intensity of each element.
const double P0=1.0/NBright;
double amplitudes[NSources];
double badamplitudes[NSources];
double phaseerrors[NSources];

//stdev in position as percentage of spacing
const double vars[2]={0.05,0.15};
const int origin=m/2;
FILE *fp;
// output file
fp=fopen("out.dat","wt");

// temporary variables to store scores, iterators and such
int j=0,k=0,ii=0,jj=0,kk=0;
double x=0.0;
double y,tmp,intensity, dphase;
double z[m];
double dphi=0;
double meanpower=0;

int NRuns=5;
double powers[NRuns];
// standard deviation of position error (in microns)
```

```
    double poserror=44;
    complex double tmode,rmode,cftemp;
    double recpower,tpower;
    srand((int)time(NULL));

    for (i=0;i<NRuns;i++) {

        // generate amplitude and phase errors.
        for (ii=0;ii<NSources; ii++) {
            // polarisation error, with mean 0 and standard deviation of
            // 1 degree, or about 0.02 radians
            dphi=rand_normal(0,0.02);
            // intensity, a normally distributed random variable with mean 1
            // and standard deviation of 5%
            amplitudes[ii]=cos(dphi)*abs(rand_normal(1.0,0.05));
            // amplitudes of signals with orthogonal polarisations
            badamplitudes[ii]=sin(dphi);
            phaseerrors[ii]=rand_normal(0,0.001);
        }

        //fill sources with relevant positions.
        hex_grid(sources,Rings,pos,sep,poserror);
        cftemp=recpower=tpower=0.0;

        //calculate the coupling factor over the area
        for (ii=0;ii<m;ii++) {
            for (jj=0;jj<m;jj++) {
                // generate coordinate which we are looking at.
                y=dy*jj-l/2;
                x=dx*ii-w/2;
                tmode=rmode=0.0;
                // if we are within the aperture, add to coupling factor.
                // add the contributions from each source at this position with
                // some phase error.
                if(x*x+y*y<WR*WR) {
                    for (k=0;k<NSources;k++) {
                        dphase=phaseerrors[k];
                        tmode +=
                        cexp(I*dphase)*
                        (amplitudes[k]+badamplitudes[k])*
                        (sources[k][2]?
                         gmode(x, y, ZZ, WW, P0, LL, sources[k][0], sources[k][1], PX, PY)
                         :0.0);
                    }
//                  tmode=gmode(x, y, ZZ, WW, 1.0, LL, 0, 0, 0, 0);
                    rmode=gmode(x, y, 0.0, WR, 1.0, LL, 0, 0, 0, 0);
                    cftemp+=tmode*conj(rmode)*dx*dy;
                    recpower+=rmode*conj(rmode)*dx*dy;
```

```
                    tpower+=tmode*conj(tmode)*dx*dy;
            } else {
            }
            //                     fprintf(fp," %e",cabs(tmode)*cabs(tmode));
        }
        fprintf(fp,"\n");
    }
    // normalise.
    printf("tpower %e\nrpower %e\n",tpower,recpower);
    powers[i]=cabs(cftemp)*cabs(cftemp)/recpower;
    printf("power coupled: %e\n",powers[i]);
}
printf("dx %e\ndy %e\n",dx,dy);
meanpower=mean(powers,NRuns);
printf("Power coupled: %e+- %e\n",meanpower,sqrt(var(powers,NRuns,meanpower)));

fclose(fp);
return 0;
}
```